UNIVERSITY OF CALIFORNIA
SANTA CRUZ

# SEARCH FOR DARK MATTER SATELLITES OF THE MILKY WAY WITH THE FERMI LAT

A dissertation submitted in partial satisfaction
of the requirements for the degree of

DOCTOR OF PHILOSOPHY

in

PHYSICS

by

**Sheridan Zalewski**

March 2013

The Dissertation of Sheridan Zalewski is approved:

---

Professor Robert Johnson, Chair

---

Professor Steve Ritz

---

Professor Stefano Profumo

---

Tyrus Miller
Vice Provost and Dean of Graduate Studies

# Table of Contents

**List of Figures** **v**

**List of Tables** **ix**

**Abstract** **x**

**Dedication** **xi**

**Acknowledgments** **xii**

**1 Dark Matter - evidence, models, simulations** **4**
1.1 History . . . . . 4
1.2 Modified gravity as an alternative to DM . . . . . 9
1.3 DM particle candidates . . . . . 12
1.3.1 Axions . . . . . 12
1.3.2 WIMPs . . . . . 13
1.4 Non-SUSY WIMP models . . . . . 15
1.5 Supersymmetry and WIMPs . . . . . 16
1.6 DM detection . . . . . 18
1.6.1 Direct detection . . . . . 19
1.6.2 Gamma rays from neutralino annihilation . . . . . 19
1.6.3 Gamma ray lines . . . . . 20
1.6.4 Continuum gamma ray production . . . . . 20
1.7 DM distribution and structure . . . . . 22
1.8 DM galactic subhalos . . . . . 25
1.8.1 Gamma-ray flux from Dark Matter Satellites . . . . . 28

**2 *Fermi* Large Area Telescope** **31**
2.1 Structure . . . . . 32
2.2 Event reconstruction, analysis, and classification . . . . . 36
2.2.1 Event reconstruction . . . . . 36
2.2.2 Event analysis . . . . . 38
2.2.3 Event classes . . . . . 41
2.3 IRFs . . . . . 45

**3 Analysis** **50**
3.1 Likelihood methods for LAT data . . . . . 50
3.1.1 Likelihood analysis . . . . . 51
3.1.2 Pointlike . . . . . 53
3.1.3 Chernoff's and Wilks' Theorems . . . . . 55
3.2 LAT source analysis principles . . . . . 58
3.2.1 Region of Interest (ROI) . . . . . 58
3.2.2 Background modeling . . . . . 58
3.2.3 LAT livetime and exposure . . . . . 59
3.2.4 LAT high-level data . . . . . 60
3.3 Analysis methods . . . . . 61
3.3.1 Dataset . . . . . 62
3.3.2 Initial candidate source selection . . . . . 65
3.3.3 Spatial Test . . . . . 67
3.3.4 Spectral Test using the Comprehensive Test . . . . . 68

**4 Results and discussion** **78**
4.1 Search for Dark Matter Satellites in LAT Unassociated Sources 78
4.2 Calculation of upper limits on DM annihilation cross-section . 79
4.2.1 Detection efficiency . . . . . 80
4.2.2 Realizations of N-body simulations . . . . . 84
4.2.3 Upper limits on annihilation cross-section . . . . . 86
4.3 Discussion . . . . . 90

**Bibliography** **93**

# List of Figures

1.1 The rotation curve of M31, published in [75], using the optical data of Rubin & Ford [78]. . . . . 5
1.2 Two images of the bullet cluster. On the left is the optical image of the individual galaxies. The majority of the baryonic mass of the cluster however is in the two clouds of hot X-ray emitting gas, shown on the right in the Chandra map. The green countours are the gravitational lensing maps. This comparison indicates that most of the total mass of the cluster is due to a large component of non-interacting (except through gravity) matter which is mostly separate from the X-ray emission. This separation is considered direct evidence of DM. From [36] . . . . . 8
1.3 The galaxy distribution obtained from spectroscopic redshift surveys and from mock catalogues constructed from cosmological simulations. The small slice at the top shows the CfA2 "Great Wall," with the Coma cluster at the centre. Drawn to the same scale is a small section of the SDSS, in which an even larger "Sloan Great Wall" has been identified. This is one of the largest observed structures in the Universe, containing over 10,000 galaxies and stretching over more than 1.37 billion light years. The wedge on the left shows one-half of the 2dFGRS, which determined distances to more than 220,000 galaxies in the southern sky out to a depth of 2 billion light years. At the bottom and on the right, mock galaxy surveys constructed using semianalytic techniques to simulate the formation and evolution of galaxies within the evolving dark matter distribution of the Millennium simulation are shown, selected with matching survey geometries and magnitude limits. From [89]. 10
1.4 Comparison of running gauge couplings in SM (left) and MSSM (right). From [43] . . . . . 17

1.5 Schematic illustration of WIMP annihilation through hadronization (left) and directly into gamma rays (right), and of the analysis chain used in the Fermi collaboration. The double question mark indicates high uncertainty in models of dark matter density and new particle theories. From [17] . . . . . 21
1.6 The gamma ray spectrum per annihilation for a 100 GeV (left) and 500 GeV (right) WIMP. Each curve denotes the result for a different dominant annihilation mode. From [38] . . . . . 21
1.7 Comparison of density profiles, $r\rho(r)$ vs $r$, for a given density normalization $\rho_0 = 0.3$ GeV/cm$^3$ at 8.5 kpc, the distance from the solar system to the galactic center. From [18] . . . . . 24
1.8 Via Lactea II projected DM density squared map. An 800 kpc cube is shown. The insets focus on an inner 40 kpc cube in local density (bottom) and local phase space density (top). Image brightness is proportional to the log of the squared dark matter density along the line-of-sight. The mass resolution is 4,100 $M_\odot$, and the mass within $r_{200}$ (402 kpc) is $1.9 \times 10^{12} M_\odot$. From [37] . . . . . 26
1.9 Aquarius projected DM density squared map of an approximately 1 Mpc cube at $z = 0$. Mass resolution is 1,700 $M_\odot$ and mass within $r_{200}$ (245 kpc) is $1.84 \times 10^{12} M_\odot$. From [90] . . . . 27

2.1 Schematic cutaway view of the LAT showing the micrometeoroid shield, ACD, and towers (left), and a picture of the 16 towers in the grid (right) before the ACD assembly. From [82]. 33
2.2 Schematic view of the Large Area Telescope silicon tracker. Each tower includes 19 tray structures constituting the basic mechanical framework and housing both the silicon detection planes and the converter foils. From [82]. . . . . 33
2.3 Event display of a simulated 27 GeV gamma ray (a) and zoom over the calorimeter (b) and tracker (c) portions of the event. The small crosses represent the clusters in the tracker, while the variable-size squares indicate the reconstructed location and magnitude of the energy deposition for every hit crystal in the calorimeter. The dotted line represents the true gamma ray direction, the solid line is the calorimeter axis, and the dashed lines are the reconstructed tracker tracks. The backsplash from the calorimeter generates tens of hits in the tracker, with two spurious tracks reconstructed in addition to the two associated with the gamma ray (note that they extrapolate away from the calorimeter centroid and do not match the calorimeter direction). It also generates a few hits in the ACD, which, however, are away from the vertex direction extrapolation and therefore do not compromise the ability to correctly classify the event as a gamma ray. From [6]. . . . . 39

2.4 LAT $A_{eff}$ integrated over the FoV as a function of energy at successive stages of the event filtering as estimated with simulated data. Since we require a direction and energy to use a gamma ray for science analysis we consider only events with at least one track found and that pass the fiducial cuts. From [6]. 44
2.5 Best estimates of differential rates of residual particle backgrounds for the Source (a), Clean (b), and Ultraclean (c) event classes. Individual contributions from primary CR protons, primary CR electrons, and secondaries from CR interactions are shown. The corresponding count rates for the extragalactic gamma ray background measured by Fermi in [4] are also overlaid for comparison. From [6]. . . . . 44
2.6 68% (solid) and 95% (dash) PSF containment for normal-incidence photons as a function of incident energy (left), and for 10 GeV photons as a function of incident angle (right) for P7SOURCE_V6 IRFs. From [106]. . . . . 48
2.7 68% energy containment for normal-incidence photons as a function of incident energy (left), and for 10 GeV photons as a function of incident angle (right) for P7SOURCE_V6 IRFs. From [106]. . . . . 48
2.8 Effective area for normal-incidence photons as a function of incident energy (left), and for 10 GeV photons as a function of incident angle (right) for P7SOURCE_V6 IRFs. From [106]. . 49

3.1 Cumulative distribution of $\mathrm{TS}_{ext}$ for point sources simulated on top of Galatic diffuse and isotropic background, compared to the $\chi^2_1$ prediction of Chernoff's theorem. Sources of four different power-law spectra were simulated in the range 1 to 100 GeV, with fluxes selected such that the TS of source detection $\sim 50$. The sources have random positions on the sky within 5° of the galactic plane. From [56] . . . . . 57
3.2 Two flowcharts; the top illustrates the broader analysis chain, the "source analysis" block of which is shown in more detail in Figure 3.3; the bottom outlines the calculation of limits set on cross-section for a non-detection. . . . . 63
3.3 Flowchart illustrating our source testing procedure. The spatial test on the left is relatively straightforward and described in section 3.3.3. The spectral test on the right draws from a large set of simulations, and will be explained in detail in section 3.3.4. 64
3.4 Best-fit exponentially cutoff power law (with $\Gamma = 1.22$ and $E_{cut} = 1.8\,\mathrm{GeV}$) of the millisecond pulsar 1FGL J0030+0451 (solid line) and the best-fit $b\bar{b}$ spectrum (with $M_{\mathrm{WIMP}} = 25GeV$) of this pulsar (dashed line). From [8] . . . . . 71

3.5 Plot showing the range of flux/index values of LAT candidate sources (circles) and the space of simulated point power-law sources used to ascertain $\mathrm{TS}^{99}_{comp}$ (small crosses). The sources are also color-coded based on whether they pass the $TS_{PL} > 25$ cut, which shows where the limit of detection of point power-law sources is for our test. The consistency of this limit between LAT sources and simulated sources is a good check on this part of our analysis. . . . . 72
3.6 Example of how $\mathrm{TS}^{99}_{comp}$ is found. The top figure shows in blue crosses the set of simulated power-law sources, and in red crosses the specific selection of the 500 nearest simulated point power law sources whose $\mathrm{TS}_{comp}$ are to be tested against. The bottom figure is a cumulative histogram of those $\mathrm{TS}_{comp}$ values, and the red line marks 99th percentile value, our $\mathrm{TS}^{99}_{comp}$ for that source. . . . . 73
3.7 Color map of $\mathrm{TS}^{99}_{comp}$ for $b\bar{b}$ and $\tau^+\tau^-$ annihilation. The flux/index range was sampled and $\mathrm{TS}^{99}_{comp}$ was calculated for each sampled point, and then bicubic interpolation was done to fill in the map. The darker regions indicate where $\mathrm{TS}^{99}_{comp}$ is largest, i.e., where fluctuations in the null hypothesis spectrum are more likely to resemble DM annihilation. . . . . 75

4.1 Example of efficiency calculation. A point in the parameter space was selected, (flux,ext) = $(3 \times 10^{-9}, 2)$, and a circle is drawn around it containing the nearest 500 sources in parameter space. The efficiency at this point is the fraction of sources inside which pass our tests. In this case it is $\sim 0.65$ . . . . . 81
4.2 Color map for the spectral test efficiency only. . . . . 82
4.3 Color map for the extension test efficiency only. . . . . 83
4.4 Color map of efficiency . . . . . 85
4.5 Color map of efficiency, showing where satellites from one realization of the Aquarius N-body simulation fall for 50 GeV $b\bar{b}$ and $\tau^+\tau^-$ models, both with a $\langle\sigma v\rangle$ of $5 \times 10^{-25}$. Annihilation through the $\tau^+\tau^-$ channel for this mass produces fewer gamma rays per event by a factor of about 7 compared to the $b\bar{b}$ channel, so the subhalo flux is smaller by the same factor. . 87
4.6 95% confidence upper limits from our analysis, compared to the limit set in the previous analysis (black square) and the thermal relic cross-section . . . . . 89

# List of Tables

2.1 LAT event classes . . . . . 45

4.1 95% confidence upper limits on $\langle \sigma v \rangle$ for the 8 DM models examined . . . . . 88

**Abstract**

SEARCH FOR DARK MATTER SATELLITES OF THE MILKY WAY WITH THE FERMI LAT

by

Sheridan Zalewski

The nature of Dark Matter is one of the most significant outstanding questions in cosmology; current estimates are that over 80% of the matter of the universe is composed of an invisible heavy particle whose nature is unknown. Numerical simulations of the evolution of structure in the universe, based on the ΛCDM model of cosmology, predict that the mass of galaxies like the Milky Way are dominated by large DM halos extending far beyond the luminous disk, and that these halos are clumpy: they have a significant amount of mass in the form of "subhalos," also called DM satellites.

A convenient candidate particle for DM is provided by Supersymmetry (SUSY), an extension of the Standard Model (SM) of particle physics which posits that each SM fermion has a partner SUSY boson, and vice versa. In many SUSY theories, the lightest supersymmetric particle (LSP) is stable and is its own antiparticle, pair-annihilating into gamma rays. The Fermi Large Area Telescope (LAT) has generated an active area of study in the search for this DM annihilation signal. The signal from DM satellites of the Milky Way would appear as gamma ray sources with no counterparts at other wavelengths, and would have a distinct spectrum and resolvable spatial extension. In this dissertation, we present results on the analysis of unassociated LAT sources, and what constraints can be set on different DM candidates in the case of a non-detection.

For Mom and Dad

## Acknowledgments

First and foremost, I want to thank my adviser Robert Johnson for his patience and trust, and for supporting me for so long. Many thanks also to the other members of my thesis committee, Steve Ritz and Stefano Profumo, who gave me useful comments on my thesis drafts and straightforward general advice. I also greatly appreciate the patience and understanding shown to me by Michael Dine and the physics department administration, who accomodated my leave of absence and return. My colleagues at Stanford, Alex Drlica-Wagner and Joshua Lande, have been indispensable in putting this analysis together, and I thank them for always being available and willing to help out. Thanks to Elliott Bloom who brought me on to work on the first satellites paper and helped me get and maintain a computing account at SLAC, without which this project would have taken months longer. This analysis would of course not be possible without the work of numerous and diverse people and groups in the Fermi Collaboration, and I thank all of them. And lastly I am grateful for all the love and support shown to me by my friends and family over the years.

# Introduction

*The most exciting phrase to hear in science, the one that heralds new discoveries, is not "Eureka" but "Thats funny..."*

Isaac Asimov

Asimov's observation is especially apt for the story of Dark Matter (DM). It began as a minor puzzle in 1933 which was not thought to be of much significance, and has become one of the most significant outstanding questions in modern physics. It is deserving of this status not just because of its major implications in both particle physics and cosmology, but also because it is suggestive of how much of the universe is not yet understood: current estimates are that over 80% of the matter of the universe is composed of an invisible heavy particle whose nature is unknown. Thus the use of the term "Dark Matter" resembles the marking of maps with "Terra Incognita" to represent land that was known merely to exist.

Although the nature is unknown, there are patterns in the distribution of DM as well as observations from cosmology that give us hints. Results on the early universe and structure formation put constraints on models of DM and led to the development of the now-standard ΛCDM paradigm. N-body simulations assuming ΛCDM have been used to predict the structure of DM in the universe down to the sub-galactic scale by simulating the evolution of dark matter structures from early times to present day, and show that the mass of galaxies like the Milky Way are dominated by DM halos. These halos have a significant amount of substructure in the form of gravitationally bound

subhalos. Supersymmetric (SUSY) extensions of the Standard Model provide a convenient candidate for DM, so-called Weakly Interacting Massive Particles (WIMPs), in addition to being well-motivated theoretically in several other ways. In many models, this particle self-annihilates into gamma rays, which could be used for indirect detection of DM; subhalos may be detectable as gamma ray sources.

Data from the Fermi Gamma-ray Space Telescope (Fermi) have generated an active area of study in the search for signals of this annihilation. Fermi was launched by NASA on June 11, 2008 from Cape Canaveral, and contains two instruments on board, the Gamma-ray Burst Monitor (GBM) for detecting gamma ray flares, and the Large Area Telescope (LAT), which is the main gamma ray detection instrument. The LAT is a pair-conversion detector, in which gamma rays incident on tungsten foils produce electron-positron pairs that are tracked by silicon strip detectors. It has the capability to detect gamma rays in the range from 20 MeV to over 300 GeV, and cosmic rays up to 3 TeV. Its field of view is about 20% of the sky, and in normal operation scans continuously, covering the full sky in about 3 hours.

The goal of this thesis shall be to establish and carry out a method for analyzing gamma ray sources in search of a candidate for a DM subhalo, and to rule out regions of WIMP parameter space in the case of a non-detection. We present this search for dark matter using 3 years of data from the Fermi LAT among unassociated sources in the LAT catalog, working with the hypothesis that DM is composed nearly entirely of LSP WIMPs in the mass range such that their self-annihilation spectrum falls in the detectable range of the LAT, and that their spatial distribution and density profiles are well-represented by recent N-body simulations such as Via Lactea II and Aquarius. Chapter 1 is dedicated to the history and evidence for DM, SUSY and its candidate DM particles, and N-body simulations and large-scale structure of the universe. In

Chapter 2 we detail the structure, subsystems, and performance of the Fermi LAT gamma ray detector. Chapter 3 explains the general likelihood methods for analyzing LAT data and the specific source analysis we use to attempt to discern DM subhalos from other astrophysical sources. And in Chapter 4 we discuss and interpret the results of our analysis. This work builds on and expands the analysis of [8].

# Chapter 1

# Dark Matter - evidence, models, simulations

## 1.1 History

Although the problem was not then described in its present formulation, the earliest hint of cosmological dark matter is generally credited to observations by Fritz Zwicky [105] in 1933 of the velocities of galaxies in the Coma cluster. The velocity dispersion is related to the total gravity of the cluster inside the orbit, and Zwicky found that the cluster's mass calculated this way was an order of magnitude greater than the summed mass of the individual galaxies in the cluster. This suggested the presence of a huge amount of invisible mass.

Several subsequent observations [87, 104] of radial velocities in clusters were consistent with this result, but the problem did not advance in status from nagging observational puzzle to major cosmological problem until the 1970's, when it became possible to measure the rotation curves of galaxies out to large distances. According to Kepler's Law, if the mass of the galaxy were mostly in the stars and dust, the rotational velocities of objects on the periphery of the galaxy should fall as $r^{-1/2}$. It was noticed as early as 1939

[16] that the outer regions of the Andromeda galaxy were rotating significantly faster than the Keplerian velocity, but using new sensitive instruments, Vera Rubin and Kent Ford were able to measure Andromeda's rotation curve to a very far distance from the center, and showed that it remained constant out to 8-10 times the distance of visible stars in the disk [78], shown in figure 1.1. Observations of more spiral and elliptical galaxies produced the same result [77, 41], suggesting that the bulk of the mass in galaxies was contained in a spherical halo around the galaxy. Photometry is used to estimate mass based on luminosity, through well-defined mass-to-light ($M/L$) ratios. These are defined according to some baseline ratio (usually the Sun) in some spectral band (e.g., blue light). Using the data from the rotation curves and from photometry, the local values of $M/L$ can be found. In the periphery, the very high rotation speeds lead to $M/L$ values around 200, compared to $M/L \sim 1$ which might be expected from the old metal-poor stars that dominate the periphery. In contrast, $M/L \sim 2-3$ in the central regions of galaxies.

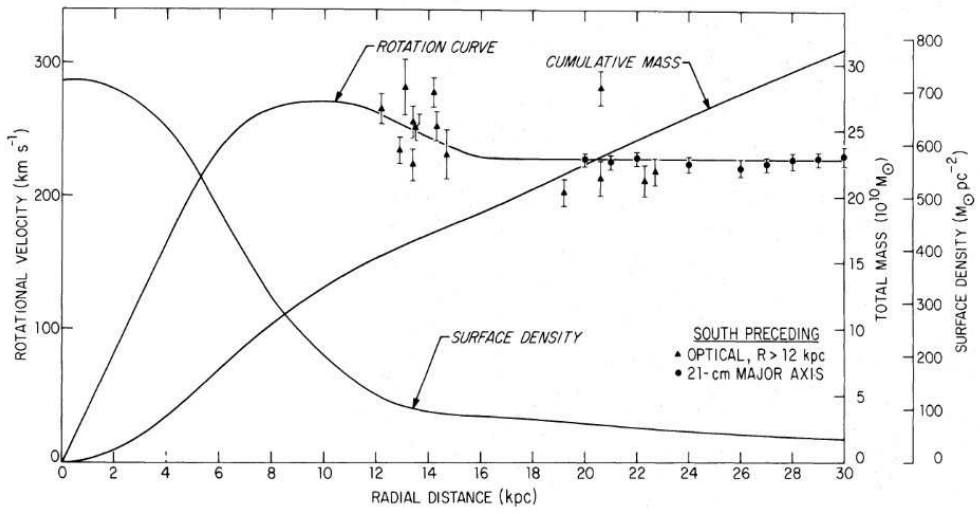


Fig. 1.1: The rotation curve of M31, published in [75], using the optical data of Rubin & Ford [78].

Early attempts to explain the missing mass posited some yet undiscovered

population of very dim stars in the halo, such as neutron stars and brown and white dwarfs, which came to be collectively called MACHOs (MAssive Compact Halo Objects). Several lines of evidence followed which argued that the mass could not be mainly composed of such a population of stars, and that it must be non-baryonic in nature. Searches for MACHOs have been carried out by several collaborations, of which the MACHO Collaboration [11] and the EROS-2 Survey [96] were historically the first. These collaborations searched for microlensing of stars in the Large Magellanic Cloud to detect these objects. Microlensing is a kind of gravitational lensing, a distortion of background image by the gravitational effects of a foreground object. In microlensing, no obvious distortion is apparent in the image, but is detected from changing amounts of light in time from the background source. These two studies concluded that the fraction of halo mass from MACHOs was 20% and 8% respectively, and strongly ruled out a 100% MACHO halo. Further searches for MACHOs were conducted with the Hubble Space Telescope using gravitational lensing in star clusters, which found that only about 6% of the stellar mass is in brown dwarfs [63].

A further theoretical argument against MACHOs followed: Models of galactic evolution [40, 95] show that the $M/L$ of a given stellar population depends critically on the lower mass limit $m_0$ at which stars in that population form. This limit was found not to change very much even over a large range of physical conditions [40], and to get the very large required $M/L$ values suggested by rotation curves, a $m_0$ much smaller than that of any known population would be necessary. This by itself is not problematic. However, stellar populations of different age and metallicity form continuous sequences in physical and kinematic properties (as in a Hertzsprung-Russell diagram). In the context of this fact it is difficult to explain the stellar and kinematic properties of a stellar dark halo. Dark halo stars must have a very high velocity dispersion

compared to the stars in the disk, which would be a large discontinuity in the dispersion-$M/L$ sequence, indicating that the origin of these stars would have to be much older than any known population (i.e., they would be "population III" stars). Recent calculations suggest that population III stars should instead be very massive [73], and therefore are unsuited to represent a present high $M/L$ population.

These arguments are strong evidence against known kinds of baryonic objects like brown dwarfs and neutron stars, but still leave open the possibility of some unknown form of baryonic matter. Nucleosynthesis however, provides a tight constraint on the baryon fraction of the universe, $\Omega_b = 0.04$ [80], which is much smaller than the total amount of matter, $\Omega_m = 0.2 - 0.3$. The Cosmic Microwave Background Radiation (CMBR) allowed measurement of the density fluctuations in the early universe, and there must be sufficient mass in the universe in order to account for present structure from initial fluctuations. For the baryons alone to be able to account for the present structure, the initial density fluctuations must be on the order of $10^{-3}$. As measurement of the initial fluctuations improved, the upper limits descended below this, and thus baryons alone would have been too slow in achieving the necessary gravitational collapse [49]. The best single piece of evidence for non-baryonic DM came from observations by the Chandra X-Ray Observatory of a cluster merger, the Bullet cluster, shown in figure 1.2. Comparing the gravitational lensing maps (which track the mass) with the X-ray gas maps (which track the baryons, as the gas is the dominant baryonic component of clusters) shows an obvious separation of the baryons from the main distributions of mass. This offset between the baryons and the large massive substructures very strongly suggests that the baryons make up only a fraction of the total mass, so the vast majority of the mass is collisionless and contained in a non-baryonic halo [36]. Despite the violent merger, the $M/L$ in the DM halos is similar to other

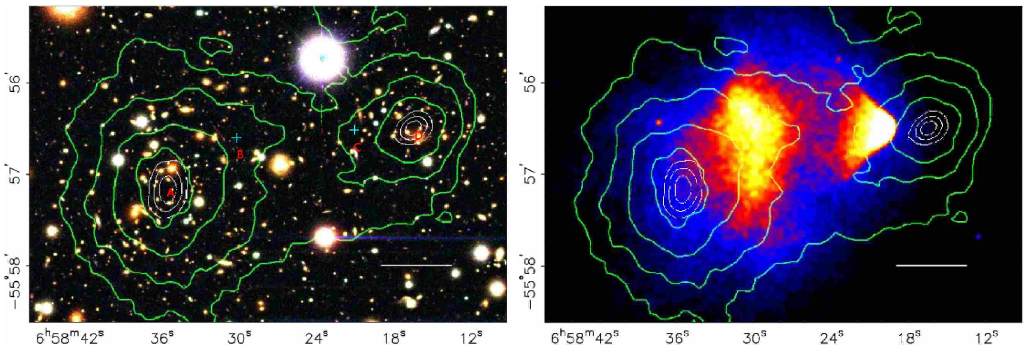


Fig. 1.2: Two images of the bullet cluster. On the left is the optical image of the individual galaxies. The majority of the baryonic mass of the cluster however is in the two clouds of hot X-ray emitting gas, shown on the right in the Chandra map. The green countours are the gravitational lensing maps. This comparison indicates that most of the total mass of the cluster is due to a large component of non-interacting (except through gravity) matter which is mostly separate from the X-ray emission. This separation is considered direct evidence of DM. From [36]

clusters, which implies that the dark matter is completely decoupled from the hot baryonic plasma tracked by the X-Ray gas maps. Observations of other cluster collisions have since corroborated these results [29].

Since DM is the bulk of the mass budget of the universe, its properties determine much of the formation and evolution of structure in the universe. Zel'dovich was among the first to discuss this [102], and proposed that matter first coalesces into pancakes, and then these fragment into smaller structures. Rivaling this theory was the hierarchical clustering theory by Peebles [71], in which small structures (on the order of star clusters) form first and then cluster together. As the evidence for DM accumulated, it became clear that whether DM particles were relativistic ("hot") or not ("cold") when they thermally decoupled from the rest of the universe, would have a profound impact on how structure formed in the universe. In Hot Dark Matter, where usually the DM is neutrinos, the very high velocities of the particles prevent small-scale density perturbations from forming early or efficiently. Superclusters and galaxies then form relatively late, which is at odds with the measured

age of old stellar populations. The Cold Dark Matter scenario, originally published by Blumenthal et al in 1984, allowed for this structure formation [26]; small dwarf galaxies form first, and large galaxies and structure form from a succession of mergers.

Later, observations of distant supernovae [74, 72] showed that the expansion of the universe is accelerating, which led to a cosmological constant $\Lambda$ (identified with dark energy) being incorporated into the paradigm, now called $\Lambda$CDM. The predictions of large-scale structure formation in $\Lambda$CDM cosmology as realized in the Millennium-II Simulation, a very large N-body simulation of DM from $z = 127$ to today [28], have been very successful in matching observation (Figure 1.3). The more recent and powerful Bolshoi simulation [53], using updated values for cosmological parameters, has been able to account for a wide range of phenomena [98]. The major question has become the nature of DM itself.

## 1.2 Modified gravity as an alternative to DM

There are theories which attempt to explain the gravitational phenomena held to be evidence of DM instead in terms of modified gravity. The Modified Newtonian Dynamics (MOND) scheme was proposed by Milgrom in 1983 as a way to explain the rotation curves of galaxies [60]. The idea behind MOND is that the acceleration $a$ of a test particle by a gravitational field depends on the form $m/\tilde{\mu}(a/a_0)$ instead of simply $m$, where $a_0$ is a natural scale, about $10^{-10}\,\mathrm{m/s^2}$, and $\mu$ is some function which approaches unity for large arguments and $a/a_0$ for small arguments, so that acceleration is not linearly proportional to gravity at small values. Two widespread choices are $\mu(x) = \frac{x}{1+x}$ and $\mu(x) = \frac{x}{\sqrt{1+x^2}}$.

Remarkably, MOND also provides an explanation for the Tully-Fisher rela-

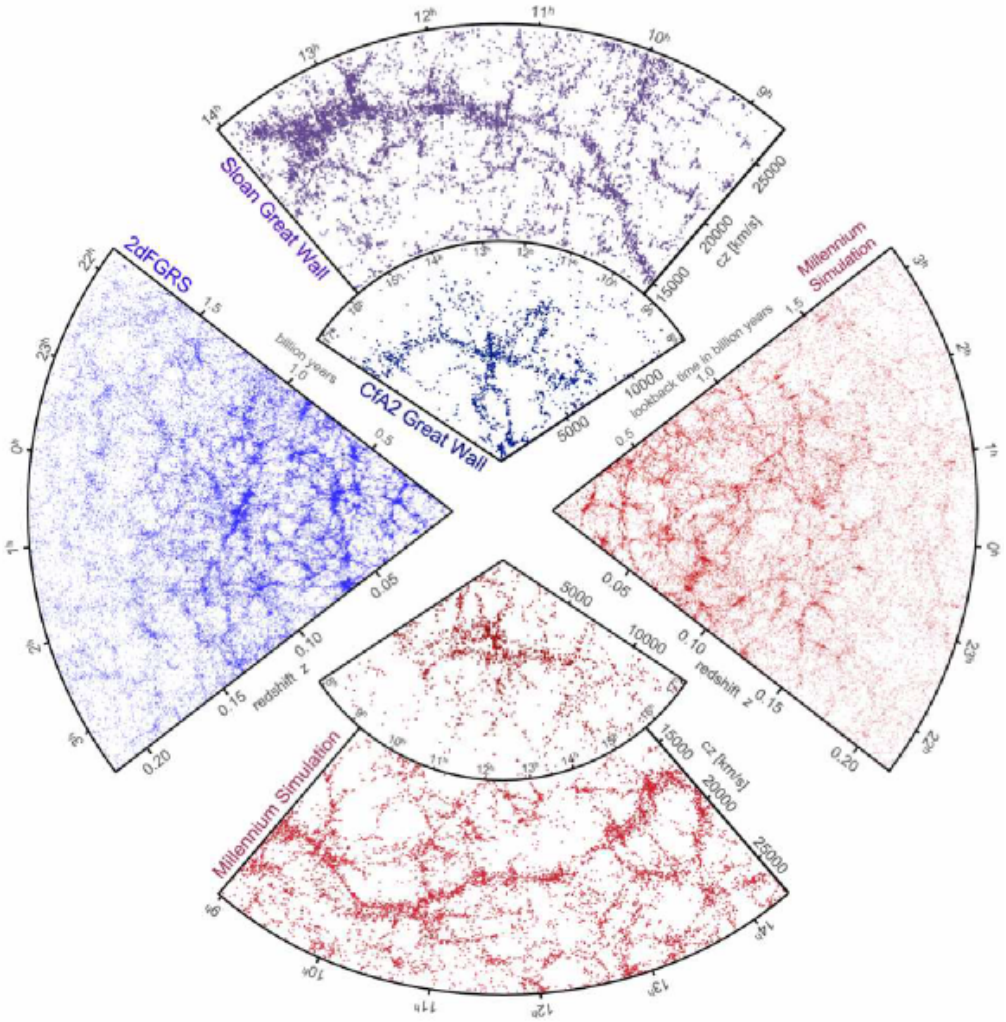


Fig. 1.3: The galaxy distribution obtained from spectroscopic redshift surveys and from mock catalogues constructed from cosmological simulations. The small slice at the top shows the CfA2 "Great Wall," with the Coma cluster at the centre. Drawn to the same scale is a small section of the SDSS, in which an even larger "Sloan Great Wall" has been identified. This is one of the largest observed structures in the Universe, containing over 10,000 galaxies and stretching over more than 1.37 billion light years. The wedge on the left shows one-half of the 2dFGRS, which determined distances to more than 220,000 galaxies in the southern sky out to a depth of 2 billion light years. At the bottom and on the right, mock galaxy surveys constructed using semianalytic techniques to simulate the formation and evolution of galaxies within the evolving dark matter distribution of the Millennium simulation are shown, selected with matching survey geometries and magnitude limits. From [89].

tion with this same scale [19]. Tully-Fisher is the observation that the baryonic mass of a disk galaxy is proportional to the fourth power of the terminal rotational velocity of that galaxy. The scale introduced to explain rotation curves also enters into the proportionality of this relation in the context of MOND, and agrees well with observation. Importantly, these two parameters did not necessarily have to have anything to do with one another, but the MOND paradigm provides a common origin for them. This is an elegant dynamical explanation for Tully-Fisher, whereas it has been difficult to find a reason for the relation to emerge from galaxy formation with DM, making MOND an attractive alternative to consider.

The embodiment of MOND into a covariant theory started with a modification of the Newtonian (i.e., non-relativistic) field Lagrangian (AQUAL) such the gradient of the scalar field recovers the $\mu(x)$ equation. To make it covariant, the Lagrangian is made covariant, and the scalar field augmented suitably. Further refinements led to tensor-vector-scalar (TeVeS) theory [20], the standard relativistic MOND paradigm (though others exist).

TeVeS has been tested observationally via gravitational lensing. Generally, TeVeS does well in accounting for strong gravitational lensing [103], but has difficulty fitting observations of weak gravitational lensing in galaxy clusters [64] (e.g. the Bullet Cluster shown above). Another test for MOND has been in cosmology; dark matter plays such a large role in cosmology and the evolution of structure that a major outstanding question for MOND was whether it would be able to account for, e.g., the observed structure in the background radiation . In [86] it was shown that TeVeS can reasonably well account for evolution of perturbations into observed spatial distribution of structure, though several differences between GR and TeVeS cosmology exist, and future observations will be able to test these.

## 1.3 DM particle candidates

The success of ΛCDM cosmology gives a set of conditions that a good candidate of particle DM should satisfy, namely that it is cold, neutral, is consistent with Big Bang nucleosynthesis, has the appropriate relic density, and is consistent with a variety of astrophysical bounds (see [94] for a more extensive test). The two most popular candidates are axions and weakly interacting massive particles (WIMPs), although there is a host of other candidates such as sterile neutrinos, or particles in a still hidden sector of physics [42].

### 1.3.1 Axions

Axions are hypothetical particles that arise in Peccei-Quinn theory, which attempts to resolve the strong CP problem. This is the observation that in order for QCD to preserve $P$ and $CP$ symmetry, in accordance with observation, the $\theta$ parameter in the QCD Lagrangian must be fine-tuned to a factor of $10^{-9}$. Peccei and Quinn [70] proposed a solution in which they posited a chiral $U(1)$ invariance — under this symmetry, changes in $\theta$ are equivalent to changes in the definitions of the fields in the Lagrangian, so this would have no observational consequence, obviating the fine-tuning problem. This symmetry is spontaneously broken at some scale $f_a$, and the axion is the corresponding Nambu-Goldstone scalar boson. The mass of the axion is experimentally constrained to be less than about $3 \times 10^{-3}$ eV by consideration of how stars and supernova cores would cool by axion emission [69], and to be greater than about $10^{-6}$ eV to effect density perturbations consistent with the CMBR observations [84]. Although very light, axions are cold because they are produced non-thermally by the "misalignment mechanism." The axions are massless at temperatures above the QCD phase transition, and as the temperature drops below about 1 GeV, the axion field acquires a mass

$m_a$ due to instanton effects. The field will begin to oscillate about an initial misalignment angle $\alpha_1$ once $m_a$ becomes comparable to the Hubble parameter $H$, and these coherent oscillations transform the energy stored in the field into physical axion quanta. The resulting axion relic density is [84]:

$$\Omega_a = 0.15\Big(\frac{f_a}{10^{12}\,\mathrm{GeV}}\Big)^{7/6}\alpha_1^2 \tag{1.1}$$

### 1.3.2 WIMPs

WIMPs are hypothetical particles which are very massive, very stable, and which only interact through gravity and the weak force. WIMPs are features of many extensions of the Standard Model such as Supersymmetry (SUSY) and Kaluza-Klein theory. Depending on the theory, the relic density of a WIMP species $\chi$ can be produced thermally in the standard freeze-out scenario (the focus of this thesis), or non-thermally, such as from decays of other particles, or gravitational mechanisms [35]. In many theories, the WIMP is its own antiparticle, and can produce detectable photons in pair-annihilation.

In the thermal production scenario, when the temperature of the universe is higher than the WIMP mass $m_\chi$, WIMPs are pair-produced by particle-antiparticle collisions in the thermal plasma, and these reactions are in equilibrium with WIMP annihilation reactions. As the universe cools, only the particles in the tail of the Boltzmann distribution remain energetic enough to contribute to this production, and so the rate of this production decreases exponentially. As this is happening, the universe is expanding, and eventually this expansion outpaces the WIMP annihilation rate, and the number of WIMPs (per comoving volume) reaches its final value—the WIMPs have "frozen out" and we obtain the present relic density. The rough criterion for this happening is that the interaction rate be less than the expansion rate of the universe, or $\Gamma < H$. To find out when this happens, we must solve the

Boltzmann equation for a theoretical particle model and then require that the relic density of that particle equal that of dark matter, $\Omega_{DM} \sim 0.3$. By making certain reasonable approximations [39], the Boltzmann equation may be cast in the form:

$$\frac{dY}{dx} = -\frac{\lambda}{x^2}\{Y^2 - Y_{EQ}^2\} \tag{1.2}$$

where the only unknown is $Y$, the entropy density, defined by $Y = n_\chi/T^3$ with $n$ the number density of particle $\chi$. $Y_{EQ}$ is the value of $Y$ at equilibrium (before freeze-out), $x = m_\chi/T$, and $\lambda$ is the parameterization of the ratio of annihilation rate to expansion rate,

$$\lambda = \frac{m^3 \langle\sigma v\rangle}{H(m)} \tag{1.3}$$

where $\langle\sigma v\rangle$ is the thermally-averaged cross-section, and $H$ is the Hubble expansion rate. The goal is then to find $Y$ at present day, or very low temperature: $Y(x \sim \infty)$, which when divided by $\Omega_{crit}$ gives the fraction of the energy density contributed by the WIMP, $\Omega_\chi$. Setting this equal to $\Omega_{DM}$ then allows us to calculate the required cross-section. Presently, the relic density of WIMPs is estimated to be approximately [25]:

$$\Omega_\chi h^2 \sim 3 \times 10^{-27} cm^3 s^{-1} / \langle\sigma v\rangle \tag{1.4}$$

where $h = H_0/(100km\ s^{-1}\ Mpc^{-1})$. This gives us a cross-section that happens to be typical of weak interactions at the electroweak scale, which comes out of the cosmology independent of any detailed assumption of particle physics - this suggestive coincidence is sometimes called the "WIMP miracle."

## 1.4 Non-SUSY WIMP models

WIMPs can come from a diverse range of theories. Here we summarize some of the more studied models, before talking more at length about Supersymmetry, the theory considered in this thesis. There are a plethora of other theories besides these which can generate WIMPs, which we cannot list exhaustively, but refer to [25].

Massive neutrinos were early popular candidates for their "undisputed virtue of being known to exist" [22], in contrast to nearly all others. As it became clear that neutrinos were too hot ($v \sim c$) and not abundant enough to account for the observed structure, one approach was to minimally extend the SM by adding a multiplet with only weak interactions instead of positing new discrete symmetries. The straightforward option is sterile neutrinos, a fourth generation which does not interact with SM particles weakly except through mixing. Constraints on sterile neutrinos from cosmology and astrophysics are detailed in [1].

In Kaluza-Klein theory, gravity and electromagnetism are unified in a five-dimensional spacetime. One of these dimensions is compactified, and the different modes of standing waves on this dimension would appear as a set of particles called the Kaluza-Klein tower. To maintain stability of these particles (which would otherwise decay into SM particles), a symmetry called KK-parity is imposed, which is conservation of momentum along the extra dimension. The lightest Kaluza-Klein particle (LKP) is then stable. The most studied example is often called the KK "photon" (really the KK hypercharge gauge boson $B_1$). Several studies have been carried out regarding their relic density and direct/indirect detection [81, 33].

In "Little Higgs" theories [79], the quadratic divergences in calculating the Higgs mass are alleviated by global symmetries in an extended electroweak

sector. The new particles ensure that this symmetry isn't broken too severely, and these particles cut off the divergences in the Higgs loops. The DM candidate comes from the introduction of T-parity, under which the new heavy particles have odd parity, and SM are even - thus the lightest T-odd particle is stable as the symmetry disallows decay into anything lighter.

## 1.5 Supersymmetry and WIMPs

Supersymmetry is a hypothetical symmetry in which all Standard Model particles have partner particles differing by a half-unit of spin; SM bosons have corresponding SUSY fermions, and vice versa. The suggestion that SUSY could provide a DM candidate was made as early as 1982 [67]. In SUSY, in order to keep protons stable it is generally necessary to impose an additional symmetry called R-parity which is preserved in all reactions. R-parity is multiplicatively conserved, and defined as:

$$R = (-1)^{3B+L+2s} \tag{1.5}$$

where $B$ is the baryon number, $L$ the lepton number, and $s$ the spin of the particle. Then, SM particles have R-parity 1 and SUSY particles have -1 (as they have a half-unit different spin). Because of this symmetry, the lightest supersymmetric particle (LSP) must be absolutely stable, since there are no lighter SUSY particles to decay into and decay into SM particles would violate R-parity.

Although there is no direct evidence at present for SUSY, it is one of the most well-motivated extensions of the SM, as it has the potential to solve several theoretical and observational puzzles besides providing a good DM candidate in the LSP. There are several flavors of SUSY, and in this thesis we consider the minimal extension of SM with SUSY, the so-called Minimal

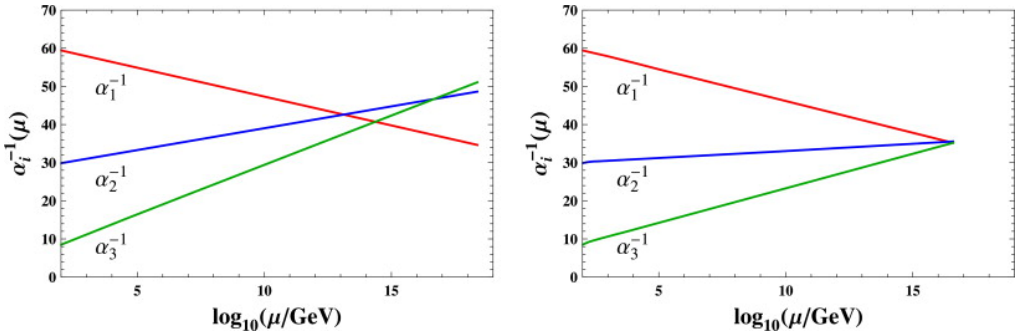


Fig. 1.4: Comparison of running gauge couplings in SM (left) and MSSM (right). From [43]

Supersymmetric Standard Model (MSSM). MSSM was in fact originally motivated by the realization that it could aid in solving the hierarchy problem, the required fine-tuning of the necessary cancellations of the divergences that arise in calculating loop corrections to the Higgs mass [59]. Additionally, and just as important, adding SUSY particles adjusts the beta-functions of the gauge couplings of SM forces in such a way as to unify at a higher energy scale (figure 1.4), whereas it is known that this fails to happen in the SM [12]. As mentioned, in MSSM, we impose the conservation of R-parity, which causes the LSP to be absolutely stable, and in the case where it is its own antiparticle, as will be considered in this thesis, is only destroyed via pair-annihilation.

The MSSM has many free parameters, and different parameters will result in different LSPs. It should also be noted that obviously SUSY is not a symmetry at everyday energy scales, and so it must be a broken at higher energy scales; the details of this symmetry breaking also affect which particle is the LSP. Given that we want to consider one that interacts only weakly and gravitationally, this narrows down the list of useful candidates to sneutrinos, gravitinos, and neutralinos, which are, respectively, the SUSY partners of the neutrino, the graviton, and the electroweak bosons. The sneutrino however is expected to a have relatively large cross-section for interactions with heavy nuclei, experiments for which so far have yielded a null result [48]. Typically,

the neutralino is the LSP, except in gauge-mediated SUSY breaking where it is the gravitino. In this thesis, we are concerned only with the neutralino LSP. While gravitinos interact only gravitationally, in some models it may decay into a photon and a photino, potentially allowing for indirect detection searches similar to this.

The neutralinos are the supersymmetric partners of the neutral SM bosons. There are 4 neutralinos, which are each different mixtures of the wino (partner of the neutral weak isospin boson $W_3$), the bino (partner of the weak hypercharge boson B), and two neutral Higgsinos (partners of the neutral components of the Higgs doublets, $H_1^0$ and $H_2^0$). In different regions of SUSY parameter space, the LSP neutralino will differ in which is the main part of the mixture. The neutralino is a Majorana fermion, its own antiparticle, and so self-annihilates. The mass of WIMPs is typically in the GeV range, so photons from annihilation would be in the gamma ray spectrum.

## 1.6 DM detection

Two general strategies for detecting WIMPs exist: direct and indirect. In direct detection, experiments look for evidence of WIMPs interacting directly with the detector apparatus. The two most popular detector technologies are cryogenic detectors and noble liquid detectors. In both cases, the experiments generally operate in deep underground sites (such as former mines) to reduce background from cosmic rays. Indirect detection looks for WIMP decay or annihilation products. These are often gamma rays (the focus of our analysis) or positrons, but neutrinos are a possibility as well; the IceCube neutrino observatory has been used to search for DM using a variety of methods [2].

### 1.6.1 Direct detection

Cryogenic detectors operate at temperatures below 0.1 Kelvin, and measure phonon and ionization signals produced when particles scatter off crystal absorbers. This allows the ability to distinguish between electron and nuclear recoils, as most of the background events will be of the former, while WIMP scattering is expected to be the latter. Examples of cryogenic detector experiments include SuperCDMS, EDELWEISS, and the planned EURECA experiment [31, 14, 54].

Liquid noble experiments consist of a large ($\sim$ 10 kg or more) target of noble gas cooled to liquid phase, and measure the scintillation in the liquid and its ionization. The ratio of the signals is different for nuclear and electron recoil events, allowing discrimination between signal and background. Examples of these experiments are XENON [13] and LUX [10].

Many other techniques also exist; the DAMA/LIBRA [24] experiment searched for a modulation of the event rate as the Earth orbits the Sun, as the velocity of the Earth relative to the DM halo will vary over the course of a year. See [93] for a more complete discussion and survey of dark matter experiments.

### 1.6.2 Gamma rays from neutralino annihilation

WIMPs can annihilate into directly into gamma rays and into several different kinds of pairs of SM particles, giving a spectrum with two components: monochromatic lines from direct annihilation into gamma rays, and continuum gamma rays from the secondary annihilation/decay of particles created in the annihilation. In this thesis, we consider only continuum gamma ray spectra, but here briefly talk about line production and recent searches for line signals.

### 1.6.3 Gamma ray lines

Since WIMPs are non-relativistic, annihilation directly into two photons gives back-to-back gamma rays with energy equal to the WIMP mass $m_\chi$ (with a very small spread). If such a line were observed in the gamma ray spectrum, it would be a "smoking gun" signature of dark matter. Annihilation into $\gamma Z$ and $\gamma H$ are also possible lines at energy $E_{\gamma(Z,H)} = m_\chi(1 - m_{Z,H}^2/(4m_\chi^2))$ but these have a spread in energy associated with the width of the $Z$ and $H$ bosons. These processes are at loop level, and so are suppressed by a factor $(\alpha/\pi)^2$ but there are certain models in which they are the dominant processes [47].

### 1.6.4 Continuum gamma ray production

The spectrum of gamma ray yield depends on the mass, cross-section, and annihilation channels (initial particles created) of the DM particle. As shown in figure 1.5, the annihilation first proceeds in one of the channels, then into mesons (primarily $\pi^0$) resulting from fragmentation or decay of the tree-level annihilation state. The dominant channels are typically (as kinematically allowed) $b\bar{b}$, $W^+W^-$, $\tau^+\tau^-$, $t\bar{t}$, and $ZZ$, as annihilation into light fermion is suppressed by the factor $(m_f^2/M_X^2)$. These depend on the model, of which there are myriad, but tools exist (e.g. Pythia [85]) to compute the number of continuum photons created, and these are fairly general to most Majorana fermion WIMPs, including the neutralino [32]. Figure 1.6 plots the spectra of these channels. We consider specifically the $b\bar{b}$ and $\tau^+\tau^-$ channels in this analysis, as $b\bar{b}$ is a good representative of several other channels, and $\tau^+\tau^-$ is very distinct from the others.

In cases where the WIMP annihilates into charged particles, it is also important to consider certain radiative corrections called internal bremsstrahl-

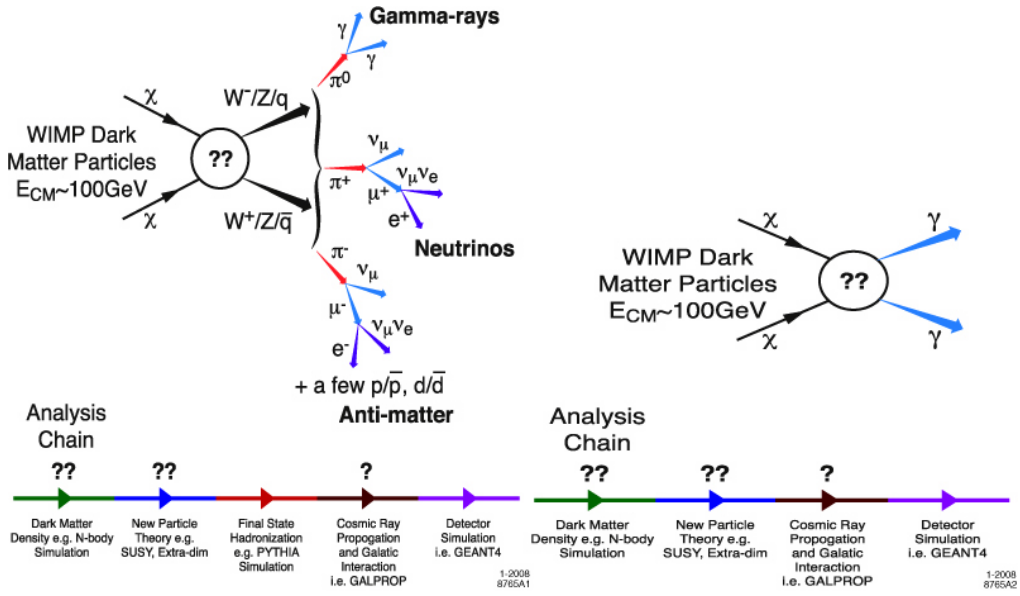


Fig. 1.5: Schematic illustration of WIMP annihilation through hadronization (left) and directly into gamma rays (right), and of the analysis chain used in the Fermi collaboration. The double question mark indicates high uncertainty in models of dark matter density and new particle theories. From [17]

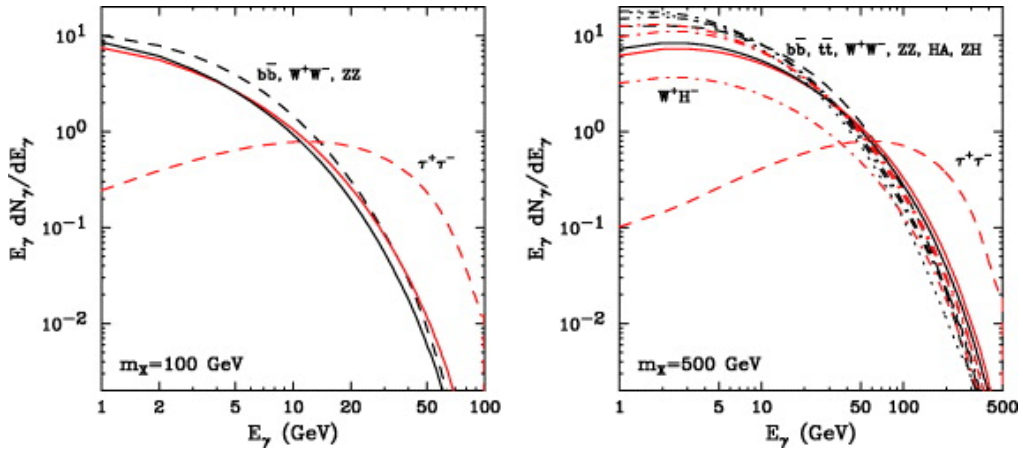


Fig. 1.6: The gamma ray spectrum per annihilation for a 100 GeV (left) and 500 GeV (right) WIMP. Each curve denotes the result for a different dominant annihilation mode. From [38]

ung. Radiation from the charged particles are referred to as final state radiation (FSR), and those from virtual particles (i.e. from somewhere in the double question mark region in figure 1.5) are internal bremsstrahlung (VIB). Models have been proposed [23] in which the bremsstrahlung from the virtual particle is actually the dominant process in annihilation, and may enhance the cross-section on the order of $10^4 - 10^6$. We do not consider such models here, but Fermi data have been used to search for VIB signals [30].

## 1.7 DM distribution and structure

To search for DM, we also need to know how DM is distributed in the universe, and how structure forms from the largest scales down to the subgalactic. As computing became cheaper and more powerful, several N-body simulations were done to this end over the last couple decades [37, 90, 28, 53, 65]. In particular we are interested in the structure of galactic DM halos. The Via Lactea II (VL2) and Aquarius projects are simulations of Milky Way-sized halos with the goal of studying how such halos evolve, and to compare predictions of ΛCDM cosmology with observation. VL2 follows the growth of a MW-size system from redshift $z = 104.3$ to the present, using cosmological parameters from 3 years of WMAP observations [88], using over one billion particles of mass $\sim 10^3 M_\odot$. Aquarius consists of six independent simulations of different halos selected from the Millennium-II simulation. It uses the same cosmological parameters, which are consistent with constraints from WMAP 1 and 5-year data analyses, although it used an early WMAP value of $\sigma_8$ which is now recognized to be too high [76]. Each halo was simulated at a multiple numerical resolutions, and one was simulated at a force and mass resolution 3 times greater than any other. VL2 was able to resolve subhalos down to the size of $10^5$ $M_\odot$, and Aquarius down to $10^{4.5}$ $M_\odot$.

Among the general results from these simulations is the observation that, as might be expected given the scale-invariant nature of gravity, the halos, subhalos, and sub-subhalos exhibit a great deal of self-similarity in their shape and substructure (although Aquarius, resolving four generations of subhalos-within-subhalos, reports less substructure in subhalos compared to the main halo). The spherically averaged halo density profile can be approximated over 20 mass decades with the same universal form, called the NFW profile [65]:

$$\rho(r) = \frac{\rho_0}{\frac{r}{r_s}(1+\frac{r}{r_s})^2} \tag{1.6}$$

This function behaves like a broken power-law which gradually changes from 3 in the outer parts to 1, asymptotically, in the inner parts, with $r_s$, the scale radius, defining the spatial scale of this transition, and $\rho_s$ a density normalization. The value of $r_s$ is often given in units of the virial radius, $r_{vir}$, and the reciprocal of that value is referred to as the halo concentration, $c_{vir} = r_{vir}/r_s$.

The inner profile is of particular interest as it is a test of ΛCDM cosmology, as the difference between cold and "tepid" or "warm" dark matter would only show up on this scale [58]. In addition to the NFW profile, other profiles such as the Moore, Einasto, and isothermal profiles have been considered. A comparison of these is shown in Figure 1.7. VL2 found the inner profiles of the main halo and subhalos were more cuspy than the NFW profile, with index scatter around $\gamma = 1.2$, whereas Aquarius found the inner regions were fit better with an Einasto profile with $\alpha = 0.16$, which is shallower in the center than NFW. The Einasto profile is defined as:

$$\rho(r) = \rho_s \, e^{-\frac{2}{\alpha}([\frac{r}{r_s}]^\alpha - 1)} \tag{1.7}$$

where the scale parameters are $\rho_s$ and $r_s$, the density and radius at the point

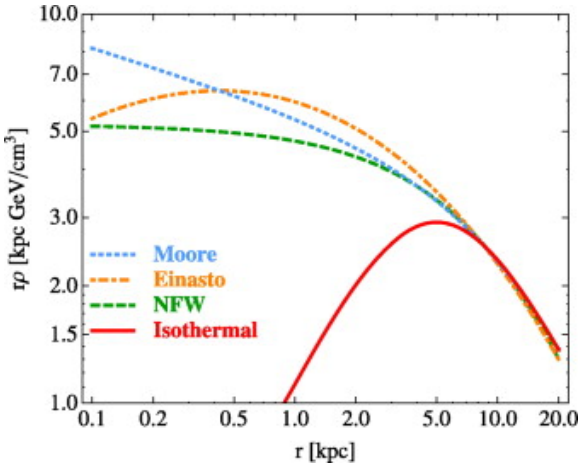


Fig. 1.7: Comparison of density profiles, $r\rho(r)$ vs $r$, for a given density normalization $\rho_0 = 0.3$ GeV/cm$^3$ at 8.5 kpc, the distance from the solar system to the galactic center. From [18]

where the local slope is $-2$. It should be noted that the inner region of halos is dominated by the baryons, but due to computational and theoretical limitations are not separately accounted for in the simulations. More detailed predictions will require a realistic treatment of the baryons.

These simulations give us guidance for where we can look for a DM annihilation signal. At the largest scale, we might expect some signal in the diffuse gamma ray background from the halos of unresolved galaxies, where the challenge is disentangling a DM signal from the gamma ray spectra of galaxies, AGNs, and so on. The galactic halo has a very high density of dark matter but also has a large and complicated background to understand from the galactic disk and bulge. Recent searches have been carried out with Fermi data in both of these [7, 83]. As mentioned above, because of the hierarchical formation of the halo, there is also much substructure in the form of gravitationally bound clumps (DM satellites, also called subhalos) and unbound DM streams. Some of this is visible in the Milky Way dwarf galaxies, which have the highest $M/L$ ratios of any known objects. These have also been the target of Fermi analysis [57]. Much of the substructure however does not host visible

stars, to the best of our ability to detect. The signal from these would show up as gamma ray sources with no associations at other wavelengths. These have the advantage of a lower background compared to the MW center or halo, but of course since they have no stars, we do not yet know specifically where they are, and must scan the sky. In this thesis, we focus on the search for such signals, and we use the data from the Aquarius and VL2 simulations to model Milky Way subhalo abundance and properties. Projected (integrated line-of-sight) density squared maps of Aquarius and VL2 are shown in figure 1.8 and 1.9.

## 1.8 DM galactic subhalos

Simulations predict that the density profile of subhalos is very similar to that of the main halo. Each simulation was able to resolve over 50,000 satellites within the virial radius of its respective main halo, defined by $r_{200}$, the maximum radius which encloses an average density 200 times the cosmological mean matter density. VL2 resolved subhalos down to the size of $10^5$ $M_\odot$, and Aquarius down to $10^{4.5}$ $M_\odot$. Each bound satellite has associated with it a position with respect to the main halo, a velocity, a tidal mass $M_{tidal}$, a maximum circular velocity $V_{max}$, and a radius of maximum circular velocity $R_{V_{max}}$.

Subhalos also contain within them sub-subhalos and so on. Since the gamma ray signal from annihilation depends on the density squared, this substructure would enhance the flux compared to a more homogeneous density. A precise estimate of this boost factor however requires detailed knowledge of the mass spectrum and density profiles over a dozen decades of mass, which is far beyond what can be gleaned from current simulations. The boost factor may be as large as 100 or on the order of 1 [92]. We do not assume any boost

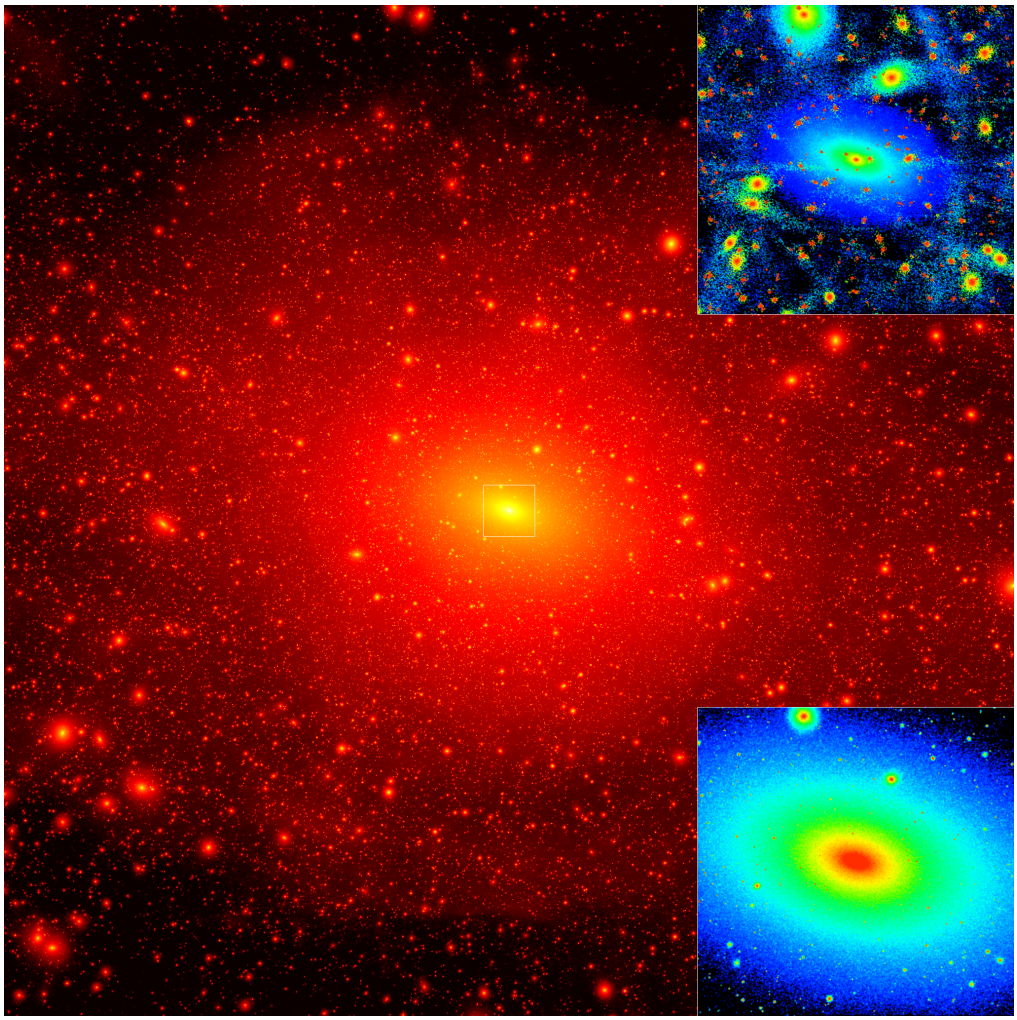

Fig. 1.8: Via Lactea II projected DM density squared map. An 800 kpc cube is shown. The insets focus on an inner 40 kpc cube in local density (bottom) and local phase space density (top). Image brightness is proportional to the log of the squared dark matter density along the line-of-sight. The mass resolution is 4,100 $M_{\odot}$, and the mass within $r_{200}$ (402 kpc) is $1.9 \times 10^{12} M_{\odot}$. From [37]

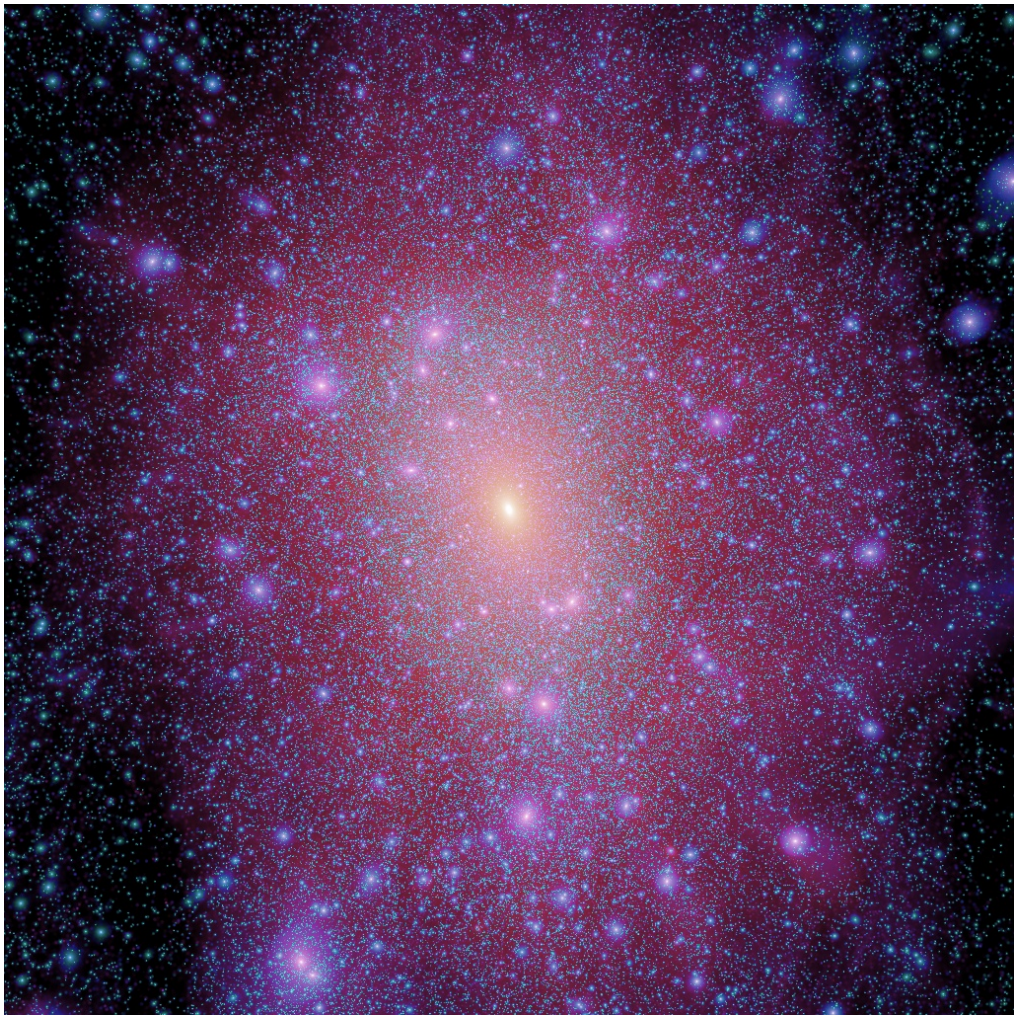

Fig. 1.9: Aquarius projected DM density squared map of an approximately 1 Mpc cube at $z = 0$. Mass resolution is 1,700 $M_\odot$ and mass within $r_{200}$ (245 kpc) is $1.84 \times 10^{12} M_\odot$. From [90]

factor in our predicted annihilation signal flux.

One result from simulations that appears to be at odds with observation is that the predicted number of large satellites of the Milky Way is significantly greater than the known Milky Way satellites (the Large/Small Magellanic Clouds and the dwarf spheroidal galaxies). This has been called the "missing satellites problem" [91]. The Sloan Digital Sky Survey has recently discovered a new population of ultra-faint dwarf satellites [21], and up to a factor of $\sim 5 - 20$ times as many faint galaxies could remain undetected at present owing to incomplete sky coverage, luminosity bias, and surface brightness limits [97], which may alleviate this concern. However even if this is the case, a new problem arises in which the majority of the most massive satellites are too dense to host the known bright Milky Way satellites. [27] calls this the "too big to fail" problem, and suggests possible resolutions: if recent simulations are accurate, it may be the case that galaxy formation is effectively stochastic at this scale, and the ultra-faint galaxies are hosted by the massive subhalos, giving them $M/L$ values of $10^5 - 10^8$. On the other hand, it is possible that the halos studied in the simulations are not very representative of our galaxy, which may be due to mere statistical aberration, or perhaps a need to model baryonic processes, or even different dark matter physics. With this in mind, we press on.

### 1.8.1 Gamma-ray flux from Dark Matter Satellites

The photon flux incident on the LAT for a DM source can be expressed as the product of two factors [44]: a particle physics factor $\Phi_{PP}$ which contains the dependence on the particle model, and the astrophysical $J-$factor that contains the dependence on the DM distribution in the source, i.e., the density profile:

$$\Phi_\gamma = \Phi^{PP} \times J \tag{1.8}$$

Going into the particle physics factor are the mass $m_\chi$ and the thermally averaged cross-section $\langle\sigma v\rangle$. The underlying physics of the particle supplies the relative differential photon yield $dN_f/dE$ for Standard model final state $f$, with $B_f$ its branching ratio:

$$\Phi_{PP} = \frac{\langle\sigma v\rangle}{8\pi m_\chi^2} \int \sum_f \frac{dN_f}{dE} B_f \, dE \tag{1.9}$$

The $J$-factor in the direction $\theta$ (relative to the center of the subhalo) is the line-of-sight ($l$) integral of the square of the density profile $\rho$ within a solid angle $d\Omega$. The total $J-$factor is $J(\theta)$ integrated over the solid angle of observation $\Delta\Omega = 2\pi(1 - \cos\theta)$.

$$J = \int_{\Delta\Omega} d\Omega \int_{l.o.s.} \rho(l)^2 \, dl \tag{1.10}$$

For satellites at large distances $D$ from the Earth, the $J$-factor can be approximated by

$$J \approx \frac{1}{D} \int_V \rho(r)^2 dV \tag{1.11}$$

where the volume integration is performed out to the satellite tidal radius [99].

The differential mass spectrum of subhalos is fit by a power law, $dN/dM_{sub}$ $\sim M_{sub}^{-a}$, where $a$ is found to be very close to $-1.9$ in both VL2 and Aquarius simulations. This steep slope implies there is a significant amount of mass in small subhalos that are unresolved in current simulations, meaning that small nearby subhalos could also be viable sources for gamma ray detection. The previous subhalo analysis performed an extrapolation of this function down to a tidal mass of $1M_\odot$, and estimated that these subhalos would have a minimal effect ($< 5\%$) when setting upper limits on $\langle\sigma v\rangle$ [8], based on calculation of their $J-$factors.

We now have some guidance for a set of criteria we can use to attempt to

distinguish DM satellites from other astrophysical sources. They will have a characteristic spectrum (depending on the DM particle), they will have spatial extension, they should not be variable in intensity, and they should not have any counterparts at other wavelengths. Before detailing the analysis methods used to discern DM satellites quantitatively using these considerations, we describe the Fermi LAT instrument, its data products, and statistical methods.

# Chapter 2

# *Fermi* Large Area Telescope

The Fermi Gamma-Ray Telescope was launched by NASA on June 11, 2008 from Cape Canaveral, and the Large Area Telescope (LAT) is the main gamma ray detection instrument on board. Also contained is the Gamma-ray Burst Monitor (GBM), a detector covering the 8 keV to 40 MeV energy range dedicated to studying gamma ray bursts. The LAT is a pair-conversion telescope which has the capability to detect gamma rays in the range from 20 MeV to over 300 GeV, and cosmic rays up to 3 TeV. Fermi's orbit is at $\sim$565 km and 25.6° inclination, and its field of view covers about 20% of the sky at a time. In normal "scanning" operation, the instrument z-axis is pointed to 50° (increased from 35° at the beginning of operation) North or South of the zenith (the direction away from the Earth) on alternate orbits. Thus the LAT achieves near uniform sky exposure after 2 orbits, covering the full sky in about 3 hours. The LAT does not take data while inside the South Atlantic Anomaly (SAA), a region of the inner Van Allen radiation belt; the fraction of time spent in the SAA is 14.6%. The LAT may also be pointed at interesting targets of opportunity such as pulsars or gamma ray bursts. The LAT has a continuous output data rate of about 1.5 Mbits per second. Data are stored on Fermi and transmitted to the ground about 10

times per day from the satellite through NASA's Tracking and Data Relay Satellite System to ground terminals at the White Sands Complex, and then to the LAT Instrument Science Operations Center (ISOC) at SLAC.

In this chapter, we describe the structure, performance, and data processing pipeline of the LAT. A full technical description can be found in [15], and an updated description of instrument performance based on 3 years of observations in [6].

## 2.1 Structure

The LAT is composed of a $4 \times 4$ array of towers, each of which consists of interleaved tungsten ($Z = 74$) pair-conversion foils and silicon strip particle-tracking detectors, and a cesium iodide calorimeter. The entire assembly is covered by an anticoincidence detector (ACD), whose goal is to reject the charged particle background, and a multi-layer insulation and micrometeoroid shield. A diagram and picture are shown in figure 2.1. As a gamma ray enters the LAT, it pair-converts predominantly in the high-$Z$ foils. These $e^+e^-$ pairs are tracked by the strips, and the energy of the gamma ray is measured by the deposition of the electromagnetic shower into the calorimeter. The on-board software then uses the triggers from the subsystems to build events and reject most of the charged-particle background before the data are transmitted to the ground.

In each tower, there are 18 tracker planes that record the passage of charged particles, and the upper 16 tracker planes are preceded just above by tungsten foils. Each plane has 2 layers ($x$ and $y$) of silicon strip detectors with a pitch of 228 microns, spaced apart by 2 mm gaps. These planes are supported by 19 composite panels, or "trays," each with a thickness of about 3 cm. The first 12 foils (the "front converters") have a depth of 0.035 radiation

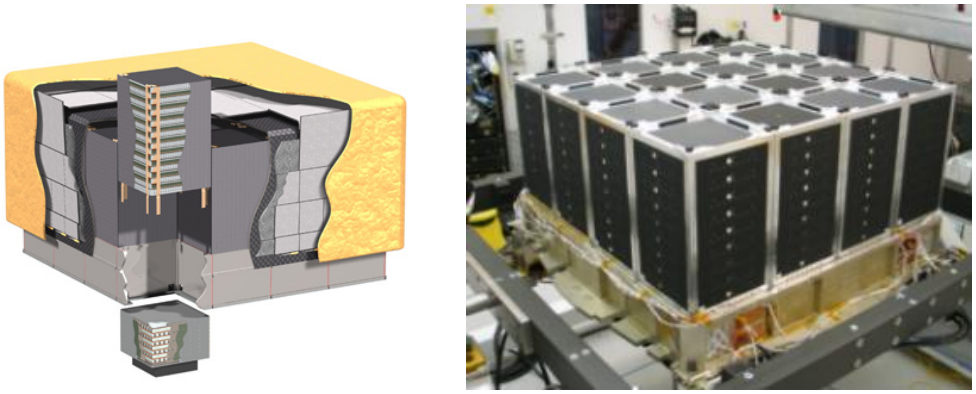

Fig. 2.1: Schematic cutaway view of the LAT showing the micrometeoroid shield, ACD, and towers (left), and a picture of the 16 towers in the grid (right) before the ACD assembly. From [82].

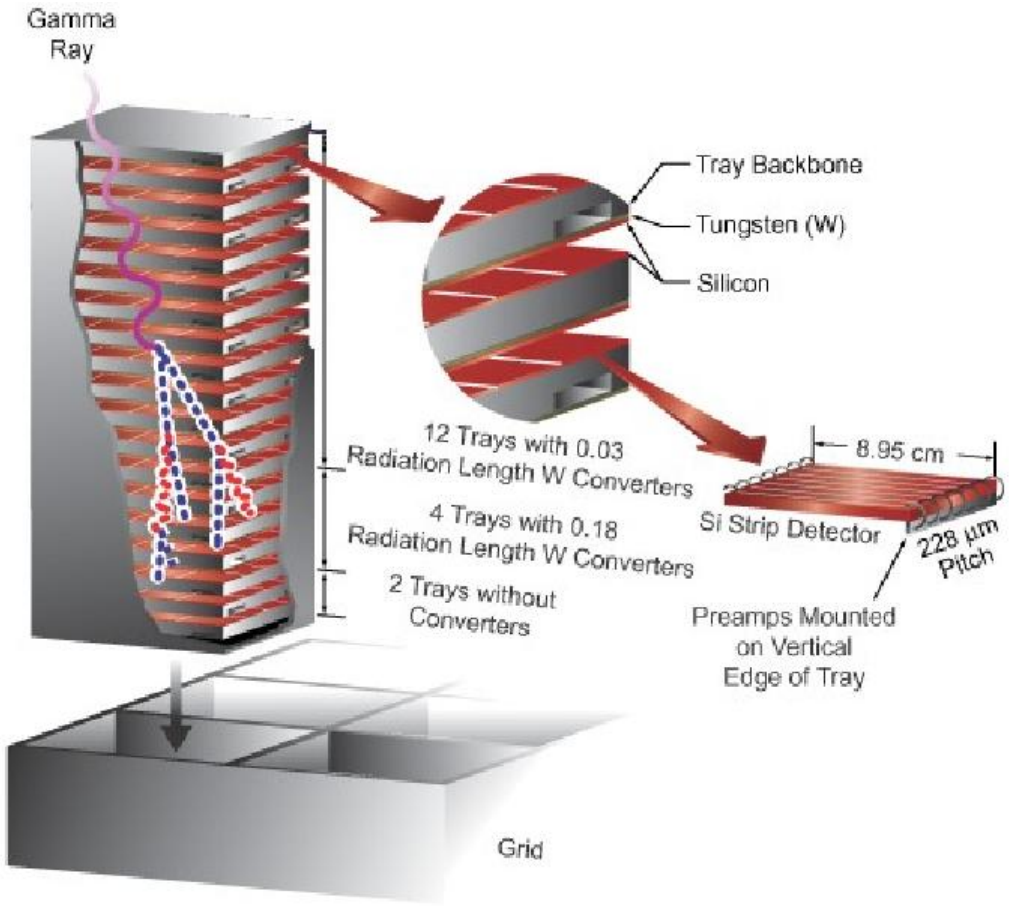


Fig. 2.2: Schematic view of the Large Area Telescope silicon tracker. Each tower includes 19 tray structures constituting the basic mechanical framework and housing both the silicon detection planes and the converter foils. From [82].

lengths, while the next 4 ("back converters") have 0.18. The presence of two different converter thicknesses is intended to find a good balance between angular resolution and effective area—thicker material increases the effective area but also increases multiple scattering, spreading the $e^+e^-$ pairs which makes directional reconstruction less precise. Instrument simulations show that the sensitivity of the LAT to point-sources is approximately balanced between the front and back tracker sections. The bottom two tracker planes have no converter, as a conversion in these planes would never achieve the three tracker plane hits in a row required by the trigger, and so would only add to multiple scattering, degrading the resolution.

The calorimeter module at the bottom of each tower consists of 8 layers of 12 CsI(Tl) crystals with each crystal of size $2.0 \times 2.7 \times 33.6$ cm, and has a depth of 8.6 radiation lengths at normal incidence (total instrument depth including the tracker is 10.1 radiation lengths). Each layer is aligned 90° with respect to its neighbors, forming an $xy$ "hodoscopic" array. As the shower goes through the calorimeter, it ionizes the CsI molecules and induces scintillation in the crystals, measured by photodiodes at each end of the long dimension of the crystals. The segmentation allows imaging of the shower development profile which provides an estimate for the fraction of energy that escapes the calorimeter, contributes to background rejections of protons, and gives a measurement of the centroid of energy deposition which serves as an anchor point in the track reconstruction algorithm.

The anti-coincidence detector (ACD) comprises 89 independent plastic scintillation tiles which surround the top and sides of the LAT, whose function is to distinguish the large charged particle background from gamma rays. The background can outnumber the gamma rays by a factor of up to $10^5$ [61]. The LAT specification is to have any residual background be at the level of no more than 10% of the diffuse gamma ray background. This requires a factor of $10^6$

suppression of protons and $10^4$ of electrons. The proton rejection is done by the ACD along with the tracker and calorimeter. Reconstructed track events are extrapolated backwards to the ACD, and the event is rejected if there is a signal in the closest ACD tile. Electron and gamma ray cascades however look similar in the calorimeter, so only the ACD and tracker are used for this background rejection. The tracker assists by requiring the conversion point of an event be identifiable by the absence of a signal in the layers projected backwards from the path, however this comes at the cost of photon efficiency as some photons will convert in the ACD. The estimated efficiency of the cosmic-ray detection is greater than 0.9997. The segmentation in the ACD also alleviates much of the false veto from the cascade of high-energy photons travelling back up through the tracker and triggering the ACD by Compton scattering, called "backsplash;" only the ACD segment in the projected path of the photon may contribute to the false veto.

The Data Acquisition System (DAQ) is the on-board hardware and software consisting of several modules which collect data from the other subsystems, implement the multi-level event triggers, and provide on-board event processing. The first level of the trigger is hardware; the primary gamma ray trigger is the "three in a row," 3 consecutive tracker planes. There are also adjustable calorimeter triggers based on energy deposition into a crystal. The ACD also has two triggers, a veto signal and a CNO (carbon-nitrogen-oxygen) signal, which is used to identify heavy ($Z > 2$) ions. A module called the GEM then combines the signals it receives in a 600 ns window and decides whether to accept the event and how read out the detector. Typical dead time from processing events is about 26.5 $\mu$s, which compared to a few kHz for the typical frequency of particles hitting the LAT, means that the LAT can trigger on nearly all particles that come across it; trigger dead time fraction is $\sim$9%. The second trigger level is software, the Event Processing

Units which apply filters to events to optimize rejection of charged particle background events and maximize the rate of gamma-triggered events which are downlinked. About 400 Hz of events are sent to the ground, of which a few Hz are gamma events.

Analysis on the ground (described in the following section) is responsible for the final discrimination between background and Earth albedo gamma events from celestial gamma events. After event reconstruction, the event is analyzed to determine the accuracy of the energy, direction, and identification as a gamma ray. The estimates are done using probabilities generated by classification trees, which were built using large sets of Monte Carlo (MC) events from the LAT simulation package. The considerations for rejecting backgrounds involve the topology of the events in the tracker and identification of an electromagnetic shower. Combined with the rejection done by the DAQ, overall the background is reduced by a factor of about $10^6$ while preserving gamma ray detection efficiency in excess of 75%.

## 2.2 Event reconstruction, analysis, and classification

### 2.2.1 Event reconstruction

The raw data from the tracker, calorimeter, and ACD are used to reconstruct the photon physical quantities (energy and direction) according to established event analysis schemes. The pre-launch version of these procedures is called "Pass 6," since replaced by "Pass 7" in August 2011, which was used to produce the second Fermi LAT catalog (2FGL) [68]. Each version has associated with it standard event classes, in which events are categorized according to the quality of the reconstruction for different analysis purposes,

and instrument response functions (IRFs), which are representations of the instrument performance.

An example of an event is shown in Figure 2.3. The starting point for the energy evaluation is the measured energy deposition in the calorimeter crystals. The centroid of the energy deposition is determined, and the principal axes of the shower are calculated by means of a principal moment analysis. Energy deposition in the tracker must also be accounted for, and this is evaluated by treating the tungsten-silicon detector as a sampling calorimeter. Three separate algorithms are used to estimate the energy of an event, and the only major point of difference between Pass 6 and Pass 7 is that the latter applies separate corrections for biases in each algorithm.

The goal of tracker reconstruction is to find the most likely incident direction of the photon. This is accomplished by assembling clusters of adjacent hit strips into track candidates by combinatorial analysis according to two different algorithms: CAL-Seeded Pattern Recognition (CSPR) in which the trajectory is assumed to point at the centroid of energy released in the calorimeter, and the Blind Search Pattern Recognition (BSPR) which can be used when there is little or no energy deposited. Both are weighted to consider the best candidate track to be the one which is both pointing toward the calorimeter centroid and is the longest and straightest. In the CSPR, the main axis of the calorimeter energy deposition is also considered. At the completion of the CSPR algorithm, the best candidate track is selected and confirmed as a track, and the clusters in it are flagged as used. The CSPR algorithm is iterated until no further tracks can be assembled from the unused tracker clusters, then proceed with the BSPR. If more than one track is found for a given event, a vertexing algorithm is applied that attempts to compute the most likely common origination point of the two highest quality (i.e., longest and straightest) tracks, and to use that point as a constraint

in combining the momenta of the tracks to obtain a better estimate of the direction of the incoming gamma ray.

In the ACD phase, these tracks are projected back to the ACD to check whether this track intersects a tile or ribbon with non-zero energy deposition. If the ACD element has no energy deposition, the distance to the nearest tile with non-zero energy deposition is calculated. This information is then used to consider whether the event should be rejected as charged particle background in later analysis.

### 2.2.2 Event analysis

After event reconstruction is the event-level analysis procedure, in which simpler representations of the event characteristics are extracted from the complex structures assembled during the reconstruction phase, which are used for the final assignment of the event energy and direction, and for background rejection. The final product is an event-by-event array of simple quantities relevant for scientific analysis: energy, direction and estimates of the probability that a given event is a gamma ray.

For each event, the output of the tracker, calorimeter, and ACD reconstruction is digested into a set of a few hundred figure-of-merit quantities, whose analyzing power has been studied and optimized with MC simulations. Then, the best likely estimate of energy is selected from the three reconsstruction algorithms using a classification tree analysis, and the event is assigned a quantity estimating the quality of the reconstruction $P_E$. Similarly for the event direction, a CT analysis is used to select the measured direction from the available options: the best track, the best vertex, and these two options again but using the calorimeter centroid of energy deposition as an additional constraint. An additional CT analysis is used to estimate the quality of reconstruction, $P_{core}$, the probability that the direction falls within the nominal

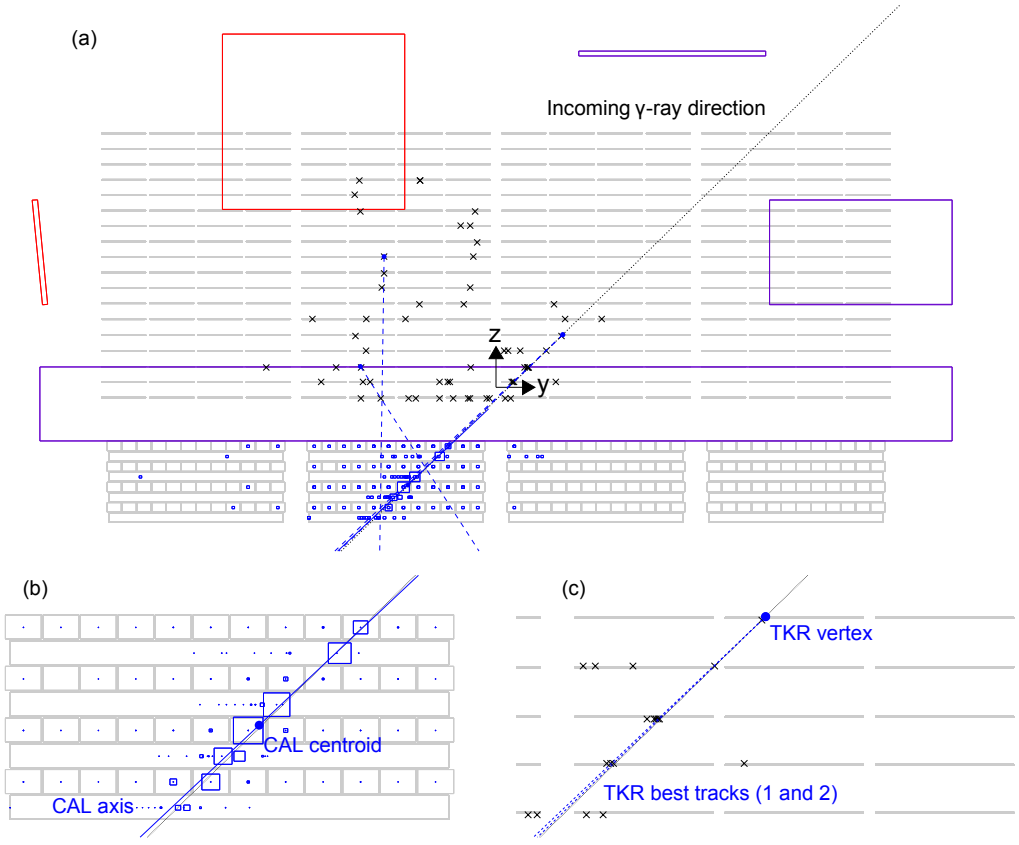


Fig. 2.3: Event display of a simulated 27 GeV gamma ray (a) and zoom over the calorimeter (b) and tracker (c) portions of the event. The small crosses represent the clusters in the tracker, while the variable-size squares indicate the reconstructed location and magnitude of the energy deposition for every hit crystal in the calorimeter. The dotted line represents the true gamma ray direction, the solid line is the calorimeter axis, and the dashed lines are the reconstructed tracker tracks. The backsplash from the calorimeter generates tens of hits in the tracker, with two spurious tracks reconstructed in addition to the two associated with the gamma ray (note that they extrapolate away from the calorimeter centroid and do not match the calorimeter direction). It also generates a few hits in the ACD, which, however, are away from the vertex direction extrapolation and therefore do not compromise the ability to correctly classify the event as a gamma ray. From [6].

68% containment core as defined by a simplified analytical model of the PSF.

Background rejection first proceeds by identifying events for which evidence clearly indicates that a charged particle entered the LAT from inside the field of view. This stage is referred to as Charged Particle in the Field-of-view (CPF) analysis. Here, a series of filters are applied which classify as background any events for which the best track has hits all the way to the edge of the tracker, and either points to an ACD element which has significant deposited energy or points directly to the less sensitive ACD areas, such as corners or gaps between the tiles. Next, the procedure attempts to account for events where the best reconstructed track does not represent the incoming particle well. This can happen for a variety of reasons, such as a calorimeter backsplash particle being assigned the best track, or when the particle passes largely in the gaps between the tracker towers. Events for which the total energy deposited in the ACD is too large to be accounted for by calorimeter backsplash are classified as background. At this point, all events classified as charged particles are removed from further consideration and are passed to separate analyses to identify various species of charged particles. Another CT analysis is performed, combining all the available information into an estimate of the probability that the event is from charged particle backgrounds, $P_{CPF}$. The performance of this stage depends on energy and incident angle, but roughly more than 95% of background is removed by these cuts, as is about 10% of the gamma ray sample.

The remaining stages of the event analysis are based on topology of energy deposition in the tracker and calorimeter. Since eletrons and positrons cause electromagnetic showers that look extremely similar to gamma ray interations, these will not have much additional discriminating power against such backgrounds, and serve primarily to identify hadronic charged particle background events. Such events are not immediately removed, but only flagged to allow

for removal from higher purity event classes. In the tracker, the events that are flagged are those with energy deposition in the tracker planes expected for heavy ionizing particles as well as events with very high energy deposition in the first hit layers of the tracker, which is a signature of a particle coming through the calorimeter that ranges out in the middle of the tracker. In the calorimeter, general cuts are made which flag events coming from the side and bottom of the LAT. From then on, analysis of the tracker and calorimeter topology are similar to one another. In each, events are divided among 5 branches depending on their topology, and in each branch a cut and a CT analysis is run, which provide estimates of the probability that the event is a gamma ray, $P_{TKR}$ and $P_{CAL}$. After these analyses, a final CT analysis is run using all available information, including the outputs of CT analyses from previous phases.

### 2.2.3 Event classes

At this point, the event analysis has produced a number of specifiers of event reconstruction and classification quality on an event-by-event basis: the energy and direction reconstruction qualities $P_E$ and $P_{core}$, the gamma ray probabilities from the CPF, tracker, and calorimeter analysies, and the overall probability from the final step, $P_{CPF}$, $P_{TKR}$, $P_{CAL}$, and $P_{all}$ respectively. These quantities are used to define event classes, optimized for different ranges of astrophysical source analyses. These classes are nested: each succeeding selection is a strict subset of the previous ones.

For the standard event classes, a few fiducial cuts are made to include only events that have some chance to be useful for most analyses, namely events for which an energy and direction can be reconstructed. The event must have a reconstructed track to allow for a direction estimation, and this track must point to the calorimeter, cross at least 4 radiation lengths of calorimeter ma-

terial, and deposit at least 5 MeV of energy in it. This removes events that deposit all their energy in the tracker or miss the calorimeter, and events that do not have reconstructed tracks but have enough information in the calorimeter to derive an estimate of the even direction. The classes are described below, with a more detailed description in [6].

The Pass 7 classes have improved performance and/or lower background contamination relative to Pass 6. Generally, the selections were tuned to give roughly the same background contamination rates, while gaining in effective area. The Pass 7 event selections are based only on quantities that have been shown to be well modeled in the Monte Carlo simulations. Therefore the associated IRFs do not require any flight based correction of the type that was applied in making the P6_V11_DIFFUSE IRFs. The relative selection efficiencies for the event classes (described in the following paragraphs) as well as previous stages of the event selection process are shown in Figure 2.4, and estimates of the rates of residual particle backgrounds for the three higher-purity classes is shown in Figure 2.5. The intended use and summary of cuts in the Pass 7 classes are itemized below. Brief descriptions of these classes and rough correspondence to the Pass 6 classes are given in table 2.1.

- The Transient class has the lowest purity, and is used primarily in analysis of brief transient sources (e.g., GRBs) for which high purity is not required. The cuts have the aim of achieving a residual background rate of a few Hz while maintaining a large efficiency for gamma rays. As a point of comparison, a background rate of 2 Hz results in one background event every 5 sec inside a 10 radius about a source. The cuts are few and loose: there are minimal cuts on the quality estimators, on energy and calorimeter deposition, and on $P_{CDF}$ and $P_{all}$.

- The Source class is intended for the analysis of point sources, and so re-

quires a lower background rate to minimize impact on source detection and characterization, as well as consideration for systematic uncertainties below 1 GeV. The cuts for this class and the higher-purity classes were developed and optimized using on-orbit data samples as well as MC simulations. The cuts include events flagged during tracker and calorimeter topological analysis and tighter requirements on $P_E$, $P_{core}$, and $P_{all}$.

- The Clean class is intended for analysis of diffuse gamma ray emission. The background contamination is reduced to ∼0.1 Hz, compared to the total Galactic diffuse contribution of ∼1 Hz. The selection includes cuts designed to reject specific backgrounds such as cosmic rays coming through gaps in the ACD, and cuts on calorimeter topology designed to remove hadronic cosmic rays.

- The Ultraclean class reduces background contamination further still for analysis of the extragalactic diffuse gamma ray emission. It achieves ∼40% lower contamination than the Clean class, and consists only of a tighter, energy-dependent cut on $P_{all}$.

One other important point is that the excellent stability of the LAT subsystems means that changes in performance over time are not a consideration in defining the event analyses or IRFs; the small changes in performance at the subsystem level are easily addressed by calibrations applied during the event reconstruction procedure. This allows IRFs to be produced that are valid for the entire mission time, simplifying the data analysis task by removing the need to split the LAT data by time range.

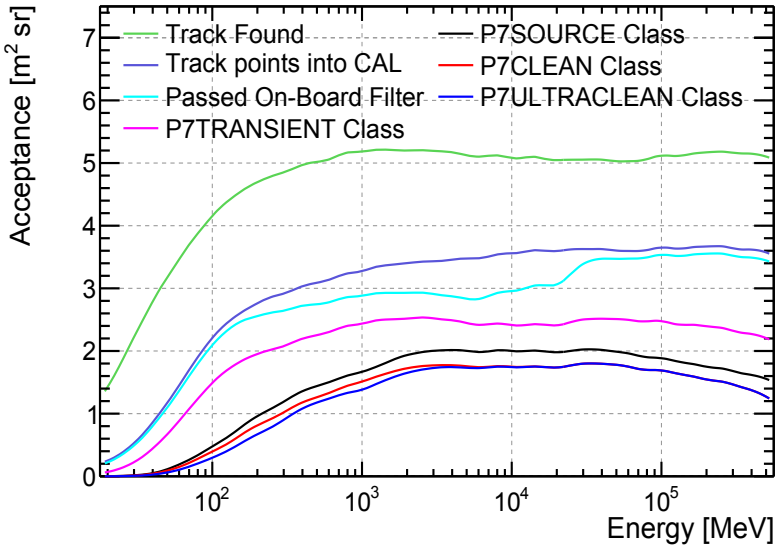


Fig. 2.4: LAT $A_{eff}$ integrated over the FoV as a function of energy at successive stages of the event filtering as estimated with simulated data. Since we require a direction and energy to use a gamma ray for science analysis we consider only events with at least one track found and that pass the fiducial cuts. From [6].

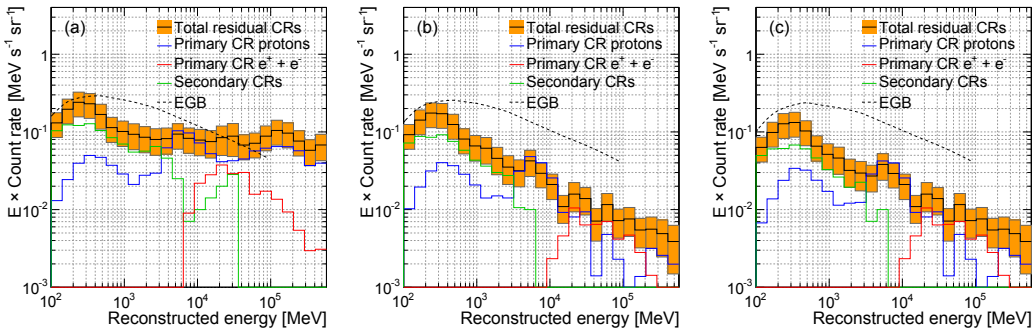


Fig. 2.5: Best estimates of differential rates of residual particle backgrounds for the Source (a), Clean (b), and Ultraclean (c) event classes. Individual contributions from primary CR protons, primary CR electrons, and secondaries from CR interactions are shown. The corresponding count rates for the extragalactic gamma ray background measured by Fermi in [4] are also overlaid for comparison. From [6].

Table 2.1: LAT event classes

| P7 Analysis class (P6 Equivalent) | Residual background rate (Hz) | Description |
|---|---|---|
| Ultraclean (None) | $< 0.1$ | Highest quality and lowest background selection. Overconservative, entails a significant loss of effective area. Mainly to use as a cross check that observed features are not due to cosmic-ray contamination. |
| Clean (DataClean) | 0.1 | Very high quality and low background selection. Recommended for analyses that integrate large regions of the sky. Reduces non-photon spectral features to very low levels. |
| Source (Diffuse) | $< 1$ | High quality selection, residual rate comparable to irreducible limit, and tails of PSF at high-energy minimized. Recommended for most analyses. |
| Transient (Transient) | 2 | Lower quality selection, maximizes effective area at expense of high residual background rate. Used for transient or timing analysis. |

## 2.3 IRFs

The Instrument Response Functions (IRFs) are parameterized representations of the instrument performance, and describe the probability of obtaining the reconstructed physical quantities given the true quantities, which is determined by the effects of the detector and the algorithms used to reconstruct photon events from tracker and calorimeter data. The initial Pass 7 IRFs are the "P7CLASS_V6" set, derived from flight data. Most generally, we can write the probability in the form:

$$R(E', \Omega' | E, \Omega) \tag{2.1}$$

where we have assumed time-independence, $E$ and $\Omega$ are the energy and direction of the photon, and the primed and unprimed quantities are the measured and true quantities. This can be factored into two components, the point-spread function (PSF) which describes likelihood to reconstruct a

gamma ray with a given angular deviation $\delta v = |\hat{v}' - \hat{v}|$, and the energy dispersion ($\Delta E$). This can be rewritten as:

$$R(E', \Omega'|E, \Omega) = PSF(\Omega'|E, \Omega) \times \Delta E(E'|E, \Omega) \tag{2.2}$$

Additionally in the IRFs there is the effective area $A_{eff}$, the parameter that determines the rate of detecting signal photons given an incident flux $F$, which is a function of the geometrical area and the conversion probability—including the efficiency of the reconstruction algorithms—at different incidence angles and energies. So overall, the differential photon flux we expect from a source of flux $F(E, \Omega)$ is written:

$$\frac{dN_s}{dt}(E', \Omega') = \int_E \int_\Omega A_{eff}(E, \Omega) \cdot \Delta E(E'|E, \Omega) \cdot PSF(\Omega'|E, \Omega) \cdot F(E, \Omega)\ dE d\Omega \tag{2.3}$$

The parameterization of the PSF used in the Pass 6 IRFs was built based on MC simulations, and have been updated using on-orbit data for Pass 7. The energy dependence of the PSF is factored into a scaling term:

$$S_P(E) = \sqrt{\left[c_0 \cdot \left(\frac{E}{100\,\mathrm{MeV}}\right)^{-\beta}\right]^2 + c_1^2} \tag{2.4}$$

where $\beta, c_0$, and $c_1$ are parameters with fixed values for each conversion type (front vs back). From this, the scaled angular deviation, $\theta$, is defined as:

$$\theta = \frac{\delta v}{S_P(E)} \tag{2.5}$$

The effect of the scaling is to make the profile almost independent of energy, in that the maximum is always close to $x = 1$ for all energy bins while the PSF 68% containment varies by almost two orders of magnitude from 100 MeV to 100 GeV. The base function used to model the PSF is referred to as a *King*

*function* [52]:

$$K(x,\sigma,\gamma) = \frac{1}{2\pi\sigma^2}\left(1-\frac{1}{\gamma}\right)\cdot\left[1+\frac{1}{2\gamma}\cdot\frac{\theta^2}{\sigma^2}\right]^{-\gamma} \tag{2.6}$$

where $\sigma$ and $\gamma$ are parameters to be fit. In practice, their values for different energy bins and incidence angles are stored in tables. In the limit of large $\gamma$, the King function basically becomes a Gaussian, so $\gamma$ can be seen as a parameter that characterized deviation from the "ideal" Gaussian, and $\sigma$ sets the overall angular scale. The PSF model has been fit to the measured 68% and 95% containment radii using a procedure which fits the width of bright point sources using flight data, described in detail in [9]. Although the PSF does have some dependence on incidence angle (on the order of 10%), given statistical limitations this is not measured, and instead an acceptance-weighted average over incidence angle is calculated. Azimuthal dependence is in almost all cases weaker than this dependence. The containment radii for the P7SOURCE_V6 PSF are shown in Figure 2.6.

The energy dispersion is generally asymmetric, with the most prominent tail being toward lower energies. This makes the energy redistribution difficult to parameterize. Since most source spectra are steeply falling with energy, the low-energy tails in the dispersion are relatively harmless. By default the energy dispersion is not taken into account in the standard likelihood analysis (this is maintained all throughout our analysis here as well) due to computational limitations. However, the effect of the finite energy resolution is generally negligible compared with other sources of systematics (see §7.4 in [6]). Energy dispersion performance is shown in Figure 2.7.

The effective area $A_{eff}$ depends on the geometrical cross-section of the LAT as well as the efficiency for converting and correctly identifying incident gamma rays. Because of the complexity of determining these, $A_{eff}$ is evalu-

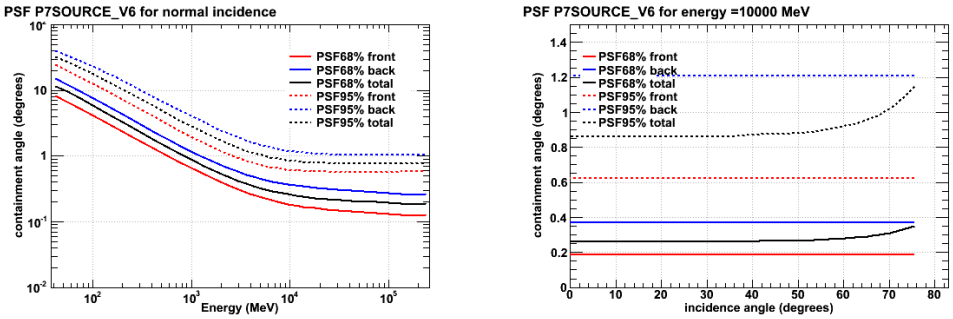


Fig. 2.6: 68% (solid) and 95% (dash) PSF containment for normal-incidence photons as a function of incident energy (left), and for 10 GeV photons as a function of incident angle (right) for P7SOURCE_V6 IRFs. From [106].

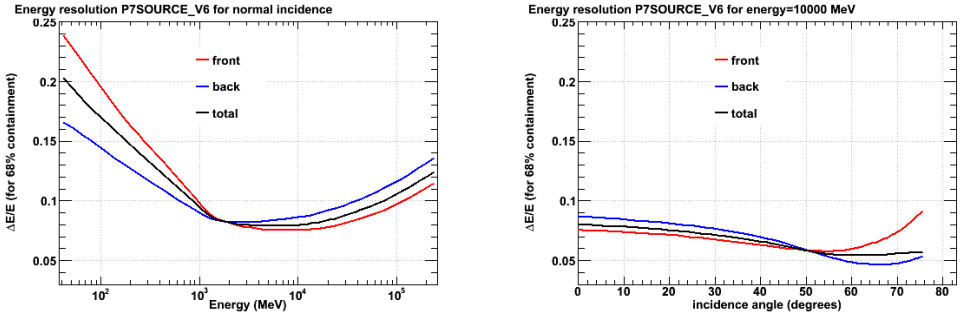


Fig. 2.7: 68% energy containment for normal-incidence photons as a function of incident energy (left), and for 10 GeV photons as a function of incident angle (right) for P7SOURCE_V6 IRFs. From [106].

ated using high statistics MC simulations and corrected based on flight data. These simulations generate tables of $A_{eff}$ as a function of energy and incidence angle, for both the front and back converters. Second-order effects from azimuthal- and livetime-dependence are also accounted for. The effective area is plotted in Figure 2.8.

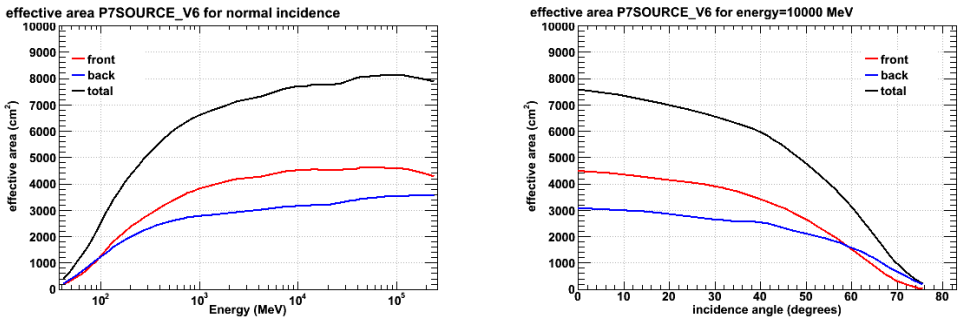


Fig. 2.8: Effective area for normal-incidence photons as a function of incident energy (left), and for 10 GeV photons as a function of incident angle (right) for P7SOURCE_V6 IRFs. From [106].

# Chapter 3

# Analysis

In this chapter we introduce the analysis methods for the DM satellite search. We describe the data set from the LAT and our initial set of candidate sources, define the spatial extension and spectral tests and the criteria used to identify a potential dark matter satellite.

## 3.1 Likelihood methods for LAT data

The angular resolution in gamma ray telescopes limits how well we can resolve astrophysical background from the sources. In Figure 2.6, we can see that the scale of the point-spread function (PSF), characterized by the 68% containment, is about 5° at 100 MeV, and still 1° at 1 GeV, making source confusion a very palpable problem. Additionally, the orientation of the LAT with respect to the source is constantly changing, which also changes the instrument response—the number of photons received cannot be converted directly into a flux, even if we had perfect angular resolution. These considerations motivate likelihood techniques for LAT data analysis, which incorporate the energy and angle dependence of the IRFs and work in terms of instrumental (instead of physical) quantities. Here we define the likelihood functional

form, and describe the *pointlike* software package which does the maximum likelihood analysis of LAT data.

### 3.1.1 Likelihood analysis

Simply put, the primary goal of our analysis of LAT sources is to compare how well different models fit the data. We quantify this with the likelihood $L$, which is the probability of obtaining the data given some input model with adjustable parameters. We fit the model to the data by varying these parameters until $L$ is maximized. More formally, we characterize a source with a *probability density function* (pdf). For our purposes, this is the flux density, $F(E, \Omega)$, the rate of photons per unit energy/area/time from a solid angle $d\Omega$ around the sky position $\Omega$.

The spectral model of a source is characterized by a vector of model parameters $\overrightarrow{\lambda}$ (e.g., spectral index and normalization for a power law source), and we can write the measured physical parameters (energy and direction) as a vector $\overrightarrow{x}$, so the pdf of the input model is expressed as $F(\overrightarrow{x}; \overrightarrow{\lambda})$. That is to say, given the model parameters $\overrightarrow{\lambda}$, the probability of obtaining data near the value $\overrightarrow{x}$ is $F(\overrightarrow{x}; \overrightarrow{\lambda})\overrightarrow{dx}$. We can also consider this same expression to be a function of $\overrightarrow{\lambda}$, that is, having measured $\overrightarrow{x}$, we can find the model parameter values most likely to have yielded the measured values. When viewed this way, the quantity is called the *likelihood*, $L$. Also note that using Bayes' Theorem, the likelihood can be converted into the posterior probability, which allows the construction of confidence intervals, the probability that the true value lies within some interval around the estimate.

We will almost always be dealing with a very large number of photons ($10^3 - 10^4$), which makes an unbinned likelihood analysis computationally very expensive, so often the data will be binned in energy and position in the sky. There is a tradeoff between accuracy and computation time however, as

binning destroys some amount of information about the photon. Detecting a photon in one of these bins is a Poisson process, so the probability $p_j$ of detecting $n_j$ events in the $j$th bin where the model predicts $m_j$ is:

$$p_j = m_j^{n_j} \frac{e^{-m_j}}{n_j!} \tag{3.1}$$

And the likelihood $L$ is then the probability of observing the detected counts in each bin, i.e. the product of the probabilities for all bins. Noticing that the product of $e^{-m_j}$ over all $j$ is just $e^{-N_{pred}}$ where $N_{pred}$ is the total number of predicted counts in all bins, the likelihood is written:

$$L = e^{-N_{pred}} \prod_j \frac{m_j^{n_j}}{n_j!} \tag{3.2}$$

Implicit is the assumption that we can accurately predict $m_i$, i.e., that we know what the model looks like to the detector, which is described by the IRFs.

The likelihood is generally a very small number for large data sets (we will typically have on the order of 10,000 bins, and the probability $p_j$ in each of these bins will often be much less than 1). Because the logarithm is a monotonic function, the logarithm of a function achieves its maximum value at the same points as the function itself, so we instead work in terms of the natural logarithm of the likelihood, the "log likelihood," which is easier to compute.

To understand the significance of the fit model, it must be compared to the null hypothesis. We will specify the results of our hypothesis testing using the Test Statistic, which is defined as:

$$TS = -2 \ \ln(L_0/L_1) \tag{3.3}$$

where $L_0$ is the maximum likelihood for the null hypothesis, which is a model with only background and no additional source, and $L_1$ is that for a model with the source at the specified location (alternative hypothesis). Thus the TS is related to the probability that the excess photons at the putative source location can be explained as a background fluctuation.

### 3.1.2 Pointlike

*Pointlike* [51] is an analysis tool which performs a maximum likelihood analysis, maximizing the Poisson likelihood of finding the observed counts, given floating parameters of the spatial and spectral model of the source and the background. At the highest level, it is a collection of Python modules. *Pointlike* bins data using HEALPix [46], a tesselation of the sky by equal-area pixels. The base tesselation comprises 12 pixels, which can be subdivided into a finer tesselation. *Pointlike* bins first into logarithmic energy, and then bins spatially in each energy band such that the binning is much smaller than the PSF in that band.

To compare a model to observation, *pointlike* begins with the characterization of a model with its flux density (i.e., its pdf), and folds the intrinsic source rates through the instrument response function by doing the integration in Eq. 2.3. Although not explicitly expressed there, there is some time-dependence even for steady sources, so an integral over time is also performed. Livetime spent at different pointing angles introduces time-dependence into the PSF, and trigger deadtime and the reconstruction effectiveness due to changing charged-particle background are represented in an seperate efficiency factor. Pointlike performs the time integration by discretizing over the 30-s time intervals in the spacecraft position and orientation file (FT2 file, see section 3.2.4), and over 40 bins in $cos\theta$ to integrate out the time-dependence introduced in the PSF. The result is the calculation of the "exposure-weighted PSF," which

is independent of the source and can be pre-computed.

The energy integral is broken into smaller integrals over many energy bands, and evaluated with a composite Simpson's rule quadtrature over logarithmic energy. For point sources, the PSF is pulled out of the energy integral using the Mean Value Theorem by evalutating it at some energy in each interval, which in practice is within a few percent of the geometric mean of the energy band. This is not done with extended or diffuse sources, since the spatial morphology of such sources can change with energy.

The spatial integral requires integrating the expected rate per unit solid angle over the entire ROI and over each data pixel. In the latter, *pointlike* makes use of the fine binning and uses a central value approximation. The integral over the ROI can be reduced to an integral linear in the King function. For diffuse sources, the convolution of the source extension with the PSF also must be done. The source extension may be specified with an analytic function, or can be represented as a mapcube (as with the Galactic diffuse model) in which case *pointlike* will construct a continuous function by interpolating it. The convolution is evaluated by sampling this function and the exposure-weighted PSF on a regular grid, and performing a 2D Fast Fourier Transform on each, eventually resulting in a pixelated image plane containing the convolved diffuse model. The source flux rate can then be easily computed.

For a source with an NFW density profile, the actual shape of the extension as seen by Fermi requires doing the line-of-sight density-squared integral (equation 1.11) with the NFW profile in for $\rho$ in order to get the $J$-factor. This integral is difficult to solve analytically, and so is represented numerically in a look-up interpolation table which evaluates $J$ as a function of source extension $\alpha$ and offset angle $\theta$ from the center of the source. Respectively, these are represented in the table with 100 entries log-spaced from $0.01^\circ$ and $15^\circ$, and 300 entries log-spaced from $1 \times 10^{-4}$ degrees to $25^\circ$.

The default fitter for *pointlike* is the BFGS [66] algorithm in scipy via *fmin_bfgs*. It uses an analytic calculation of the gradient of the likelihood function $dL(\lambda)/d\lambda_i$ to find its maximum and determine its curvature. It may also use the downhill simplex algorithm (in *scipy* via *fmin*), which makes use of the log likelihood only, if it is too difficult to implement for a spectral model. The errors are estimated from the inverse of the Hessian matrix of $L$.

### 3.1.3 Chernoff's and Wilks' Theorems

Wilks' theorem [101] is a result about the asymptotic distribution of the Test Statistic (eqn. 3.3) of nested hypotheses. Two hypotheses $H$ and $H'$, characterized by their respective sets of possibilities which satisfy them, $S$ and $S'$, are nested if $S \subset S'$. If the null and alternative hypotheses are nested, then as the number of null hypothesis trials approaches infinity, the TS distribution will behave as $\chi^2_k$, where $k$ is the number of extra dimensions in the alternative hypotheses. More precisely, if the hypothesis that a parameter vector $\theta$ lies on an $r$-dimensional plane of $k$-dimensional space is true, the TS distribution is asymptotically that of $\chi^2_{k-r}$. This allows one to calculate the significance of a given TS directly from the $\chi^2$-distribution, as opposed to doing a large set of trials to determine it empirically.

A variation on this theme is Chernoff's Theorem [34], which applies when the null hypothesis $\theta$ lies on the surface of a $(k-1)$-hyperplane, and we test whether $\theta$ is on one side of the hyperplane in a $k$-dimensional space. In this case if the null hypothesis is true, the asymptotic TS distribution is that of a variable which is zero half the time, and $\chi^2_1$ the other half of the time:

$$P(TS) = \frac{1}{2}(\chi^2_1(TS) + \delta(TS)) \tag{3.4}$$

As the spatial extension of a source can only have a zero or positive value,

testing the null hypothesis is the case where the extension is zero and we test if it is positive, which is the case described by Chernoff's theorem: the null hypothesis lies on the surface of the hyperplane which is the edge of parameter space, and in the alternative hypothesis we test if it is above it. The factor of one-half comes from the fact that half the time, the photon distribution will be smaller than the PSF, which results in a $TS_{ext}$ of zero. An additional requirement of Wilks' and Chernoff's theorems is that we must be able to marginalize over the nuisance parameters, i.e., that we can correctly model everything else that contributes to the photon count but which we aren't immediately interested in. In our case, these would be the emissions of the galactic and extragalactic backround and of nearby sources.

One of the goals of the LAT extended source search [56] was to evaluate the false detection probability for measuring source extension. This was done by simulating a large number of point sources over a background and fitting them for extension with *pointlike*, and the resulting distribution was compared to the distribution predicted by Chernoff's theorem. For four different power-law spectra, ∼90,000 sources were simulated. These were placed randomly in the sky on top of simulated Galactic and isotropic diffuse emission as used in the 2FGL catalog, and their fluxes were selected such that their source significance TS∼50, by maintaining an approximately constant signal-to-noise ratio as the Galactic diffuse emission varies. It was found that the distribution agreed broadly with Chernoff's theorem, and to the extent that there was a discrepancy, the simulations tended to produce smaller than expected TS values, which would make the formal significance conservative. A plot of the distribution is seen in Figure 3.1.

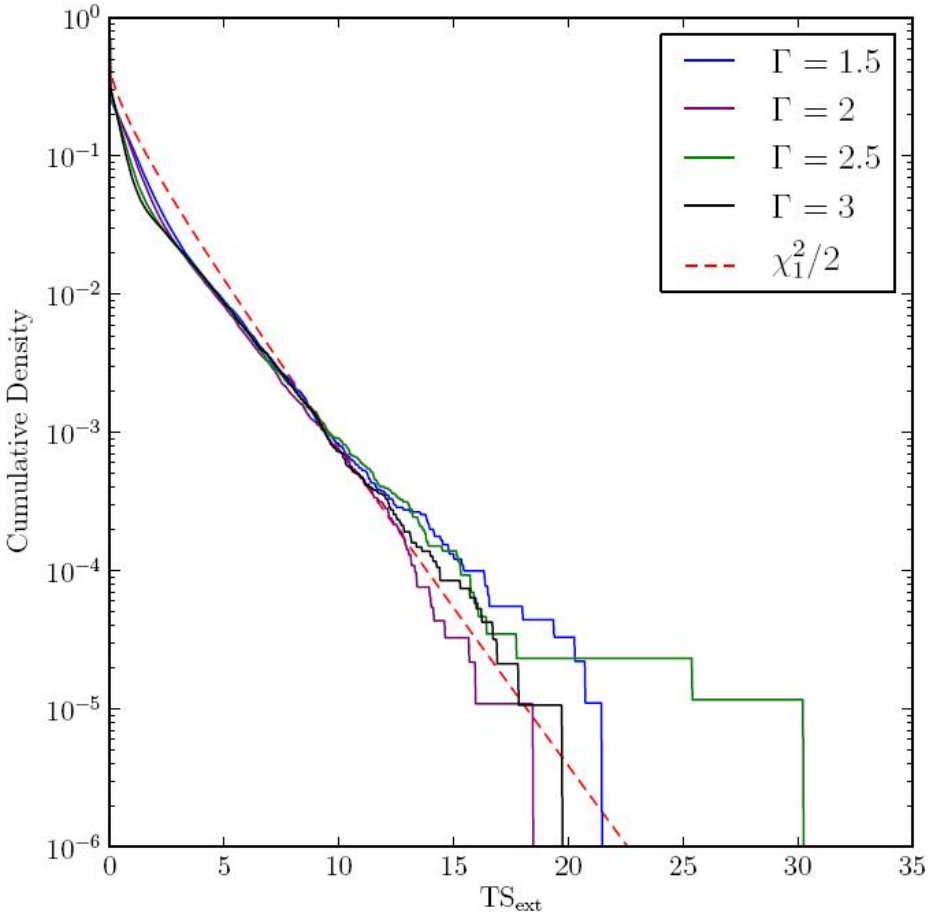


Fig. 3.1: Cumulative distribution of $TS_{ext}$ for point sources simulated on top of Galatic diffuse and isotropic background, compared to the $\chi^2_1$ prediction of Chernoff's theorem. Sources of four different power-law spectra were simulated in the range 1 to 100 GeV, with fluxes selected such that the TS of source detection $\sim 50$. The sources have random positions on the sky within 5° of the galactic plane. From [56]

## 3.2 LAT source analysis principles

### 3.2.1 Region of Interest (ROI)

The extension of the LAT PSF requires us to model the diffuse galactic and extragalactic background as well as other sources near the source we wish to analyze, as the tails of the photon distributions of sources may overlap. In a *pointlike* analysis, we define a region of interest (ROI) around the source we wish to fit, in which we also model any external sources. Such sources are modeled as point sources with power-law or exponential-cutoff spectra according to the best fit model in the catalog. Additionally, there is a list of known extended sources (e.g. the Small and Large Magellanic Clouds) which have defined spatial extension templates. The total (front + back) 68%/98% containment angle at 1 GeV is about 0.9/3 degrees, so for sources less than 5 degrees from the source to be fit, we also allow their fit parameters to float. For sources outside this range, the parameters are fixed to the values in the catalog. The ROIs used in our analyses are 14 degree squares divided into 0.1° squares, and 8 logarithmically-spaced bins per energy decade, giving 20 energy bins.

### 3.2.2 Background modeling

Most of the photon background will come from the galactic and extragalactic diffuse emission, so the ability to correctly fit the spectrum and extension of sources depends greatly on accurate models of these backgrounds. The model for the galactic diffuse emission was developed using spectral line surveys of HI and CO (as a tracer of $H_2$) to derive the distribution of interstellar gas in galactocentric rings. Infrared tracers of dust column density were used to correct column densities in directions where the optical depth of HI was either over or under-estimated. The model of the diffuse gamma ray emission was

then constructed by fitting the gamma ray emissivities of the rings in several energy bands to the LAT observations. The fitting also required a model of the inverse Compton emission calculated using GALPROP (a numerical code for calculating cosmic-ray transport and the diffuse emission they produce) [62] and a model for the isotropic diffuse emission. The isotropic spectral template provides the spectral form from a fit to the all-sky emission ($|b| > 30°$) that is not represented in the Galactic diffuse model and therefore includes both extragalactic diffuse gamma rays and remaining residual (misclassified) cosmic-ray emission.

The software form of the galactic diffuse model is a mapcube, which is a set of spatial templates for a range of energy bins providing the differential flux, with a pixel size of 0.125° and 30 energy planes from 50 MeV to 600 GeV. The isotropic model consists of two columns, a list of energy bands and the differential flux in the band (in ph/cm$^2$/s/MeV/sr). All simulations and analyses in this thesis are done using galactic diffuse and extragalactic (isotropic) models *gal_2yearp7v6_v0.fits* and *iso_p7v6source.txt* respectively, found at [108].

### 3.2.3 LAT livetime and exposure

The LAT will not spend precisely the same amount of time looking at each region of the sky, and the LAT instrument response function (IRF) changes with how far off-angle a photon is from the instrument z-axis. Therefore to properly model the expected photon flux of a source, it is necessary to take into account how much time the LAT spends observing a given position on the sky at various inclination angles over the course of the observation. This quantity is called the livetime and depends only on the history of the LAT's orientation during the observation and not on the source model. The array of these livetimes at all points on the sky is called the "livetime cube."

Livetime cubes are generated by the ScienceTools utility *gtltcube*. However, as a practical matter, the livetime cannot be provided as a continuous function of inclination angle or position on the sky. Thus the livetime cubes are defined on a pixel grid on the sky and in inclination angle bins prescribed by HEALPix [46].

The livetime cube is then used to calculate the exposure cube, an array of exposure maps in each energy bin. The exposure consists of an integral of the total instrument response over time (as provided by the livetime), and over the entire ROI dataspace (area and energy):

$$\epsilon(E,\Omega) = \int_{ROI} dE' d\Omega' dt \; R(E',\Omega'|E,\Omega,t) \tag{3.5}$$

where $R$ is the response function as defined in equation 2.2, provided by the LAT IRFs. The exposure map is then the total exposure (area multiplied by time) for all positions on the sky producing counts in the ROI. The counts produced by a source at a given position on the sky is the integral of the source photon intensity and the exposure at that position. The exposure map is used for extended sources and the diffuse Galactic and Extragalactic backgrounds, and not for point sources. *Pointlike* generates these exposure cubes on the fly.

### 3.2.4 LAT high-level data

Once the LAT data are transmitted to the ground and to the LAT ISOC, the events are reconstructed and analyzed (as described in section 2.2) using a batch farm of several hundred computers at SLAC. The end result is two high-level data products in the FITS format: FT1 files are event lists with columns containing reconstructed physical quantities and parameters (e.g. energy, time, direction) for each event; FT2 files give the position and orientation

of the satellite every 30 seconds. The events are also classified into certain classes based on charged particle residual background rate, described in table 2.1.

## 3.3 Analysis methods

Our goal in this section is to elucidate the overall flow of analysis on LAT sources used to search for dark matter satellite candidates and to set a limit on the cross-section of a DM model. As argued in section 1.8, DM satellites may be distinguished by several features: No association with sources in other wavelengths (e.g. X-ray, radio, optical), no time variability, spatial extension, and a distinct spectrum. We therefore perform two tests on initial candidate sources, a spectral test comparing its spectrum to a DM annihilation spectrum and a power law spectrum, and a test for spatial extension with the NFW profile.

After describing our data set, the first step is to define our tests in terms of the Test Statistic, and the criteria for passing each test, i.e., finding a cutoff value for the TS of each test which causes us to reject the null hypothesis. There is a tradeoff between test significance and efficiency; if we require a larger significance, there is a greater likelihood for a true alternative hypothesis source to have a significance that falls below the chosen threshold. We choose cutoff values for both our tests such that each will have a significance level of 0.01, meaning the TS cutoff value is the TS which 99% of true null hypothesis sources will fall under. We refer to these values as $\mathrm{TS}^{99}_{ext}$ and $\mathrm{TS}^{99}_{comp}$ for the extension and spectral tests, respectively. We ascertain these values with simulations in the case of the spectral test, and use Chernoff's theorem for the spatial extension test.

In the event of a non-detection (either in our analysis or of further study of

sources that may pass our tests), we may set limits on DM model parameters with some level of statistical confidence. This requires two pieces of information: the efficiency of detection, and the statistics of galactic subhalos. The efficiency is a measure of how often a (simulated) extended DM source of a given flux, extension, and particle model will pass the tests, and we find our efficiency via performing our tests on large sets of such sources. From the galactic subhalo statistics of the VL2 and Aquarius simulations, we can calculate their observed extension from our vantage point 8.5 kpc from the galactic center, and their flux based on the DM particle model and their density profiles. Thus we can estimate the likelihood of a given satellite passing both tests, and we can set a limit on the annihilation cross section by increasing it until the probability of a null observation is at the desired significance level.

In Figs. 3.2 and 3.3, we show two flowcharts which, respectively, summarize the overall analysis, and then specifically our source analysis chain.

### 3.3.1 Dataset

From 3 years of data (August 8, 2008 − August 7, 2011), events are selected according to the collaboration's agreed upon high-level analysis standards and caveats [107]. Only "source" class events (previously known in Pass 6 as "diffuse" class) between 1 GeV and 317 GeV are used (317 was chosen as it makes the energy interval a half-integral number of decades in energy logarithmically, to align with the bins used for the PSF parameters by the Fermi calibration database). Analysis of simulated sources for a variety of energy ranges showed that excluding events below 1 GeV generally improved the signal-to-background ratio and caused the *pointlike* fitting software to converge more often for lower flux sources. The higher energy range also has the advantage of a smaller PSF. In order to avoid contamination from the Earth's albedo, a zenith angle cut of 100° is applied as well as a rocking

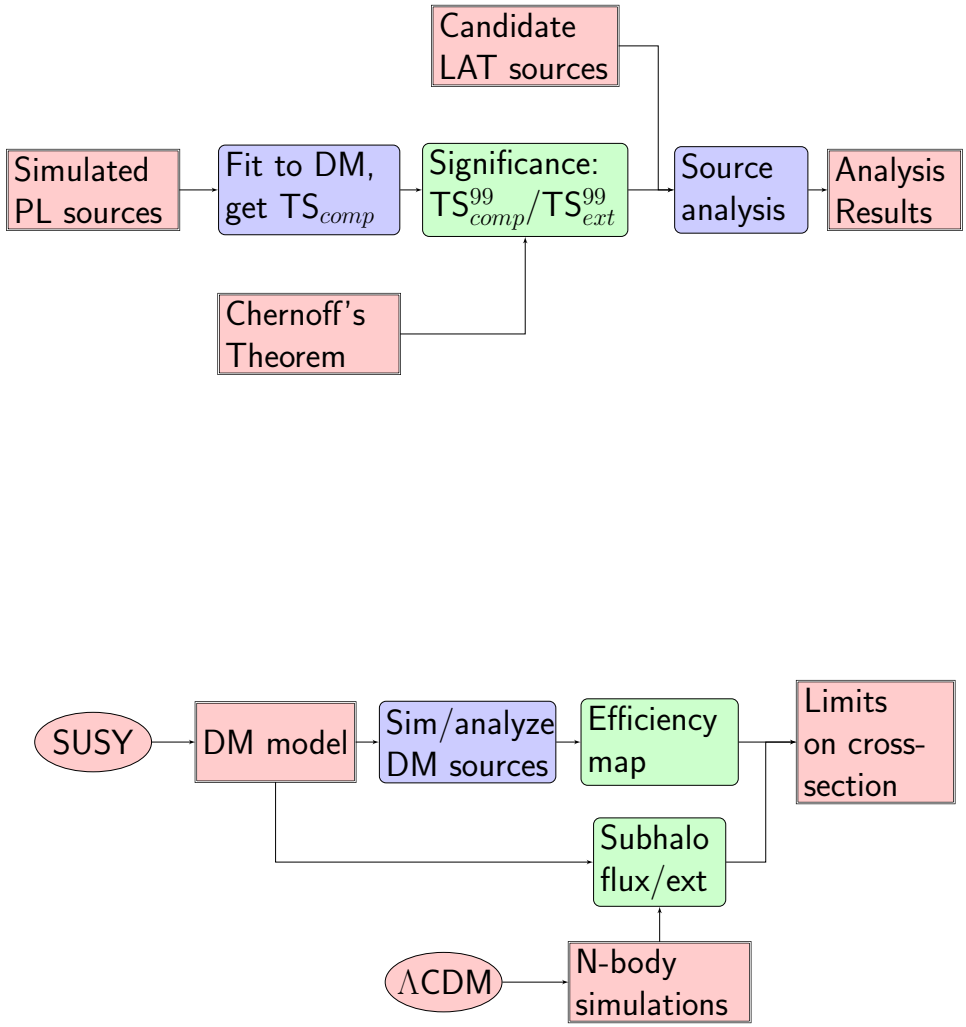


Fig. 3.2: Two flowcharts; the top illustrates the broader analysis chain, the "source analysis" block of which is shown in more detail in Figure 3.3; the bottom outlines the calculation of limits set on cross-section for a non-detection.

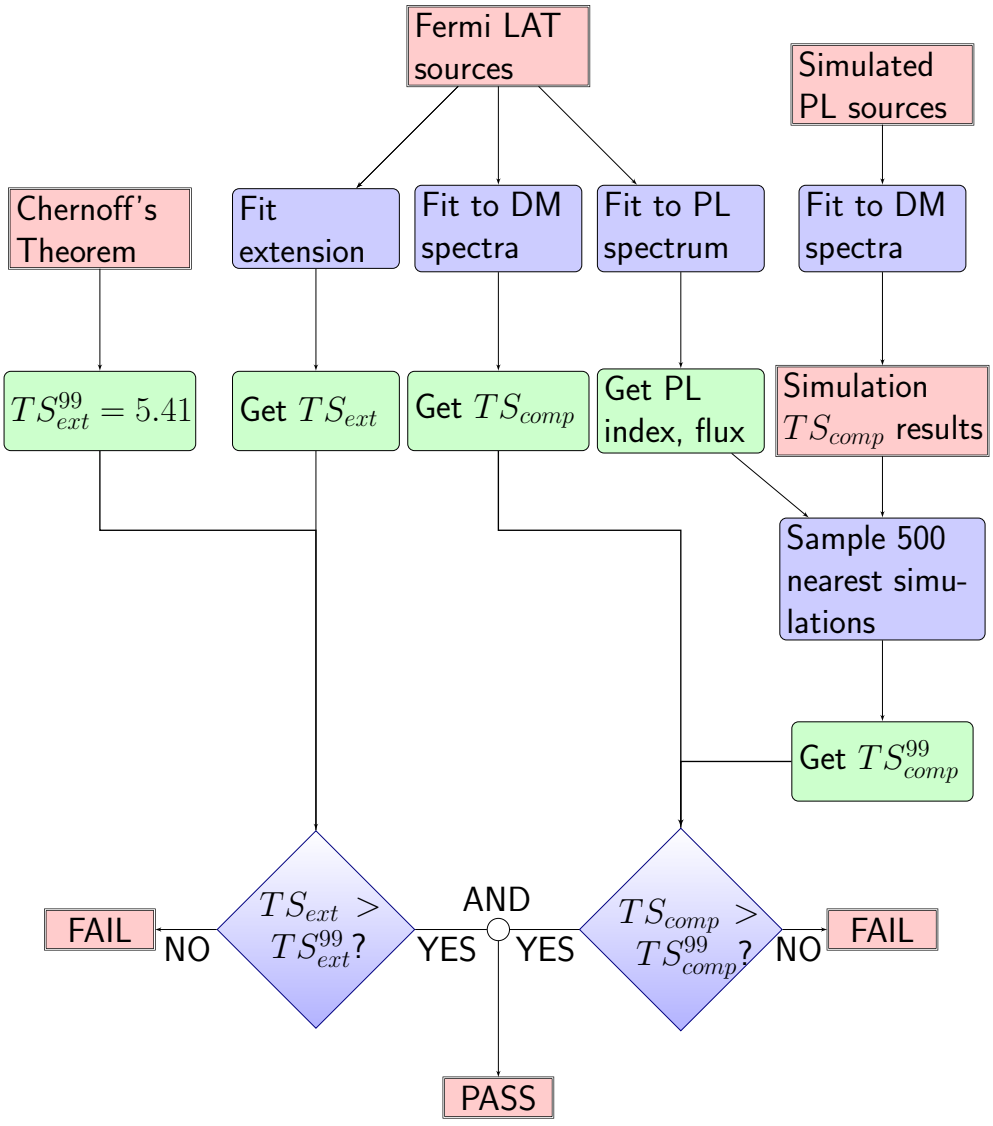


Fig. 3.3: Flowchart illustrating our source testing procedure. The spatial test on the left is relatively straightforward and described in section 3.3.3. The spectral test on the right draws from a large set of simulations, and will be explained in detail in section 3.3.4.

angle (the angle the instrument z-axis makes with the zenith angle) cut of 52°. The data were processed and analyzed using the P7SOURCE_V6 IRFs and ScienceTools version v9r30p1.

### 3.3.2 Initial candidate source selection

The 3-year catalog is a collection of high energy gamma ray sources detected by the LAT during the first 3 years of data, along with associations to sources in other catalogs found at other wavelengths. This catalog was compiled internally and is not published. It was compiled using the same detection, localization, and automatic association pipeline (uning *pointlike*) as the 2FGL catalog [68] with some minor improvements. Source detection involves identifying potential point sources (called "seeds") through wavelet-based methods (as in image processing), a full-sky optimazation of a model of the gamma ray sky including the new seeds, and a creation of a residual Test Statistic map, where the TS is evaluated as $\mathrm{TS} = 2\ \ln(L(source)/L(nosource))$. This process also performs local optimizations of the position of each point source. A threshold of $\mathrm{TS} > 25$ is applied to all sources, and the energy range $100\ \mathrm{MeV} - 100\ \mathrm{GeV}$ is used throughout this process. Source associations use a Bayesian approach that trades the positional coincidence of possible counterparts with 2FGL sources against the expected number of chance coincidences to estimate the probability that a specific counterpart association is indeed real (i.e., a physical association). Further details on this method can be found in [3]. Counterparts are retained as associations if they reach a posterior probability of at least 80%. This method is applied to a set of counterpart catalogs. The expected false association rate is better than 5%.

The 3-year source associations however have not yet undergone a detailed review by hand as thorough as the 2FGL catalog, and the source list likely contains some unassociated sources which in reality have associations, or which

are spurious sources. This is not necessarily a fundamental problem for the analysis, but it does mean that we will have a larger initial candidate source list and have a slightly higher chance of identifying a false positive DM candidate.

Our initial set of candidate sources selects unassociated sources from the 3-year LAT Catalog above galactic latitude $|b| > 15$, in order to avoid the gamma ray background from the galactic disk. We also avoided any source in the Orion A and B molecular clouds, a region of the galactic background in which there is a known uncertainty in the diffuse models [5]. This results in an initial candidate list of 304 sources.

Although all catalog sources have a TS $> 25$ (as this is the TS cut for a source to make it into the catalog), this value is based on the TS estimation method used by the catalog group, which gives the TS for the energy range 200 MeV $-$ 300 GeV, when the source is analyzed as a point-like power-law source. Because our analysis uses the more narrow $1 - 317$ GeV range, we do not necessarily expect *pointlike* to be able to identify all these sources at such significance, as some of the significance of softer sources will come primarily from the lower end of the spectrum. It is possible however for a source to have a negative TS value to a spectral fit in an energy band, so a TS $> 25$ in our energy range does not absolutely guarantee TS $> 25$ in a wider range which includes ours. To be perfectly consistent then, we should also do our own sky search using the procedure for the 3-year catalog in order to find such sources. We estimate by the following means, however, that it is very unlikely that DM satellites would appear as such sources.

Considering the spectra of DM annihilation in Figure 1.6, $\tau^+\tau^-$ annihilation of a high-mass particle would be most likely to cause a source to appear as pathologically hard, since it would have a greater fraction of its flux in the $1 - 317$ GeV energy range compared to other DM annihilation spectra. We

simulated 3000 such sources of DM mass 300 GeV in the $200\,\mathrm{MeV} - 317\,\mathrm{GeV}$ energy range with extended NFW profiles and photon fluxes near the cusp of detectability (randomly spaced logarithmically between $3\times10^{-10}$ and $1\times10^{-9}$ GeV in the $1-317$ GeV energy range) at random places in the $|b| > 15$ sky over background, and analyzed them with *pointlike* as point-like power-law sources in two energy ranges, that of the catalog values, $200\,\mathrm{MeV} - 317\,\mathrm{GeV}$ ($TS_{200M}$), and the range of our analysis, $1-317$ GeV ($TS_{1G}$). We then found the fraction of sources that were fit with $TS_{200M} < 25$ but $TS_{1G} > 25$. We found that of the 3000 sources, 1656 of them were fit with $TS_{1G} > 25$, and of these, 13 were fit with $TS_{200M} < 25$, or less than 1%. This percentage would almost certainly be smaller for other masses and annihilation channels as we already argued. This strongly suggests that an independent sky search is unnecessary.

### 3.3.3 Spatial Test

Here we describe the test for spatial extension of LAT sources. As mentioned in section 1.7, N-body simulations predict that the structure of the Milky Way's DM halo is likely to have several subhalos with significant angular extension, up to a few degrees. These simulations also predict that these subhalos can generally be well approximated by a common density profile, the NFW profile (equation 1.6), which we use to model DM sources. While the LAT has the capability to detect extension of at least 0.5°, recent simulations [56] show that in general it may not have the capability to distinguish some common density profiles from one another. This does allow us to regard the NFW profile as a generic representative of other possible profiles that may manifest in substructure, but prevents us from testing predictions made by different models of DM about halo density profiles.

For an NFW dark matter distribution with scale radius $r_s$ at a distance

$D$, the angular extent of a satellite can be characterized by the parameter $\alpha_0 = r_s/D$. *Pointlike* uses a likelihood ratio test to analyze sources for extension, defined as

$$TS_{ext} = -2 \ln \frac{L_{point}}{L_{NFW}} = TS_{NFW} - TS_{point} \tag{3.6}$$

where $TS_{point}$ is the TS of the null hypothesis, the assumption that the source has an extension much smaller than the LAT PSF, and $TS_{NFW}$ is the TS when $\alpha_0$ was fit as a free parameter. The position of the source was also optimized in the fit.

As mentioned in the introduction to this section, we wish our test to have a significance of $p = 0.01$, so we make a cut on $\mathrm{TS}_{ext}$ such that 99% of point sources will fall under this value, which we call $\mathrm{TS}^{99}_{ext}$. Since the NFW and point hypotheses are nested, we use Wilks' and Chernoff's theorems to get this value from eqn. 3.4, $\mathrm{TS}^{99}_{ext} = 5.41$.

### 3.3.4 Spectral Test using the Comprehensive Test

Here we describe the test used to distinguish a WIMP DM spectrum from a power-law spectrum, which generically represents common astrophysical sources. We test 2 different annihilation channels, $b\bar{b}$, and $\tau^+\tau^-$. The spectra of various channels plotted in Figure 1.6 shows that $b\bar{b}$ is also generally a good representation of other hadronic channels and also $W^+W^-$, while the $\tau^+\tau^-$ is very distinct. The dark matter model spectra are simulated with the DMFIT [50] package, a tool used to simulate and fit dark matter spectra based on DarkSUSY [45].

In contrast with the spatial test, where the point model (null hypothesis) is nested within the extended model (alternative hypothesis), the power law and dark matter spectra are not, so the proper way to compare their statis-

tical significance is not immediately obvious. This is a familiar problem in source analysis. In the past (as in the previous subhalo analysis), the general practice has been to simply consider the difference in TS values between the two models, $\mathrm{TS}_{\mathrm{diff}} = \mathrm{TS}_{DM}$ - $\mathrm{TS}_{PL}$, but it is not clear whether this is a statistically rigorous means of comparison.

It is possible however to construct a "comprehensive hypothesis" from two non-nested hypotheses within which the null hypothesis is nested. Consider two functions $f(x_1)$ and $g(x_2)$. The comprehensive hypothesis is then

$$h(x_1, x_2, \alpha) = f(x_1)^{1-\alpha} \times g(x_2)^{\alpha}, 0 \leq \alpha \leq 1 \tag{3.7}$$

where $h(\alpha = 0)$ represents the null hypothesis, and $h$ with $\alpha$ free is the alternative hypothesis. In our case, $f$ is a power-law spectrum with floating spectral index, and $g$ is one of two DM annihilation spectra, with floating mass. We use *pointlike* to perform this test. The TS of this test should be strictly higher than that of the null hypothesis $f$, and we call the test statistic for this test $\mathrm{TS}_{comp}$, defined as

$$TS_{comp} = -2 \ln \frac{L_{PL}}{L_{comp}} = TS_{comp} - TS_{PL} \tag{3.8}$$

i.e., the difference between the test statistics of the comprehensive hypothesis and the power law hypothesis. This comprehensive hypothesis forms the basis of our spectral test.

The comprehensive hypothesis has three floating parameters to fit, and this makes for a very large parameter space. It can be difficult for the fitter to explore the parameter space sufficiently and may stay too close to its starting parameters, or neglect to move one very much, so we seek to ameliorate this by fixing the $\alpha$ parameter to different values and then performing the fit over the other two parameters. This is done over 9 uniform values from $0.1 - 0.9$.

We then perform the fit a final time leaving $\alpha$ free but initializing it at the value where it achieved the best fit.

Like our spatial test, we also want our spectral test to have a significance of 0.01, so we will make a cut on $\mathrm{TS}_{comp}$ such that 99% of simulated null hypothesis (point power law) sources will fall below this threshold value. In contrast to the spatial test, where we generally expect non-DM sources to be fit well by the null hypothesis, we do not necessarily expect all non-DM LAT sources to conform closely to power law spectra. Pulsars especially may have exponential cutoff spectra that can resemble the particle mass cutoff of DM annihilation (Figure 3.4). The disadvantage is that we cannot make a very precise estimate of the expected false positive background for this test; the ostensible rate of 1 in 100 implied by a $\mathrm{TS}^{99}_{comp}$ is instead a lower limit which is only as good as the approximation of actual non-DM source spectra to power-law spectra. There is also the seeming difficulty in interpreting the meaning of a fit in which say $\alpha = 0.5$. Neither of these present a fundamental statistical problem however: it should be kept in mind that all we are attempting to do in a frequentist test such as this is reject the null hypothesis; $\mathrm{TS}_{comp}$ is the significance for rejecting the null hypothesis and not identically the significance of the DM spectrum fit, but by choosing the alternative as a DM spectrum, we make the test more sensitive to sources with that spectrum.

If Wilks' and Chernoff's theorems apply, then we expect the distribution of $\mathrm{TS}_{comp}$ for the nested model ($f$) to be asymptotically distributed as half having $\mathrm{TS}_{comp}$ of zero, and half going as a $\chi^2$ distribution with degrees of freedom equal to the extra dimensionality, which is ostensibly 2 ($\alpha$ and $x_2$) in this case. If it holds, we would be able to pick our $\mathrm{TS}^{99}_{comp}$ from this function. This also implies that the $\mathrm{TS}_{comp}$ distribution should be independent of the parameters of the models $f$ and $g$. That is to say, our sensitivity should be the same across the whole range of flux and spectral index that we test (as

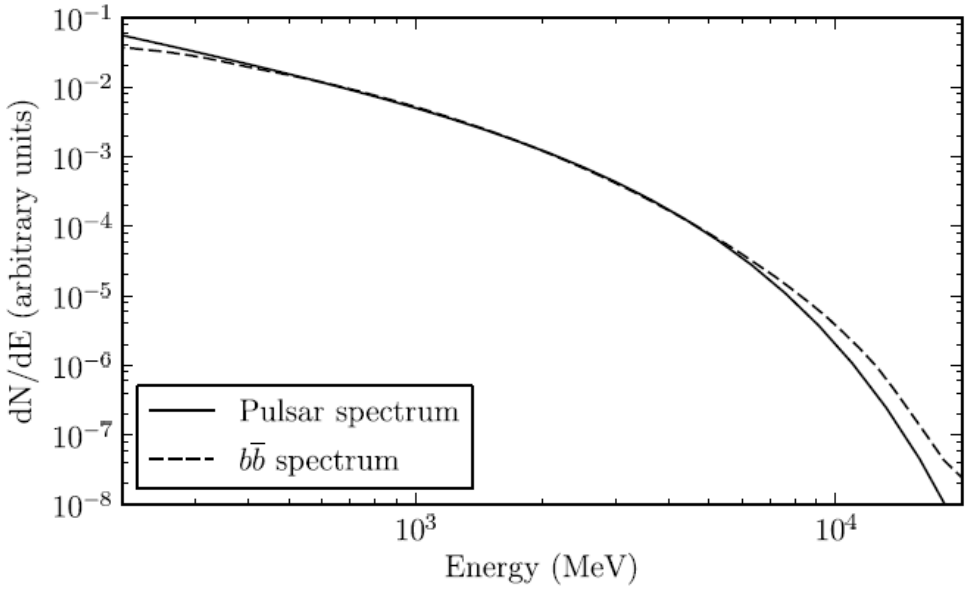


Fig. 3.4: Best-fit exponentially cutoff power law (with $\Gamma = 1.22$ and $E_{cut} = 1.8\,\mathrm{GeV}$) of the millisecond pulsar 1FGL J0030+0451 (solid line) and the best-fit $b\bar{b}$ spectrum (with $M_{\mathrm{WIMP}} = 25GeV$) of this pulsar (dashed line). From [8]

long as we can significantly distinguish source from background, as per the requirement that we be able to marginalize over the nuisance parameters of the background emission).

It is far from clear however whether these theorems apply, so one of the sub-goals of this analysis is to see how well the predictions of these theorems hold. To test this, we ascertain $\mathrm{TS}^{99}_{comp}$ using a large set of simulations: we consider a range of flux-index space which encloses the range of fit values (when fit as a point power-law source) of the candidate source spectral parameters, and simulate 21,000 sources in this space. This range, along with the fit values of the candidate sources plotted on top, is shown in Figure 3.5. To determine the threshold significance for given flux and index, we take the nearest 500 simulated sources ('nearest' in parameter space which also pass the $TS_{PL} > 25$ cut to those parameters, and find the threshold $\mathrm{TS}^{99}_{comp}$ value from among these

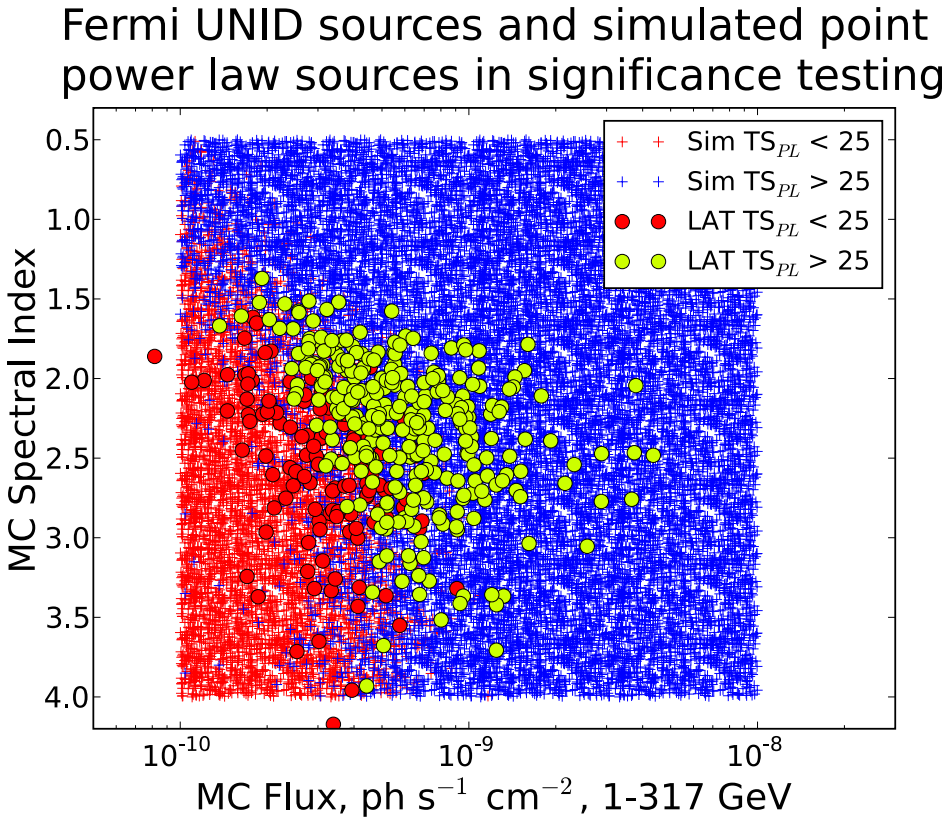


Fig. 3.5: Plot showing the range of flux/index values of LAT candidate sources (circles) and the space of simulated point power-law sources used to ascertain $\mathrm{TS}^{99}_{comp}$ (small crosses). The sources are also color-coded based on whether they pass the $TS_{PL} > 25$ cut, which shows where the limit of detection of point power-law sources is for our test. The consistency of this limit between LAT sources and simulated sources is a good check on this part of our analysis.

sources (i.e., the 495th highest $\mathrm{TS}^{99}_{comp}$ among them). An example is depicted in figure 3.6.

In this way, each source we wish to test can be said to have its own "personalized bin," and so will have its own unique $\mathrm{TS}^{99}_{comp}$, associated with its fit spectral parameters (when fit as a power-law spectrum). This applies not only to our candidate LAT sources, but also to our set of simulated DM sources which we will use to find the efficiency of detection (which we will describe in section 4.2); we will fit them as power-law sources, find their $\mathrm{TS}^{99}_{comp}$, and then compare that to the $\mathrm{TS}_{comp}$ from the fit with the comprehensive test.

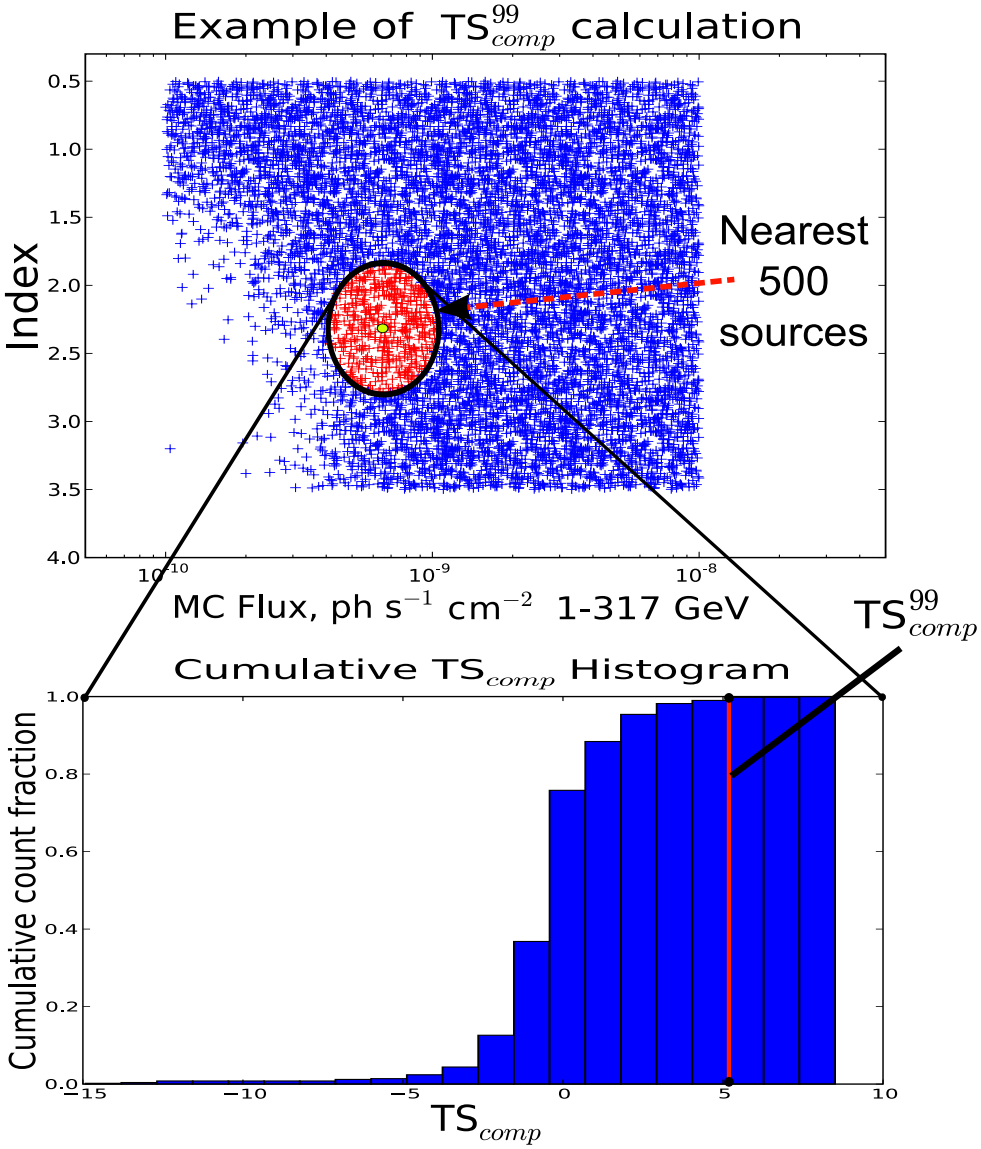


Fig. 3.6: Example of how $TS^{99}_{comp}$ is found. The top figure shows in blue crosses the set of simulated power-law sources, and in red crosses the specific selection of the 500 nearest simulated point power law sources whose $TS_{comp}$ are to be tested against. The bottom figure is a cumulative histogram of those $TS_{comp}$ values, and the red line marks 99th percentile value, our $TS^{99}_{comp}$ for that source.

We sample this parameter space and plot the $\mathrm{TS}^{99}_{comp}$ found in figure 3.7, interpolating between sample points. This interpolation is for the purposes of illustration, the actual $\mathrm{TS}^{99}_{comp}$ calculation is done in full for every source. If Wilks' and Chernoff's theorems apply here, then we should expect $\mathrm{TS}^{99}_{comp}$ to be uniform across the parameter space (at least within the range where we can accurately account for the background) and we could characterize the test significance with a single value, as we did with the extension test.

The nonuniformity of figure 3.7 seems to indicate that these theorems do not strictly apply. While $\mathrm{TS}^{99}_{comp}$ does not seem to depend strongly on flux, there is some variation with spectral index. The $\mathrm{TS}^{99}_{comp}$ increases with increasing spectral index until around 1.7, above which it becomes more consistent, although there is still a good deal of inhomogeneity. An explanation for this may be that very hard power-law spectra have the least resemble DM annihilation spectra particularly at higher energies, because the mass cutoff in the spectrum becomes a poorer and poorer fit, and the statistics in the higher energy bins for hard sources has a greater effect on the fit. When the power-law spectrum is soft enough, fluctuations in statistics can more often resemble the mass cutoff and curvature of the spectrum. The $\mathrm{TS}^{99}_{comp}$ for the $\tau^+\tau^-$ spectrum however begins to decrease again when the index is greater than 3.0, and it's unclear how to explain this. The inhomogeneities are likely due to the fact that the $\mathrm{TS}^{99}_{comp}$ calculation is sensitive to only the top few $\mathrm{TS}_{comp}$ values, so a couple particularly high $\mathrm{TS}_{comp}$ values can have a marked influence on the local $\mathrm{TS}^{99}_{comp}$ value.

It's also unclear whether the comprehensive hypothesis has in fact 2 more degrees of freedom than the null hypothesis, because there is some degeneracy in the comprehensive hypothesis parameter space. For example, it is possible to represent a pure dark matter spectrum by taking the $\alpha$ parameter to 1, or by taking the spectral index to a large value so as to make the power-law

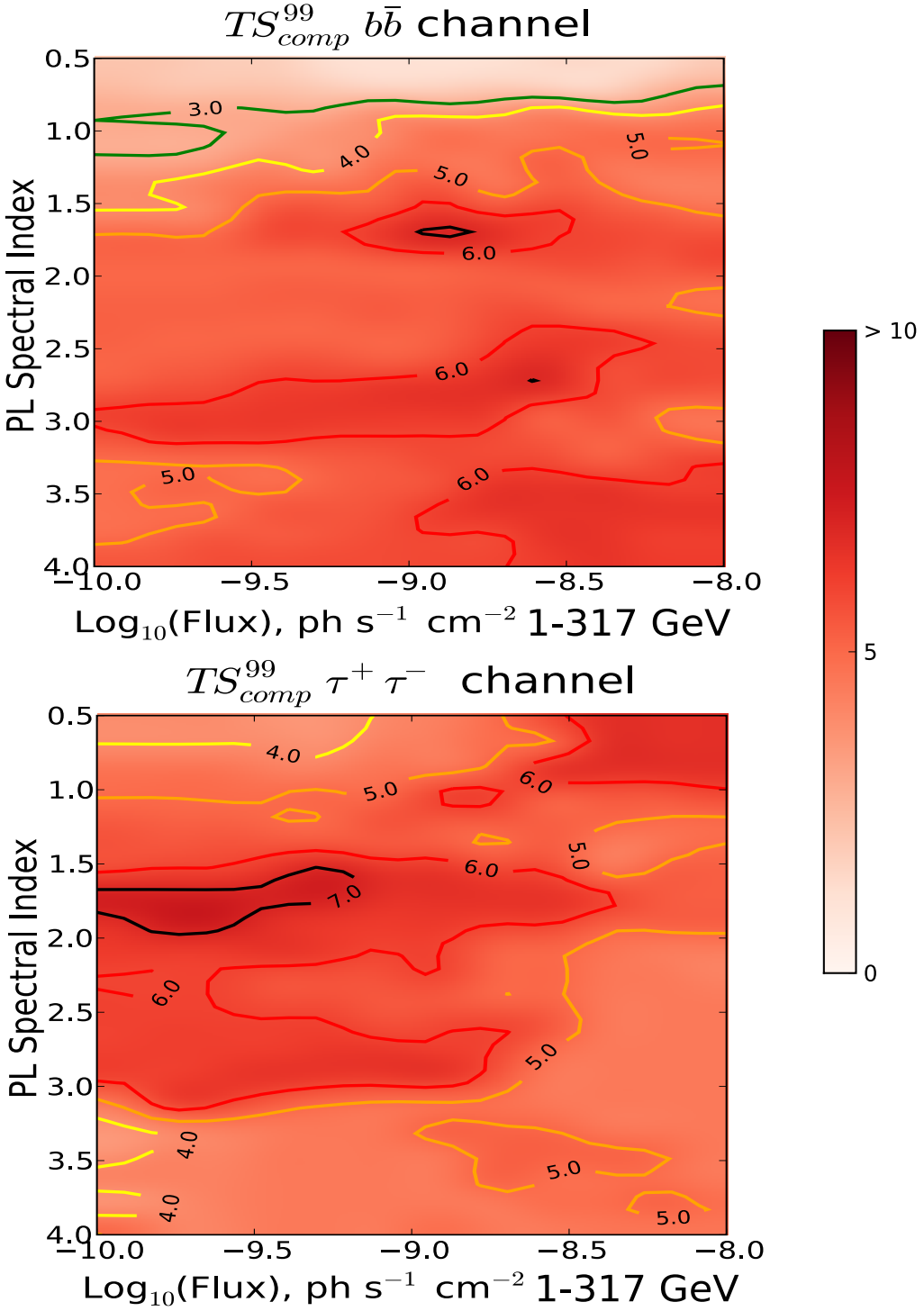


Fig. 3.7: Color map of $\mathrm{TS}^{99}_{comp}$ for $b\bar{b}$ and $\tau^+\tau^-$ annihilation. The flux/index range was sampled and $\mathrm{TS}^{99}_{comp}$ was calculated for each sampled point, and then bicubic interpolation was done to fill in the map. The darker regions indicate where $\mathrm{TS}^{99}_{comp}$ is largest, i.e., where fluctuations in the null hypothesis spectrum are more likely to resemble DM annihilation.

component so soft that it doesn't contribute at all. So the observations here suggest there is likely some finer point at work here and that there is still work to be done on the statistical front, although the lack of strong dependence on flux gives some indication that it may be possible to represent the significance by some analytic function representing how different the two spectra are, such as the cross-correlation. A functional representation of the $\mathrm{TS}_{comp}$ distribution would be quite valuable, since it allows a simple functional characterization of the significance of a test, instead of spending a large amount of computer time on finding it with MC simulations. The problem of comparing non-nested hypotheses is a very general problem, so work towards this end would likely find broad application.

A couple points bear mentioning here. Note that in the upper panel of figure 3.6, there is a patch in the lower left of the parameter space where the density of simulated sources decreases down to basically zero. This represents the threshold of detection according to the $\mathrm{TS}_{PL} > 25$ cut. As we approach this threshold, the $\mathrm{TS}^{99}_{comp}$ becomes skewed more and more, as the nearest 500 sources will be disproportionately of higher flux and slightly harder. As can be seen in 3.5, no LAT sources fall too far into this range, but we don't know ahead of time that this will be the case for the simulated DM sources that we will use in our efficiency calculations. This effect can be mostly ignored for a couple reasons. The first is that, as will be seen, the efficiency of the extension test is also very low around this threshold, making it unlikely that sources whose $\mathrm{TS}^{99}_{comp}$ values are skewed will have much effect in the combined efficiency of all three tests (spectral, spatial, and the $\mathrm{TS}_{PL} > 25$ cut). The other is that considering figure 3.7, $\mathrm{TS}^{99}_{comp}$ does not have strong dependence on flux, while $\mathrm{TS}^{99}_{comp}$ increases slightly as the spectrum gets harder relative to this threshold (since it is mostly below the index where the peak $\mathrm{TS}^{99}_{comp}$ is found), making the skewed $\mathrm{TS}^{99}_{comp}$ cut a bit more exclusive than it might

otherwise be, so to the extent that this effect does factor into our overall efficiency, it likely results in it being slightly more conservative.

There also is a seeming arbitrariness in the way "nearness" has been defined, as there is no reason *a priori* for a half-decade in flux to be considered the same "distance" as a difference of 1 in spectral index. A more natural idea of "distance" might take into account the estimated error of the spectral parameters, and so we might draw ellipses instead of circles. We make the simplification of using circles for a couple reasons. The general scale of errors in flux and index are not unreasonably different; the $1\sigma$ index error typically is around a factor of 0.1 (for a difference of 0.1 - 0.3), and the flux error is around 0.5, or about 0.17 of a decade in energy. The relative scale here is also very similar to the one used for the $TS^{99}$ interpolation in the previous subhalo analysis.

# Chapter 4

# Results and discussion

## 4.1 Search for Dark Matter Satellites in LAT Unassociated Sources

Applying the $TS^{99}$ cuts on extension and spectra to our set of 304 candidate sources, we find that 10 pass the extension cut, but none of these pass the spectral test for any annihilation channel considered. Given that our extension cut was at the 99% significance level, 10 out of 304 sources is greater than the background number of detections we might expect for extension; the binomial distribution gives approximately a 0.1% chance of this happening by chance, so it is possible that some of these sources are actually extended. Though, our extension test significance is likely a bit worse than 0.01, because one of the assumptions that went into the use of $TS^{99}_{ext} = 5.41$ was that we can perfectly model the background, which is not the case

As for the spectral tests, 30 passed the $b\bar{b}$ spectral test and 21 passed the $\tau^+\tau^-$ spectral test. As we remarked in the section describing the spectral test, this relatively large number is somewhat expected, as our null hypothesis for the spectral test was a power-law, and some ordinary astrophysical sources will have spectra that are not closely modeled by a power-law over 2.5 decades

of energy. Passing the spectral test only implies that a DM annihilation spectrum fits the source spectrum better than the null hypothesis, which can be due more to the power-law fit being poor than the DM fit being particularly good. Pulsars in particular may closely mimic DM annihilation (although they will never appear as extended sources), so it's unclear how to estimate the background number of sources we should expect to pass our test.

## 4.2 Calculation of upper limits on DM annihilation cross-section

In order to calculate a cross-section upper limit we require two pieces of information: the efficiency of detection, and the statistics of galactic DM satellites. For the first, we must find our tests' efficiency of detecting DM satellites with varying flux, DM mass, and spatial extension, which we determine with Monte Carlo simulations. Then using the VL2 and Aquarius simulations, we estimate the likelihood that satellites of varying $J$ and extension exist from Earth's vantage point 8.5 kpc from the galactic center. For a given $\langle \sigma v \rangle$, DM particle mass, and annihilation channel, we can calculate the expected photon flux, and in turn the detection efficiency, of each satellite. Based on the discussion of low-mass satellites in section 1.8, we do not consider low-mass satellites in this analysis. We set the cutoff for consideration to be an order of magnitude less than the conservative lower bound on the $J-$factor of the Draco dwarf spheroidal galaxy, taken to be $10^{11} M_{\odot}^2\,\mathrm{kpc}^5$ [100], since the strongest limits on the annihilation cross-section result from its analysis.

We can then estimate the likelihood (averaged over all N-body simulations) not to observe any DM satellite for this $\langle \sigma v \rangle$. We then find the $\langle \sigma v \rangle$ where this probability becomes 5%, which is the 95% confidence upper limit for $\langle \sigma v \rangle$ for the given DM mass and annihilation channel. We calculate upper limits

for the masses 50, 100, 200, 500 GeV in each of the $b\bar{b}$ and $\tau^+\tau^-$ channels.

### 4.2.1 Detection efficiency

The efficiency is defined as the fraction of simulated DM satellites which pass both our tests. The efficiency will depend on the satellite's extension and spectrum in addition to its brightness, so we simulated across a range of these parameters for several DM models. This range spans in flux from $1 \times 10^{-10}$ to $1 \times 10^{-8}$ photons $s^{-1}$ $cm^{-2}$, and in extension (as defined by the parameter $\alpha_0 = r_s/D$) from 0.5° to 4°. The minimum of this range of extensions was chosen based on the threshold of detection of extended sources as reported in [56], and the maximum was chosen based on the most extended sources found in the N-body simulations. This parameter space is cut into 12 bins, 4 in flux and 3 in extension, both logarithmically scaled. For each DM model we simulated 1000 sources randomly inside each bin with NFW profiles using the *gtobssim* tool (part of the ScienceTools package), using the actual FT2 file from 3 years of LAT spaceflight, and performed our tests on these sources. Each source was placed at a random point on the sky with $|b| > 15$. We also excluded the region ($-21 < b < -15$, $205 < l < 217$) corresponding to the Orion A and B molecular clouds. The spatial and spectral tests are run on each simulated source, and sources which have $TS_{PL} > 25, TS_{comp} > TS^{99}_{comp}$, and $TS_{ext} > TS^{99}_{ext}$ are counted as detected. The spectral and spatial tests are done independently of one another, that is, the spectral test assumes the null hypothesis spatial model, and vice versa. The efficiency of our test for given flux and extension is the fraction of the nearest 500 sources which are detected, similar to our calculation of $TS^{99}_{comp}$. An example is depicted in Figure 4.1. The same caveats concerning "distance" in parameter space apply here as they did in the calculation of $TS^{99}_{comp}$, although the error on fit extension is typically larger than that of spectral index, so the relative scales of the errors

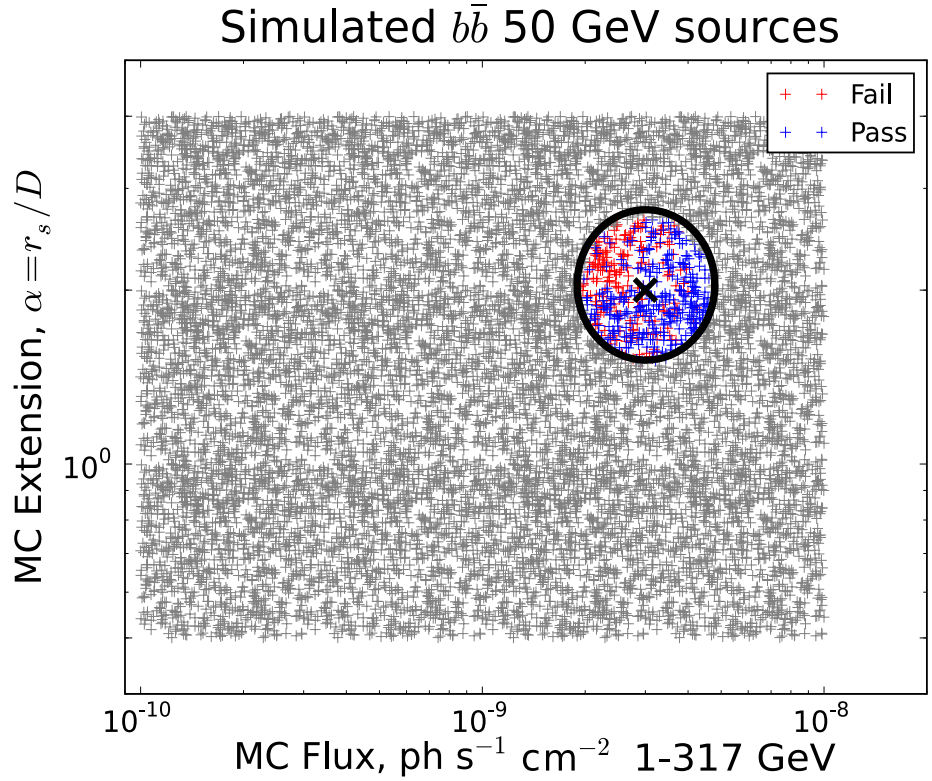


Fig. 4.1: Example of efficiency calculation. A point in the parameter space was selected, (flux,ext) $= (3 \times 10^{-9}, 2)$, and a circle is drawn around it containing the nearest 500 sources in parameter space. The efficiency at this point is the fraction of sources inside which pass our tests. In this case it is $\sim 0.65$

.

are a bit more similar here.

Again sampling across this parameter space and interpolating, we first plot the efficiency of the spectral and spatial tests separately in Figures 4.2 and 4.3, showing the 50 GeV $b\bar{b}$ and $\tau^+\tau^-$ model efficiencies as an example.

The spectral test efficiency decreases steadily for increasing extension. This may be expected given that for the same flux, a bigger extension spaces the same number of photons further apart, which makes them more difficult to resolve against the background as coming from the same source. The spatial test on the other hand first generally increases with increasing extension, as it becomes easier to separate the extension from the PSF, and then levels

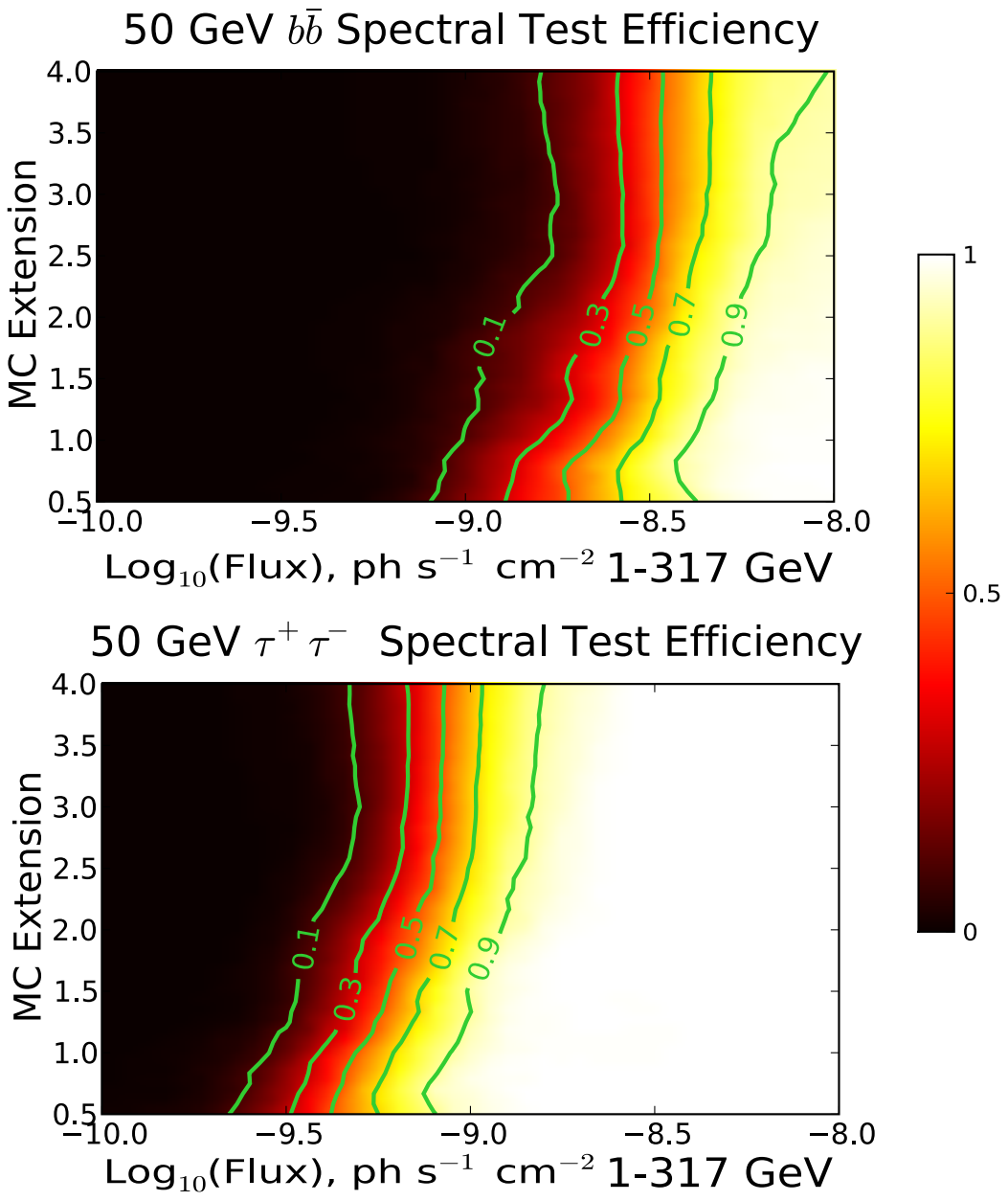


Fig. 4.2: Color map for the spectral test efficiency only.

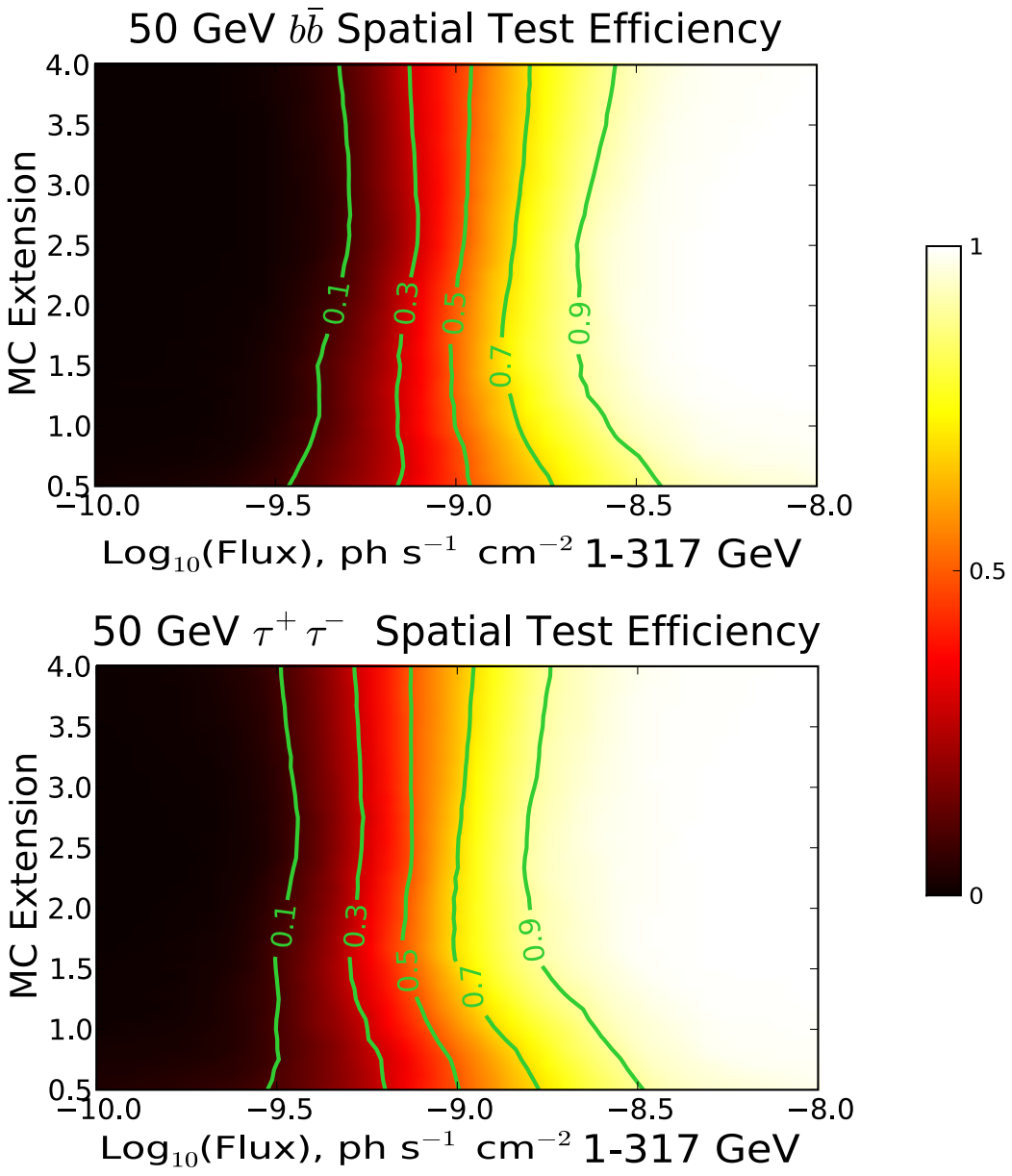


Fig. 4.3: Color map for the extension test efficiency only.

off as this effect competes agains the effect of larger extension resembling background. This is similar to the shape of the extension detection threshold as a function of extension found in the extended source search [56].

For the 50 GeV $b\bar{b}$ model, the spectral test efficiency is the limiting factor, so the map of the overall efficiency (Figure 4.4) more closely resembles the efficiency of that test. This is generally the case for the $b\bar{b}$ channel, whereas the opposite tends to be true for $\tau^+\tau^-$ channels. This can be attributed to the more distinct shape of the $\tau^+\tau^-$ annihilation spectrum, which makes it easier to distinguish from the null hypothesis power-law spectrum.

### 4.2.2 Realizations of N-body simulations

Given our test efficiency, we now need the statistics of the galactic subhalos to predict the likelihood of observing one in gamma rays, specifically the $J$-values (from which we calculate the expected flux using eq. 1.9) and spatial extensions for each satellite. The VL2 and the 6 Aquarius simulations are used to represent the Milky Way DM halo. The observed flux and extension will also depend on where Earth's vantage point is represented in these simulations, which may be at any point 8.5 kpc from the galactic center. For satellites close ($\lesssim$ 100 kpc) to the galactic center, different vantage points can have a noticeable effect. In order to account for this, we repeat the calculation of satellite $J$-values and extensions from 6 maximally-spaced vantage points on the 8.5 kpc sphere. These are referred to as realizations of a simulation. While the VL2 and 6 Aquarius simulations are statistically independent from one another, the realizations of each simulation are not. Thus, we have seven independent simulations, each with six interdependent realizations (referred to as the 42 "visualizations").

We calculate the $J$-value and extension for each satellite in each visualization using equation 1.11. This requires the input of the scale radius $r_s$ and

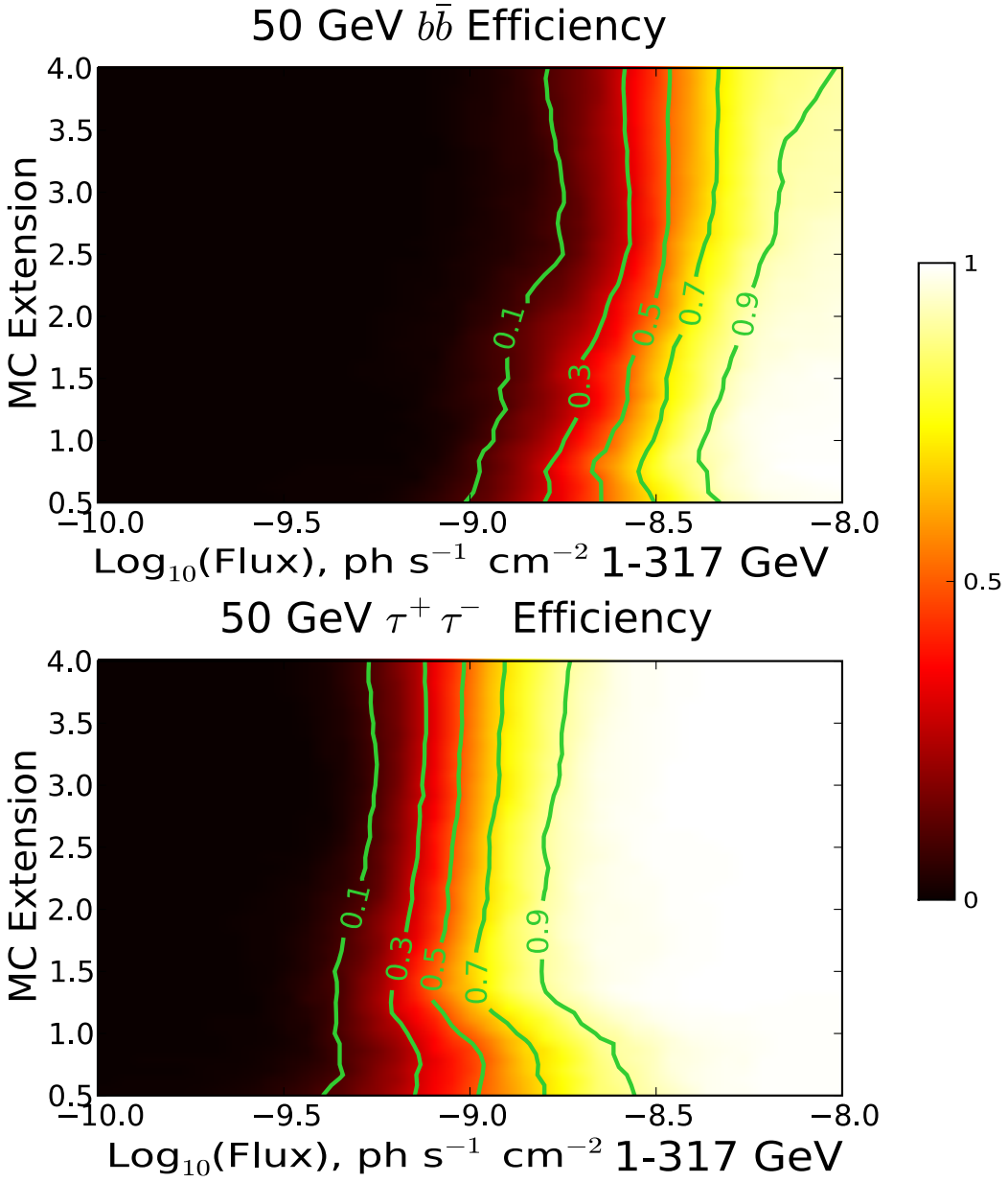


Fig. 4.4: Color map of efficiency

density $\rho_s$ for the satellite, which we do not have directly from the simulations. We make use of the relations in [55], which hold for an NFW profile:

$$r_s = \frac{r_{V_{max}}}{2.163} \tag{4.1}$$

$$\rho_s = \frac{4.625}{4\pi G}\left(\frac{V_{max}}{r_s}\right)^2 \tag{4.2}$$

with $r_s$ in kpc and $\rho_s$ in $M_\odot\,\mathrm{kpc}^{-3}$. $V_{max}$ is the peak circular velocity of the particles associated with a subhalo (in km/s), and $r_{V_{max}}$ is the radius (in kpc) where this velocity is achieved. $V_{max}$ is often used as a proxy for subhalo mass, since the virial mass of a subhalo itself may not be a well defined quantity in simulations — it strongly depends on the definition of the truncation radius and how unbound particles are removed. Thus for each visualization, we end up with a table of $J$-values and extensions of the satellites. Given a DM mass, annihilation channel, and $\langle\sigma v\rangle$, the photon flux of the satellite is then calculated according to equation 1.8, where the DMFIT package is used to calculate the photon yield $\Phi_{PP}$. We then assign the efficiency for detecting each satellite as explained in the previous section. In Figure 4.5, we illustrate an example where one realization's satellites, given a DM model and a cross-section, are plotted on top of that model's efficiency map.

### 4.2.3 Upper limits on annihilation cross-section

With the flux and extension from each satellite, for a given $\langle\sigma v\rangle$ and annihilation channel we can then assign a detection efficiency for each satellite in a given visualization using our efficiency maps. Since we interpret this as the probability to detect that satellite, we can write the probability that the

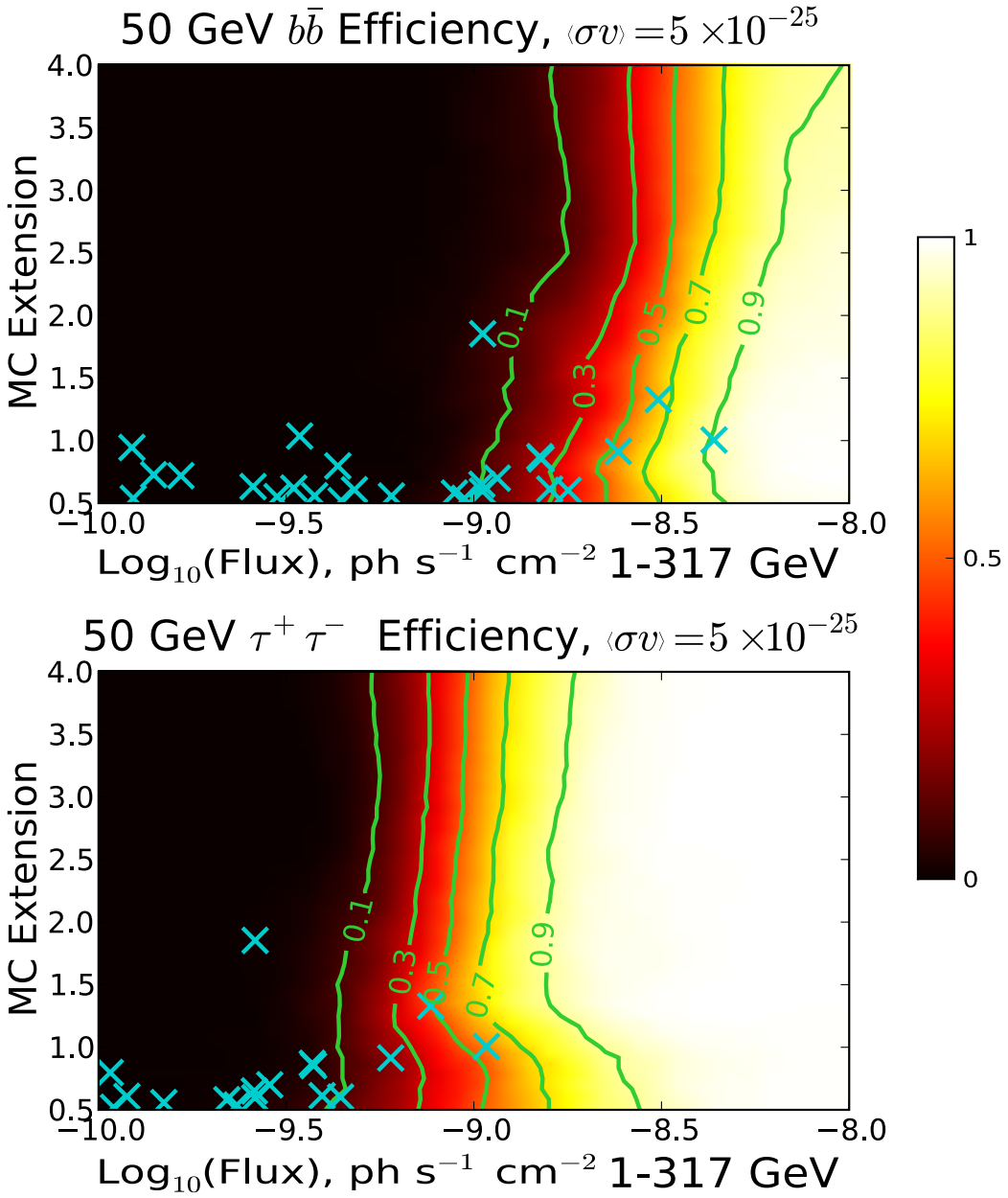


Fig. 4.5: Color map of efficiency, showing where satellites from one realization of the Aquarius N-body simulation fall for 50 GeV $b\bar{b}$ and $\tau^+\tau^-$ models, both with a $\langle\sigma v\rangle$ of $5 \times 10^{-25}$. Annihilation through the $\tau^+\tau^-$ channel for this mass produces fewer gamma rays per event by a factor of about 7 compared to the $b\bar{b}$ channel, so the subhalo flux is smaller by the same factor.

Table 4.1: 95% confidence upper limits on $\langle\sigma v\rangle$ for the 8 DM models examined

| | 50 Gev | 100 GeV | 200 GeV | 500 GeV |
|---|---|---|---|---|
| $b\bar{b}$ | $6.3 \times 10^{-25}$ | $9.7 \times 10^{-25}$ | $2.2 \times 10^{-24}$ | $9.5 \times 10^{-24}$ |
| $\tau^+\tau^-$ | $7.5 \times 10^{-25}$ | $1.75 \times 10^{-24}$ | $6.8 \times 10^{-24}$ | $4.1 \times 10^{-23}$ |

LAT would observe no satellites in visualization $i$ as

$$P_i(\langle\sigma v\rangle) = \prod_j (1 - \epsilon_{i,j}(\langle\sigma v\rangle)) \tag{4.3}$$

where $\epsilon_{i,j}$ is the efficiency for satellite $j$ in visualization $i$. We assume that the subhalos are distributed approximately isotropically in the sky, so that there is no reason to statistically prefer any particular visualization/realization, so we calculate the average null detection probability over the $N = 42$ visualizations as

$$\overline{P_i}(\langle\sigma v\rangle) = \frac{1}{N}\sum_i^N P_i(\langle\sigma v\rangle) \tag{4.4}$$

To set an upper limit on the DM annihilation cross section, we find the $\langle\sigma v\rangle$ where the probability of a null observation is 5%. In other words, the point at which there is a 95% probability that at least one satellite would have passed our tests if the subhalos were composed of DM with this $\langle\sigma v\rangle$. In Figure 4.6 we plot the 95% confidence upper limits for the masses and channels we considered, and list the values in table 4.1.

As a quick point of comparison to the previous subhalo paper, we set an upper limit of $9.7 \times 10^{-25}$ on the 100 GeV $b\bar{b}$ channel, an improvement by a factor of about 2. This is slightly better than what might be expected from the factor increase in signal-to-noise ratio from 1 to 3 years, $\sqrt{3} \sim 1.73$.

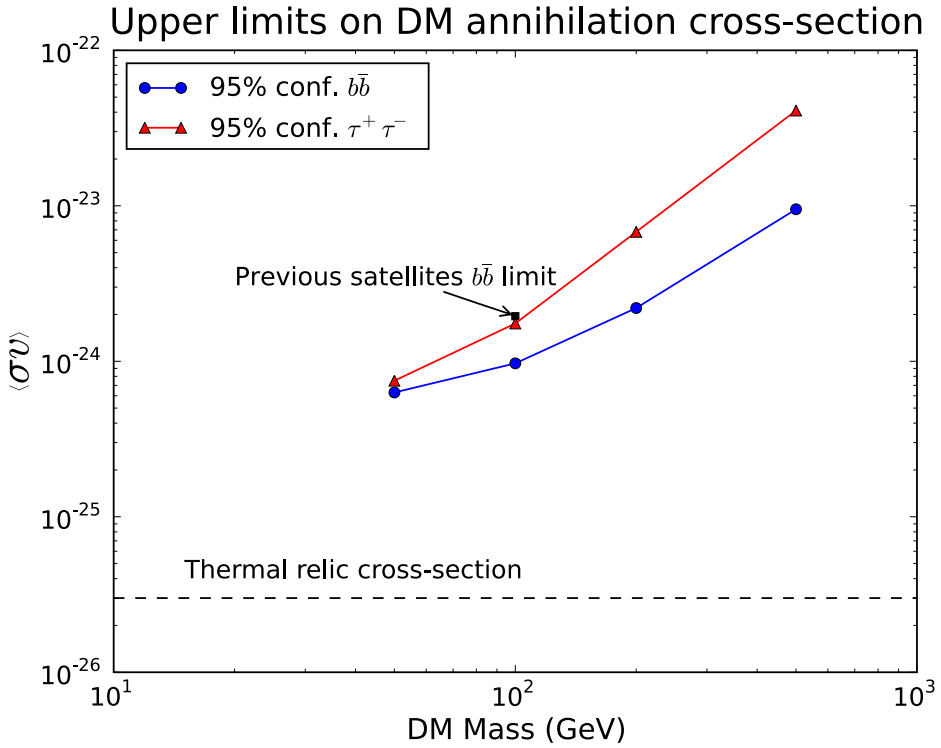


Fig. 4.6: 95% confidence upper limits from our analysis, compared to the limit set in the previous analysis (black square) and the thermal relic cross-section

## 4.3 Discussion

We analyzed unassociated sources in the 3-year Fermi LAT catalog in a search for dark matter substructure of the Milky Way using 3 years of data. Our analysis consisted of a spatial extension test, and a spectral test using the comprehensive hypothesis method, comparing to the $b\bar{b}$ and $\tau^+\tau^-$ annihilation channels. We found a small number of sources that passed either the extension or the spectral test, but none which passed both tests. We then used this null detection to constrain the annihilation cross-section of a few DM models. This was done using the predicted satellite distributions of the Aquarius and Via Lactea II simulations of DM halos in a $\Lambda$CDM universe, and our estimated efficiency for detecting these satellites from our own simulations. We assumed no boost from sub-substructure within these subhalos, and any boost factor one wishes to consider roughly lowers the upper limit further by the same factor. In particular, for the 100 GeV WIMP annihilating to $b\bar{b}$ studied in the previous such analysis, we find the 95% confidence upper limit to be $9.7 \times 10^{-25}$, a factor of 2 improvement from the previous subhalo search, and about a factor of 2.5 higher than the limits from the combined dwarf spheroidal analysis [57]. Even for the lowest mass we considered, our limit is still a factor of about 20 above the fiducial thermal relic cross section, so all other things being equal, 10 years of data will not be able to push this limit down to that level.

There are several ways we can improve our chances however. The primary source of error in the analysis is likely in our understanding of the significance of our spectral test. We do not have a reliable way to accurately estimate the significance of $\mathrm{TS}_{comp}$ *a priori*, so we rely on large sets of simulated null hypothesis sources to make the comparison. The practical limitations of computation here cause the $\mathrm{TS}^{99}_{comp}$ calculation to be somewhat imprecise, since

we have to make the comparison to sources whose spectral parameters differ a bit from the parameters of interest. This kind of imprecision is also found in the efficiency calculation. Further exploration of the comprehensive test and other ways of comparing non-nested hypotheses will help simplify and let us have more confidence in our spectral test. We also use a one-size-fits-all power law model as our null hypothesis, so better modeling of the spectra of AGNs and other astrophysical sources might allow for a better precision here as well.

Noting the plot of the subhalos from N-body simulations on top of the efficiency map, the extensions of many of these subhalos lie close to the threshold of extension detection, so even modest improvements in spatial resolution and extension sensitivity may go a long way towards lowering the upper limit that a satellite search may be able to set. Larger and more precise N-body simulations of DM halos may resolve some of the uncertainties in its distribution and spatial profile (especially in regards to sub-substructure, which can significantly boost the annihilation signal), allowing us to more closely model the Milky Way halo and its subhalos. Improvements continue to be made in modeling the diffuse background, which will broaden the available search area and reduce false positives in extension testing. And of course more data (perhaps up to 10 years) and computing power will come in the course of time. These improvements will allow any future analysis to increase the efficiency of detection and further lower the cross-section upper limit for null detections.

Our analysis used techniques developed in the previous DM satellite search and made several augmentations. Most notably, we used a new spectral test which may have very general application in source spectrum analysis and perhaps beyond. We also used an improved fitting program, and reduced computation time by using results from the search for spatially extended sources to establish our extension test significance via Chernoff's theorem. This allowed

us to set limits on 8 different DM models. The analysis used here can also be applied to any other models of DM annihilation spectra or subhalo profiles that others may wish to consider.

# Bibliography


[1] K. Abazajian, G. M. Fuller and M. Patel, *Phys. Rev. D*, **64**:023501. [arXiv:astro-ph/0101524].

[2] R. Abbasi, et al. [IceCube Collaboration], The IceCube Neutrino Observatory IV: Searches for Dark Matter and Exotic Particles, submitted to *32nd International Cosmic Ray Conference, Beijing 2011; part IV*, [arXiv:1111.2738 [astro-ph.HE]].

[3] A. A. Abdo et al., *ApJS*, **188**:405, 2010g.

[4] A. A. Abdo et al., *Physical Review Letters*, **104**:101101.

[5] M. Ackermann et al., Gamma-ray observations of the Orion Molecular Clouds with the Fermi Large Area Telescope, *ApJ*, **756**:4, 2012. [arXiv:1207.0616 [astro-ph.HE]].

[6] M. Ackermann, et al. [Fermi-LAT Collaboration], The Fermi Large Area Telescope On Orbit: Event Classification, Instrument Response Functions, and Calibration, *ApJS*, **203**:4, 2012. [arXiv:1206.1896v2 [astro-ph.IM]].

[7] M. Ackermann et al. [Fermi-LAT collaboration], Constraints on the Galactic Halo Dark Matter from Fermi-LAT Diffuse Measurements. *ApJ.* **in press**. [arXiv:1205.6474v1 [astro-ph.CO]].

[8] M. Ackermann, et al. [Fermi-LAT Collaboration], Search for Dark Matter Satellites using the FERMI-LAT, *ApJ*, 747:121, 2012. [arXiv:1201.2691 [astro-ph.HE]].

[9] M. Ackermann et al., 2012, in preparation.

[10] D. S. Akerib et al., The Large Underground Xenon (LUX) Experiment, *Nuclear Inst. and Methods in Physics Research A* **704**:111 - 126, 2013. [arXiv:1211.3788v2 [physics.ins-det]].

[11] C. Alcock et al., The MACHO Project: Microlensing Results from 5.7 Years of LMC Observations, *ApJ*, **542** (2000) 281-307. [arXiv:astro-ph/0001272v1].

[12] U. Amaldi, W. de Boer, and H. Furstenau, Comparison of grand unified theories with electroweak and strong coupling constants measured at LEP. *Phys. Lett. B*, **260**:447, 1991.

[13] E. Aprile, XENON1T collaboration, The XENON1T Dark Matter Search Experiment, In *Proceedings of DM2012 at UCLA*. [arXiv:1206.6288v1 [astro-ph.IM]].

[14] E. Armengaud, et at. [EDELWEISS Collaboration], Final results of the EDELWEISS-II WIMP search using a 4-kg array of cryogenic germanium detectors with interleaved electrodes, *Phys. Lett. B*, **702**:329-335, 2011. [arXiv:1103.4070v3 [astro-ph.CO]].

[15] W. B. Atwood et al., The Large Area Telescope on the Fermi Gamma-Ray Space Telescope Mission. *ApJ*, **697**:10711102, June 2009.

[16] H. W. Babcock, The rotation of the Andromeda Nebula, *Lick Observatory Bulletin*; no. 498, 1939.

[17] E. A. Baltz et al., *JCAP* **07**:013, 2008.

[18] V. Barger et al., Dark matter and pulsar signals for Fermi LAT, PAMELA, ATIC, HESS and WMAP data, *Physics Letters B*, **678**:3, 20 July 2009, pp. 283292.

[19] K. G. Begeman, A. H. Broeils, and R. H. Sanders, Extended rotation curves of spiral galaxies: Dark haloes and modified dynamics, *Mon. Not. Roy. Astron. Soc.*, **249**:523, 1991.

[20] J. D. Bekenstein and R. H. Sanders, A primer to relativistic MOND theory. In G. A. Mamon, F. Combes, C. Deffayet, and B. Fort, eds., *Mass Profiles and Shapes of Cosmological Structures*, volume 20 of *EAS Publications Series*, 225-230, 2006.

[21] V. Belokurov et al., *ApJ*, **654**:897, 2007.

[22] L. Bergstrom, *Rep. Prog. Phys.* 63:793, 2000. [arXiv:hep-ph/0002126].

[23] L. Bergstrom, Radiative processes in dark matter photino annihilation, *Phys. Lett. B*, **225**:372, 1989.

[24] R. Bernabei et al., The DAMA/LIBRA apparatus, *Nucl.Instrum.Meth.A*, **592**:297-315, 2008. [arXiv:0804.2738v1 [astro-ph]].

[25] G. Bertone, D. Hooper and J. Silk, Particle Dark Matter: Evidence, Candidates and Constraints, *Phys. Rept.* **405**:279, 2005. [arXiv:hep-ph/0404175v2].

[26] G. R. Blumenthal, S. M. Faber, J. R. Primack, & M. J. Rees, Formation of galaxies and large-scale structure with cold dark matter, *Nature*, **311**:517, 1984.

[27] M. Boylan-Kolchin, J. Bullock, & M. Kaplinghat, Too big to fail? The puzzling darkness of massive Milky Way subhaloes,

*Mon.Not.Roy.Astron.Soc.* **415**:L40, 2011. [arXiv:1103.0007v2 [astro-ph.CO]].

[28] M. Boylan-Kolchin, Resolving Cosmic Structure Formation with the Millennium-II Simulation, *Mon.Not.Roy.Astron.Soc.* **398**:1150, 2009. [arXiv:0903.3041v2 [astro-ph.CO]].

[29] M. Bradač, S. W. Allen, T. Treu, et al. Revealing the properties of dark matter in the merging cluster MACS J0025.4-1222, *ApJ*, **687**:959-967, 2008. [arXiv:0806.2320].

[30] T. Bringmann, X. Huang, A. Ibarra, S. Vogl, C. Weniger, Fermi LAT Search for Internal Bremsstrahlung Signatures, *TUM-HEP* 828/12, *MPP*-2012-54. [arXiv:1203.1312v2 [hep-ph]].

[31] T. Bruch, for the CDMS Collaboration, CDMS-II to SuperCDMS: WIMP search at a zeptobarn, Prepared for *5th Patras Workshop on Axions, WIMPs and WISPs, Durham, England, 13-17 July 2009.* [arXiv:1001.3037v1 [astro-ph.IM]].

[32] A. Cesarini et al., The Galactic Center as a Dark Matter Gamma-Ray Source, *Astropart.Phys.* **21**:267-285, 2004. [arXiv:astro-ph/0305075v2].

[33] H. C. Cheng, J. L. Feng and K. T. Matchev, Kaluza-Klein Dark Matter, *Phys. Rev. Lett.* **89**:211301, 2002. [arXiv:hep-ph/0207125].

[34] H. Chernoff, *Ann. Math. Statist.*, **25**:573, 1954.

[35] D. J. H. Chung, P. Crotty, E. W. Kolb, A. Riotto, On the gravitational production of superheavy dark matter, *Phys.Rev.D* 64:**043503**, 2001. [arXiv:hep-ph/0104100v2].

[36] D. Clowe, M. Bradač, A. H. Gonzalez, et al., A Direct Empirical Proof of the Existence of Dark Matter, *ApJ*, **648**:L109, 2006a.

[37] J. Diemand et al., Clumps and streams in the local dark matter distribution, *Nature*, **454**:735-738, 2008. [arXiv:0805.1244v2 [astro-ph]].

[38] S. Dodelson, D. Hooper, and P. D. Serpico, Extracting the Gamma Ray Signal from Dark Matter Annihilation in the Galactic Center Region, *Phys.Rev.D*, **77**:063512, 2008. [arXiv:0711.4621v2 [astro-ph]].

[39] S. Dodelson, *Modern Cosmology* ch. 3. Elsevier, 2003.

[40] J. Einasto, Structure and Evolution of Regular Galaxies, PhD thesis, Tartu University, Tartu, 1972.

[41] S. M. Faber & R. E. Jackson, Velocity dispersions and mass-tolight ratios for elliptical galaxies, *ApJ*, **204**:668, 1976.

[42] J. Feng. Non-WIMP candidates, published in *Particle Dark Matter: Observations, Models, and Searches*, Cambridge University Press, 2010. [arXiv:1002.3828v1 [hep-ph]].

[43] I. Gogoladze, Bin He, and Qaisar Shafi, New fermions at the LHC and mass of the Higgs boson, *Phys. Lett. B*, Volume **690**5:495, 2010.

[44] P. Gondolo et al., DarkSUSY: Computing Supersymmetric Dark Matter Properties Numerically, *JCAP*, **0407**:008, 2004. [arXiv:astro-ph/0406204v1].

[45] P. Gondolo et al., DarkSUSY: A numerical package for supersymmetric dark matter calculations, In *proceedings of the 4th International Workshop on Identification of Dark Matter (idm2002), York, England, 2-6 September, 2002*. [arXiv:astro-ph/0211238].

[46] K. M. Gorski et al., HEALPix – a Framework for High Resolution Discretization, and Fast Analysis of Data Distributed on the Sphere, *ApJ*, **622**:759-771, 2005. [arXiv:astro-ph/0409513v1].

[47] M. Gustafsson et al., Significant Gamma Lines from Inert Higgs Dark Matter, *Phys.Rev.Lett.* **99**:041301, 2007. [arXiv:astro-ph/0703512v3].

[48] T. K. Hemmick et al., A search for anomalously heavy isotopes of low-Z nuclei, *Phys. Rev. D* **41**:2074, 1990.

[49] G. Hinshaw et al. Five-Year Wilkinson Microwave Anisotropy Probe (WMAP) observations: Data processing, sky maps, & basic results, *ApJS* **180**:225-245, 2009, [arXiv:0803.0732 [astro-ph]].

[50] T. E. Jeltema, S. Profumo, Fitting the Gamma-Ray Spectrum from Dark Matter with DMFIT: GLAST and the Galactic Center Region, *JCAP* **0811**:003, 2008. [arXiv:0808.2641v1 [astro-ph]].

[51] M. Kerr, Likelihood Methods for the Detection and Characterization of Gamma-ray Pulsars with the Fermi Large Area Telescope, Ph.D. thesis, University of Washington, Seattle, 2010. [arXiv:1101.6072v1 [astro-ph.IM]].

[52] I. King, *AJ*, **67**:471, 1962.

[53] A. Klypin, S. Trujillo-Gomez, J. Primack, Dark matter halos in the standard cosmological model: results from the Bolshoi simulation, *ApJ* **70**:102, 2010. [arXiv:1002.3660].

[54] H. Kraus et al., EURECA: The European future of dark matter searches with cryogenic detectors, *Nucl. Phys. Proc. Suppl.*, **173**:168-171, 2007.

[55] M. Kuhlen, J. Diemand, & P. Madau, The Dark Matter Annihilation Signal from Galactic Substructure: Predictions for GLAST, *ApJ*, **686**:262-278, 2008. [arXiv:0805.4416 [astro-ph]].

[56] J. Lande et al., Search for Spatially Extended Fermi-LAT Sources Using Two Years of Data. [arXiv:1207.0027v2 [astro-ph.HE]].

[57] M. Llena Garde et al., Constraining Dark Matter Signal from a Combined Analysis of Milky Way Satellites with the Fermi-LAT, in *2011 Fermi Symposium proceedings - eConf C110509.* [arXiv:1111.0320v1 [astro-ph.HE]].

[58] A. Macciò et al., The inner structure of haloes in Cold+Warm dark matter models, submitted to *MNRAS*, [arXiv:1202.2858v2 [astro-ph.CO]].

[59] L. Maiani, All you need to know about the Higgs boson, in *Proceedings: Gif-sur-Yvette Summer School on Particle Physics*, 1-52, 1979.

[60] M. Milgrom, A modification of the Newtonian dynamics as a possible alternative to the hidden mass hypothesis, *ApJ*, **270**:365-370, 1983.

[61] A. A. Moiseev et al., The anti-coincidence detector for the GLAST large area telescope. *Astroparticle Physics*, **27**:339358, June 2007.

[62] I. V. Moskalenko, GALPROP: modeling cosmic ray propagation and associated interstellar emissions. [arXiv:1105.4921v1 [astro-ph.HE]].

[63] J. R. Najita et al., From Stars to Super-planets: the Low-Mass IMF in the Young Cluster IC348, *ApJ*, **541**:977-1003, 2000. [arXiv:astro-ph/0005290].

[64] P. Natarajan and H. Zhao, MOND plus classical neutrinos are not enough for cluster lensing, *Mon. Not. Roy. Astron. Soc.*, **389**:250-256, 2008, [arXiv:0806.3080].

[65] J. F. Navarro, C. S. Frenk and S. D. M. White, The Structure of Cold Dark Matter Halos, *ApJ*, **462**:563-575, 1996. [arXiv:astro-ph/9508025v1].

[66] Jorge Nocedal and Stephen J. Wright. *Numerical Optimization.* Springer, August 2000.

[67] H. Pagels & J. R. Primack, Supersymmetry, cosmology, and new physics at teraelectronvolt energies, *Phys. Rev. Lett.*, 1982:223, 1982.

[68] P. L. Nolan, et al. [Fermi-LAT Collaboration], Fermi Large Area Telescope Second Source Catalog, *ApJS*, **199**:31, 2012. [arXiv:1108.1435v2 [astro-ph.HE]]

[69] R. D. Peccei. *Summary of the Beijing workshop on Weak Interactions and CP Violation*, August 22-26, 1989.

[70] R. D. Peccei and H. R. Quinn. Constraints imposed by CP conservation in the presence of instantons, *Phys. Rev. D*, **16**:1791-1797, 1977.

[71] P. J. E. Peebles, *Physical cosmology*, Princeton Series in Physics, Princeton, N.J., Princeton University Press, 1971

[72] S. Perlmutter et al., Measurements of Omega and Lambda from 42 High-Redshift Supernovae, *ApJ*, **517**:565-586, 1999. [arXiv:astro-ph/9812133v1].

[73] D. S. Reed, R. Bower, C. S. Frenk, et al., The first generation of star-forming haloes, *MNRAS*, **363**:393, 2005.

[74] A. Riess et al., Observational Evidence from Supernovae for an Accelerating Universe and a Cosmological Constant, *Astron.J.*, **116**:1009-1038, 1998. [arXiv:astro-ph/9805201v1].

[75] M. S. Roberts & R. N. Whitehurst, The rotation curve and geometry of M31 at large galactocentric distances., *ApJ*, **201**:327, 1975.

[76] E. Rozo, et al., Cosmological Constraints from the SDSS maxBCG Cluster Catalog, *ApJ*, **708**:645-660, 2010. [arXiv:0902.3702 [astro-ph.CO]].

[77] V. C. Rubin, W. K. J. Ford, & N. Thonnard, Rotational properties of 21 SC galaxies with a large range of luminosities and radii, from NGC 4605 R = 4kpc to UGC 2885 R = 122 kpc, *ApJ*, **238**:471, 1980.

[78] V. C. Rubin & W. K. J. Ford, Rotation of the Andromeda Nebula from a Spectroscopic Survey of Emission Regions, *ApJ*, **159**:379, 1970.

[79] M. Schmaltz and D. Tucker-Smith. Little Higgs review, *Ann. Rev. Nucl. Part. Sci.*, **55**:229-270, 2005, [arXiv:hep-ph/0502182].

[80] D. N. Schramm & M. S. Turner, Big-bang nucleosynthesis enters the precision era, *Reviews of Modern Physics*, 70:303, 1988.

[81] G. Servant and T. M. Tait, *Nucl. Phys. B*, **650**:391, 2003. [arXiv:hepph/0206071].

[82] C. Sgrò, The GLAST Large Area Telescope: calibration, performance and first light results. Doctoral thesis, Scuola Normale Superiore, Pisa, Italy, 2009.

[83] J. M. Siegal-Gaskins, The angular power spectrum of the diffuse gamma-ray background as a probe of Galactic dark matter substructure, to appear in *Proceedings of SnowPAC 2009*. [arXiv:0907.0183v1 [astro-ph.HE]].

[84] P. Sikivie. Axions, published in *Particle Dark Matter: Observations, Models, and Searches*, Cambridge University Press, 2010.

[85] T. Sjöstrand, S. Mrenna, and P. Skands, A Brief Introduction to PYTHIA 8.1, *Comput.Phys.Commun.*, **178**:852-867, 2008. [arXiv:0710.3820v1 [hep-ph]].

[86] C. Skordis, D. F. Mota, P. G. Ferreira, and C. Boehm. Large scale structure in Bekenstein's theory of relativistic modified Newtonian dynamics, *Phys. Rev. Lett.*, **96**:011301, 2006.

[87] S. Smith, The Mass of the Virgo Cluster, *ApJ*, **83**:23, 1936.

[88] D. Spergel et al., Wilkinson Microwave Anisotropy Probe (WMAP) Three Year Results: Implications for Cosmology, *Astrophys.J.Suppl.*, **170**:377, 2007. [arXiv:astro-ph/0603449v2].

[89] V. Springel, C. S. Frenk, & S. D. M. White, The large-scale structure of the Universe, *Nature*, **440**:1137. 2006.

[90] V. Springel et al., The Aquarius Project: the subhalos of galactic halos, *Mon.Not.Roy.Astron.Soc.*, **391**:1685-1711, 2008. [arXiv:0809.0898v1 [astro-ph]].

[91] L. Strigari et al., Redefining the Missing Satellites Problem, *ApJ*, **669**:676-683, 2007. [arXiv:0704.1817v2 [astro-ph]].

[92] L. Strigari et al., Precise constraints on the dark matter content of Milky Way dwarf galaxies for gamma-ray experiments, *Phys.Rev.D*, **75**:083526, 2007. [arXiv:astro-ph/0611925v2].

[93] A. M. Szelc, Dark Matter Experimental Overview, *Acta Phys.Polon.B*, **41**:1417-1440, 2010. [arXiv:1010.3918v1 [astro-ph.IM]].

[94] M. Taoso, G. Bertone, and A, Masiero, Dark Matter Candidates: A Ten-Point Test, *JCAP*, **0803**:002, 2008. [arXiv:0711.4996 [astro-ph]].

[95] B. M. Tinsley, Evolution of the Stars and Gas in Galaxies, *ApJ*, **151**:547, 1968.

[96] P. Tisserand et al., Limits on the Macho Content of the Galactic Halo from the EROS-2 Survey of the Magellanic Clouds, *Astron.Astrophys.*, **469**:387-404, 2007. [arXiv:astro-ph/0607207v2].

[97] E. J. Tollerud, J. S. Bullock, L. E. Strigari, & B. Willman, *ApJ*, **688**:277, 2008.

[98] S. Trujillo-Gomez, A. Klypin, J. Primack, A. J. Romanowsky, Galaxies in LCDM with Halo Abundance Matching: luminosity-velocity relation, baryonic mass-velocity relation, velocity function and clustering, *ApJ*, **742**:16, 2011. [arXiv:1005.1289v3 [astro-ph.CO]].

[99] C. Tyler, *Phys. Rev. D*, **99**:023509, 2002.

[100] M. G. Walker, M. Mateo, E. W. Olszewski, J. Penarrubia, N. Evans, et al., *ApJ*, **704**:1274, 2009.

[101] S. S. Wilks, The Large-Sample Distribution of the Likelihood Ratio for Testing Composite Hypotheses, *The Annals of Mathematical Statistics*, **9**: 6062, 1938.

[102] Y. B. Zeldovich, Gravitational instability: An approximate theory for large density perturbations, *A&A*, **5**:84, 1970.

[103] H. Zhao, D. J. Bacomn, A. N. Taylor, and K. Horne. Testing Bekenstein's relativistic modified Newtonian dynamics with lensing data, *Mon. Not. Roy. Astron. Soc.*, **368**:171-186, 2006.

[104] F. Zwicky, On the Masses of Nebulae and of Clusters of Nebulae, *ApJ*, **86**:217, 1937.

[105] F. Zwicky, Die Rotverschiebung von extragalaktischen Nebeln, *Helvetica Physica Acta*, **6**:110, 1933

[106] www.slac.stanford.edu/exp/glast/groups/canda/lat_Performance.htm

[107] fermi.gsfc.nasa.gov/ssc/data/analysis/LAT_caveats.html

[108] fermi.gsfc.nasa.gov/ssc/data/access/lat/BackgroundModels.html